

Dissertation  
submitted to the  
Combined Faculties for the Natural Sciences and for Mathematics  
of the Ruperto-Carola University of Heidelberg, Germany  
for the degree of  
Doctor of Natural Sciences

presented by  
Diplom-Physicist Joana Büchler Costa  
born in: Santo Tirso, Portugal  
Oral examination: February 9th 2005



# Development of a new Infrared Pyramid Wavefront Sensor

**Referees: Prof. Dr. Reinhard Mundt  
Prof. Dr. Josef Bille**



## **Zusammenfassung**

Eine Möglichkeit die erreichbare Himmelsabdeckung eines adaptiv-optischen Systems, dass die optischen Aberrationen in astronomischen Beobachtungen, die durch atmosphärische Turbulenz erzeugt werden, kompensiert, ist die Wellenfront im nahen infraroten Wellenlängenbereich abzutasten. Dort werden viele helle Sterne gefunden, die als Leitsterne benutzt werden können und die keine Entsprechung im Sichtbaren haben. Ein Pyramiden Wellenfront Sensor wurde gewählt wegen seiner Vorteile gegenüber eines Shack-Hartmann Sensors. Es wird ein Gewinn an Empfindlichkeit erwartet, der die Grenzhelligkeit erhöhen kann, wenn der Sensor in einem geschlossenen Regelkreis arbeitet. In dieser Arbeit wird die Möglichkeit ein solches Instrument zu bauen im Rahmen eines Projektes, PYRAMIR, untersucht, welches einen neuen Wellenfront Sensor am 3.5 m Teleskop auf dem Calar Alto implementieren wird. Ein analytisches Modell für die Erweiterung des linearen Bereiches des Sensors durch die atmosphärischen Turbulenzen, mit dem Preis einer Verminderung der Empfindlichkeit, sowie es auch bei der üblichen Modulation des Lichtkegels geschieht, wurde ausgearbeitet. Messungen am Teleskop, im Labor und Ergebnisse numerischer Simulationen zeigen die Möglichkeit einen Pyramiden Wellenfront Sensor ohne zusätzliche mechanische Modulation zu benutzen. Ein experimenteller Labor-Aufbau und numerische Simulationen eines kompletten adaptiv-optischen Systems waren die Hauptwerkzeuge für die Festlegung der Anforderungen an die Optik des neuen Instrumentes. Die Spezifikationen und Anforderungen an die Pyramiden wurden ausgearbeitet, die Effekte der Modulation und statischer Aberrationen auf die Messungen des Sensors, sowie der Einsatz räumlicher Filter wurden analysiert. Die Ergebnisse dieser Studie wurden direkt in PYRAMIR angewandt.

## **Abstract**

One possibility of increasing the achievable sky coverage of an adaptive optics system compensating the optical aberrations due to atmospheric turbulence for astronomical observations is sensing the wavefront at near-infrared wavelengths, where many bright stars are found, which can be used as guide stars and have no visible counterparts. A pyramid wavefront sensor was chosen due to its advantages over the Shack-Hartmann sensor. It is expected to achieve a gain in terms of sensitivity, raising the limiting magnitude, when used in closed-loop regime. In this work the possibility of building such an instrument has been studied in the framework of a project called PYRAMIR, which will implement a new wavefront sensor in the adaptive optics system at the Calar Alto 3.5 m telescope. An analytical model for the way in which atmospheric turbulence increases the linear range of this sensor at the cost of lower sensitivity, as usually is done through a mechanical modulation of the light beam, has been presented. Studies at the telescope, in the laboratory and through simulations show the possibility of using the pyramid wavefront sensor without any extra modulation. An experimental laboratory setup and numerical simulations of a full adaptive optics system were the main tools for establishing the optical requirements for the new instrument. Issues like the pyramid requirements and specifications, the effects of modulation and non-common path aberrations and spatial filters and their effects on the sensor have been analyzed in this way. The results were then directly applied in the design of PYRAMIR.



# Contents

<b>1</b>	<b>Introduction</b>	<b>1</b>
<b>2</b>	<b>Motivation</b>	<b>5</b>
2.1	The new instrument PYRAMIR . . . . .	5
2.2	Astronomical Motivation . . . . .	6
2.3	Technical Motivation . . . . .	9
<b>3</b>	<b>The pyramid wavefront sensor</b>	<b>11</b>
3.1	Geometrical description . . . . .	11
3.1.1	Error propagation . . . . .	14
3.2	Diffractive optical description . . . . .	14
3.3	Interpretation of the measurements . . . . .	17
3.3.1	Error propagation in frequency space . . . . .	19
3.4	Problems and open issues . . . . .	20
3.4.1	Light loss . . . . .	20
3.4.2	Calibration amplitude . . . . .	20
3.4.3	Modulation . . . . .	22
3.4.4	Static aberrations . . . . .	23
3.4.5	Pyramid roof . . . . .	23
3.4.6	Spatial filter . . . . .	24
3.4.7	Three-sided pyramid . . . . .	25
<b>4</b>	<b>The Modulation of the Atmosphere</b>	<b>29</b>
4.1	Introduction . . . . .	29
4.2	A model to describe the natural modulation . . . . .	30
4.3	A quantitative estimation of the atmospheric modulation effect . . . . .	32
4.4	Experimental Verification with real Stars . . . . .	36
4.5	Results . . . . .	38
<b>5</b>	<b>Laboratory setup and simulation technique</b>	<b>41</b>
5.1	Description of the laboratory system . . . . .	41
5.1.1	Optical setup and hardware . . . . .	41

5.1.2	Image Treatment and Software . . . . .	47
5.2	Description of the simulation . . . . .	50
5.2.1	Calibration . . . . .	50
5.2.2	Measurements . . . . .	51
5.2.3	Closed-loop operation . . . . .	51
<b>6</b>	<b>Laboratory experiments and simulations</b>	<b>53</b>
6.1	Pyramid characterization . . . . .	54
6.2	Light loss . . . . .	59
6.2.1	Numerical estimation . . . . .	59
6.2.2	Laboratory experiments . . . . .	60
6.3	Laboratory setup characterization . . . . .	61
6.3.1	The focus on the pyramid . . . . .	61
6.3.2	Offset subtraction . . . . .	63
6.3.3	Normalization diameter . . . . .	64
6.3.4	Quality of the modes . . . . .	64
6.3.5	Pupil sampling . . . . .	67
6.4	The modulation . . . . .	68
6.4.1	Simulation results . . . . .	68
6.4.2	Laboratory verification . . . . .	71
6.5	Effect of the pyramid roof . . . . .	75
6.6	Static aberrations . . . . .	76
6.7	Spatial filter . . . . .	78
6.8	Three-sided pyramid . . . . .	80
6.9	Future developments . . . . .	81
<b>7</b>	<b>The PYRAMIR instrument</b>	<b>83</b>
7.1	Optics . . . . .	83
7.2	Laboratory setup . . . . .	88
7.3	Mechanics . . . . .	88
7.4	Detector . . . . .	90
7.5	Thermic background estimation . . . . .	90
7.6	Limiting magnitude . . . . .	90
7.7	Electronics/Control . . . . .	92
7.8	Telescope implementation . . . . .	93
<b>8</b>	<b>Conclusions and Future Prospects</b>	<b>95</b>
	<b>Appendix</b>	<b>99</b>
	<b>A Integration of the power spectrum</b>	<b>99</b>
	<b>B Dependencies of the modulation function</b>	<b>101</b>

C Singular value decomposition	103
D Zernike polynomes	105
Bibliography	111



# Chapter 1

## Introduction

The study of astronomy has always been limited by the distortion due to the earth's turbulent atmosphere. Even through the transparent wavelength windows, where absorption is minimal, the flat wavefront coming from the astronomical sources is distorted by the changing atmosphere. There are many ways to circumvent this problem: the most obvious of them is to avoid the atmosphere completely by the installation of space-based telescopes. Above the atmosphere, these instruments deliver undistorted and beautiful images, limited only by the optics of the system and the finite aperture size. However the prohibitive costs of building, launching and maintaining these instruments is a major deterrent. Another way out is speckle interferometry, where short exposure images are taken, allowing for diffraction limited images. This method falls out of favor since it is limited by low sensitivity, and hence only bright targets can be used.

Adaptive optics has proven to be particularly useful in ground-based telescopes, successively measuring and correcting for the effects of the atmospheric turbulence. Geometrically this can be described as correcting the direction of the incoming light rays, which has been deflected while traversing our turbulent atmosphere. It is generally desired to have a real-time correction, which is able to follow the temporal evolution of the atmosphere, aiming to reach the diffraction limit and full optical performance of the instruments. The demand of high temporal frequency needed and the low photon flux coming from the weaker sources make adaptive optics projects very challenging and often interdisciplinary. An adaptive optics system generally has two main components: the wavefront sensor, which measures the wavefront distortion, and the wavefront corrector, which is usually a deformable mirror conjugated to the ground turbulence layer. In this work a new wavefront sensor is explored, which has its roots at the beginning of optical testing.

The Foucault knife-edge can be considered as the first direct predecessor of the pyramid wavefront sensor. Invented during the second half of the nineteenth century, described in Foucault (1859), this test uses a knife-edge at the focus of an objective lens or mirror to determine the direction of the light rays coming from each point of the objective. The small imperfections of the lens or mirror can thus be detected as variations in brightness. This method revolutionized the optical testing techniques of the period. Transposing this to a telescope pointed at a bright star, the knife-edge can be positioned at the focus, allowing for the detection of the continuously

evolving wavefront distortions due to the atmospheric turbulence. Later with the Hartmann test (Hartmann (1900)), the predecessor of the Shack-Hartmann wavefront sensor, together with the Foucault test, the basis for wavefront sensing for adaptive optics was established. However, the correction of wavefront distortions took some years to catch up (Babcock (1953)).

The principle of the Pyramid Wavefront Sensor, described in Ragazzoni (1996), is an adaptation of the Foucault knife-edge, with a four-sided glass prism, in the form of a pyramid, located at the focus of the telescope, which divides the light into four different beams, according to their direction when emanating from the entrance pupil. This sensor has many advantages over the established Shack-Hartmann sensor in terms of higher sensitivity and flexibility of sampling: this make it a very interesting alternative for astronomical light-starved applications.

Today adaptive optics systems have been implemented or planned on all major telescopes. The ALFA system was implemented on the 3.5 m telescope on the Calar Alto observatory in southern Spain. This system uses a Shack-Hartmann wavefront sensor working at visible wavelengths and a 97 piezo-actuator deformable mirror correcting the wavefront. The need for bright natural guide stars, suited to wavefront sensing, limits the sky coverage of the instrument. For some years ALFA worked with a laser guide star to overcome this problem. Ever since it has been decommissioned, various options have been explored for its successor. There was an urgent need to develop a wavefront sensor in the infrared to extend the sky coverage to sources bright in the infrared, which were too weak for guide stars in the visible. The high readout noise of the infrared detector arrays has always made this idea unfeasible. However the new generation of infrared detectors have overcome this defect, which makes the idea of an infrared wavefront sensor a realistic one. To date the only infrared system is NAOS, installed at one of the four VLT telescopes, working in the southern hemisphere.

The new wavefront sensor, called PYRAMIR, combines the new pyramid wavefront sensor with the infrared sensing capabilities to get full exploitation of the ALFA potentialities. The goal of this thesis has been to study the possibility of building such an instrument, for possible implementation in the existing ALFA system as a complement to the visible Shack-Hartmann sensor. A great part of this thesis has been devoted to the planning and development of this instrument. The telescope implementation has already started and first light is planned for beginning of 2005.

In Chapter 2 the astronomical and technical motivations for this work are presented. An introduction to the pyramid wavefront sensor and its measurement interpretation are elucidated in Chapter 3, where also some of the open issues that emerged during the project are discussed. In Chapter 4 a model for the effect of the atmospheric turbulence on the pyramid wavefront sensors' measurements is presented, which acts as a *modulation* increasing the linear range of the sensor and establishing a limit to its sensitivity. Telescope experiments comparing a system modulated only by the atmosphere and a conventional system modulated additionally by mechanical means are also presented. The main techniques for the study of the sensors performance and its characteristics have been a setup, which was built in laboratory, and numerical modelling of a pyramid wavefront sensor integrated in a telescope adaptive optics system. These are described in Chapter 5. A set of different glass pyramids has been characterized and related

issues like the light loss through the pyramid edges and the effect of a roof-shaped tip of the pyramid were analyzed, as well as the possibility to use a three-sided pyramid. Also the need and effect of modulation, the impact of static aberrations and the effect of a spatial filter in the focal plane have been studied. The results of these studies are given in Chapter 6. In Chapter 7 the complete instrument is described, where the setting of the requirements and the development of the optics were a major task during the elaboration of this thesis.



# Chapter 2

## Motivation

A major goal of this work, was the conceptual development and optical design of the new PYRAMIR instrument. This new wavefront sensor, based on the pyramid principle proposed by Ragazzoni (1996), will be installed parallel to the existing Shack-Hartmann wavefront sensor in ALFA, providing an alternate wavefront sensor for the existing adaptive optics (AO) system on the 3.5 m telescope at Calar Alto. This new wavefront sensor will operate at near-infrared wavelengths. In this chapter, we motivate the need of this project in terms of astronomical objectives, and as a technical demonstrator.

### 2.1 The new instrument PYRAMIR

In the past few years, pyramid wavefront sensors (PWS) have been studied and tested in laboratory simulations as well as real models on telescopes (Esposito et al. (2000a); Esposito and Riccardi (2001); Vérinaud (2004); Ragazzoni et al. (2000); Ghedina et al. (2003)). PWSs are also being implemented in other major AO projects for telescopes, like the Large Binocular Telescope (LBT) (Ragazzoni et al. (2003)) and the CHEOPS/Planet-finder for VLT (Feldt et al. (2003a,b,c); Claudi et al. (2004))<sup>1</sup>. The studies for this instrument have been made at MPIA in the framework of a preliminary proposal made to ESO responding to a call for a second generation VLT instrument called "Planet finder". CHEOPS draws a lot from the conceptual design and experience of PYRAMIR.

One of the greatest strengths this new type of wavefront sensor is its expected increase in sensitivity when operated in a closed loop, thus enhancing the limiting magnitude (Ragazzoni and Farinato (1999)). This is in stark comparison to a Shack-Hartmann wavefront sensor with the same configuration. Highest sensitivity is expected to be achieved with very little or no modulation<sup>2</sup>, and hence PYRAMIR was designed to work without modulation (although a back-up solution has been planned). The role and need of modulation (Esposito and Riccardi (2001); Costa et al. (2003b)) have been further discussed, and the modulation effect of the atmosphere

---

<sup>1</sup>CHEOPS: Characterization of Exo-planets by Opto-infrared Polarimetry and Spectroscopy

<sup>2</sup>Modulation is a movement of the focus around the pyramid tip, which is used to increase the dynamic range of the sensor, at the cost of lower sensitivity.

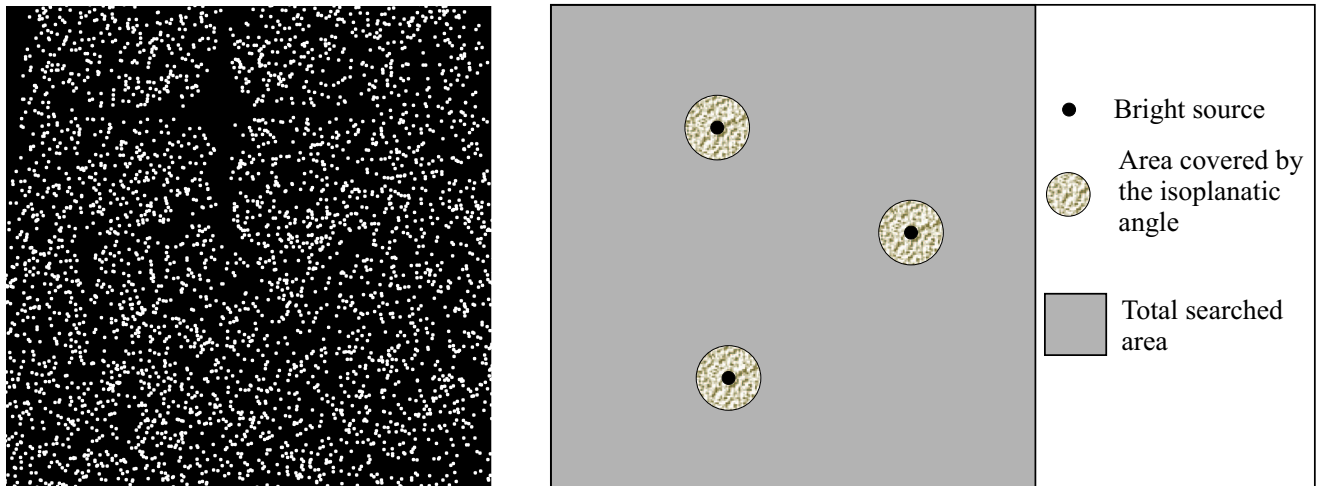


Figure 2.1: The left image is an extract of one area of the sky where suitable guide stars were found. The square area shown has  $0.75^\circ$  side length. The white fields represent the area covered by this stars. The right image schematically shows how the calculation of the sky coverage was done.

has been analyzed (see Chapter 4 and Costa (2004)).

There has always existed an urgent need to build a wavefront sensor operating at infrared wavelengths, since there exist many bright sources in the infrared  $1.25$ ,  $1.62$  and  $2.2 \mu\text{m}$  bands which do not possess visible counterparts. The main reason for the delay in its development has been the fact that the readout noise scales with the frame rate, being too high with current infrared detectors, at frame rates of the order of  $100 \text{ Hz}$ , which are necessary for AO. These cameras have been developed mainly for astronomical long-exposure images having a large number of pixels. The new infrared detectors that have been developed show a big improvement in this point. The first detector, which will be used for PYRAMIR is a 4-quadrant Hawaii-I detector from Rockwell, each quadrant having  $512 \times 512$  pixels read out in parallel through 4 independent output channels. These detector has been tested (Ligori et al. (2004)) and the frame rates of  $150 \text{ Hz}$  were achieved without significant increase of the readout noise, which stays below  $10 e^-$ . As a next step the AO-Mux, also from Rockwell, is planned to be implemented in PYRAMIR. It promises an even lower readout noise of  $5 e^-$ , but is unfortunately still under development.

## 2.2 Astronomical Motivation

One of the basic limitations of natural guide star AO systems is the achievable sky coverage. It is defined as the percentage of sky that can be observed while fulfilling the requirements of the AO system.

In the ALFA visible wavefront sensor, one always needs a star brighter than  $m_V \approx 12 \text{ mag}$  and closer than  $\approx 20''$  (in K-band) to the science target. This considerably limits the amount of

sky observable with AO. One of the possibilities to overcome this limitation is the use of artificial, laser guide stars (LGS). However, after ALFA's LGS facility was de-commissioned in 2000, a new technique to extend the possible choices of sciences targets was needed. One alternative is through multi-conjugated AO techniques, another one is an infrared wavefront sensor.

To make a direct comparison between the sky coverage of the visible wavefront sensor and the infrared sensor the same definition of limiting magnitude had to be used in both cases.

The new PWS is designed to work in a near-infrared wavelength range, from 1.0 to 2.35  $\mu\text{m}$ , and should be photon-noise limited down to  $m_K \approx 12$  mag. This is the estimated limiting magnitude for PYRAMIR (see Chapter 7) for the system reaching a Strehl ratio of 0.1 with high order correction (not only tip and tilt). The 2MASS Catalogue<sup>3</sup> was used to search for suitable guide stars. For this search random circular areas with  $1^{\circ 2}$  radius, visible in the northern hemisphere at Calar Alto latitude, ( $37.2^\circ$ ) were taken. This was done in the galactic plane ( $|glat| < 5^\circ$ ) as well as extragalactically ( $|glat| > 45^\circ$ ). According to the catalogue specifications, the number of stars found close to the galactic plane may be underestimated due to the high density of stars in that region.

A similar search was done in the Tycho2 catalogue for suitable guide stars for the visible wavefront sensor of ALFA. This sensor has already been in use for some years and it is known that with  $1''$  seeing, which are normal conditions at Calar Alto, it can still close the loop sensing with the  $5 \times 5$  array and correcting high orders with a guide star of 12th magnitude in the visible achieving Strehl ratios of the order of 0.1. The search was performed in the same random areas as for the infrared sources.

Since the turbulence is not concentrated in a thin layer at the telescope pupil but is distributed along the propagation path of the light through the atmosphere, the more distant the science target and the guide source are, the more the wavefront error de-correlates. This is called the angular anisoplanatism and constricts the science target to be within a certain angular distance from the guide source if it is not bright enough to be self-guided. The isoplanatic angle is defined as the angular distance at which the average wavefront error is  $1 \text{ rad}^2$ . Usually for the near-infrared the isoplanatic angle is given as  $10''$  (Hardy (1998)). Experience with ALFA has shown that it achieves the performance described in the last paragraph at an angle of  $20''$  from the guide star. In the following calculation this value will be taken as the "isoplanatic angle".

<sup>3</sup>Two Micron All-Sky Data Release, Point Source Catalogue

Sky Coverage	$m_V < 12$	$m_K < 12$
<b>Galactic</b>	0.8%	27%
<b>Extragalactic</b>	0.2%	0.9%

Table 2.1: Achievable sky coverage for an infrared pyramid wavefront sensor as PYRAMIR, having a limiting magnitude of 12 in K-band and for a visible wavefront sensor working with  $m_V < 12$ . For the calculation details refer to the text.

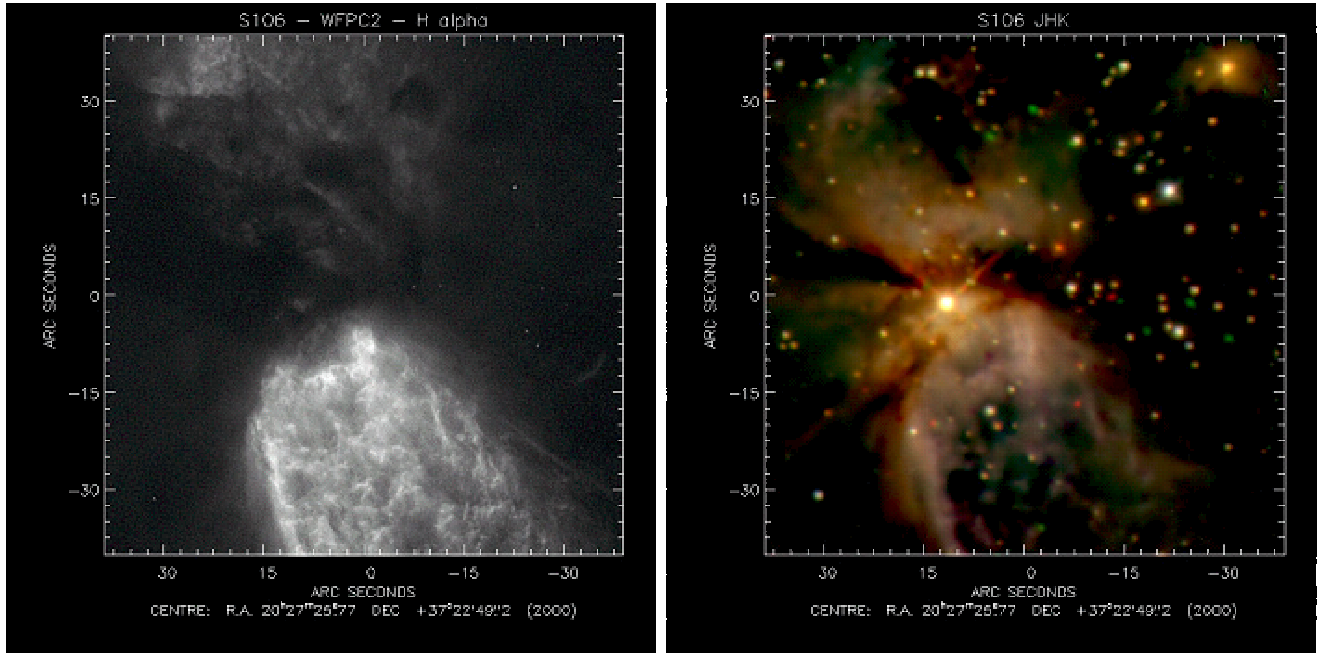


Figure 2.2: These are pictures of the Massive Star Forming Region S106 taken with the Hubble Space Telescope (from Bally et al. (1998)). The image on the left has been taken at optical wavelength and the one on the right was observed at the near-infrared. In the latter a central source can be seen, which is surrounded by ionized material and is embedded in a molecular cloud. This makes the visual extinction so high that it can not be observed. In the near-infrared the star is very bright and can be used as guide star for reference.

Each source, which was found, increases the sky coverage by about  $\pi\theta_0^2$ , where  $\theta_0$  is the isoplanatic angle (see Fig. 2.1). The total covered area divided by the total search area of  $\pi^{\circ 2}$  gives the percentage of sky covered by the sensor in the search area.

The sky coverage in the galactic plane gives a mean value of 27% for stars brighter than 12th magnitude in K-band. This is a considerable increase relative to the visible sensors' coverage, which is less than 1%. For the extragalactic region coverage of visible and infrared is 0.2% and 0.9% respectively (see Tab. 2.1).

On the other hand one of the prime science drivers for the PYRAMIR project has been the increased sample coverage of regions of special interest. It increases the observable targets by a large number of objects which can not be reached by any other adaptive optics system in the northern hemisphere. In galactic star forming regions, observations generally suffer a high extinction originating from large amounts of molecular material enshrouding the newly born stars and effectively the complete star forming regions. This results in a high reddening of stars inside these regions, i.e. most of the objects are invisible at visual wavelengths but bright in the infrared. Often the interesting object can even be used as self-reference or as reference source

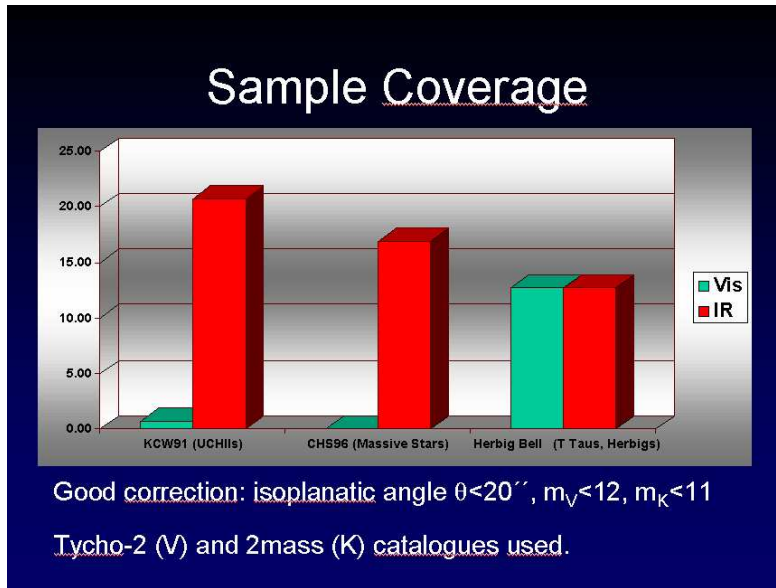


Figure 2.3: Sample coverage for ALFA’s visual wavefront sensor and PYRAMIR.

for the also embedded surroundings, within the isoplanatic angle. We find this situation always in Young Stellar Objects with very hot massive stars, but also in stars with debris disks, stars undergoing mass loss, Novae or Peculiar Objects.

The result of a comparison of the coverage of this kind of objects by the visible and the new infrared wavefront sensor can be seen in Fig. 2.3. Here we compare a sample of ultra-compact HII regions from Kurtz et al. (1990), a sample of young, massive stars from Chan et al. (1996), and a sample of T Tau and Herbig Ae/Be stars for the two wavefront sensors. It can clearly be seen that for the massive stars, which generally develop faster than low-mass stars and are thus more deeply embedded in dust for a considerable fraction of their lifetime, an infrared sensor increases the chances to observe such objects from practically zero up to a respectable 20%. This comparative estimation of the sky and sample coverage of the existing visible wavefront sensor with the new PWS has been analyzed in Costa et al. (2003a).

## 2.3 Technical Motivation

The refractive-index changes produced by turbulence are almost wavelength-independent over the range between 0.36 and 10  $\mu\text{m}$ . Therefore, given an optical path-length error due to turbulence, it will produce smaller phase shifts at longer wavelengths. This translates into the fact that turbulence is relatively benign at near-infrared wavelengths, having values of  $r_0$  in the range of 0.5 to 1.0 m while in the visual  $r_0$  is approximately 0.1 m. This means that the degradation effects on uncompensated images in the near-infrared are smaller than in the visible, which results in a smaller angular image diameter at longer wavelengths. A wavefront sensor working in the near-infrared will better adapt to the spatial and temporal characteristics of the ALFA system. The spatial sampling of the wavefront, given by the deformable mirror subaperture size,

is 0.35 m and the temporal characteristics of the adaptive optics loop, given by the loop frequency, is 100-200 Hz. This is hardly effective to compensate the turbulence in the visible, while in the infrared the demands are lower. Together with the greater  $r_0$  also the proportionality of the Greenwood frequency  $f_G \propto \lambda^{-6/5}$  allows a longer integration time at longer wavelengths. Of course visible wavefront sensing allows a potentially greater improvement but in the near infrared the Strehl ratios will be higher and the AO-loop is closed more easily, meaning a better bootstrapping and a higher limiting magnitude.

On the other hand the PWS is expected to achieve higher sensitivity than the Shack-Hartmann sensor in a closed loop, enhancing the limiting magnitude. A pyramid sensor benefits from the closed-loop operation to its intrinsic limitation only by the diffraction by the full telescope aperture (whereas a Shack-Hartmann sensor is always limited by the lenslet sub-apertures diffraction effects). This allows the PWS to have a gain up to 2 in limiting magnitude with respect to a Shack-Hartmann with the same configuration (Ragazzoni and Farinato (1999)).

The combination of these parameters leads to the conclusion that a PWS is better adapted to near-infrared sensing in ALFA than a Shack-Hartmann sensor would be. In the case of systems with deformable mirrors with more actuators and a higher loop frequency, like the AO system for the CHEOPS/Planet Finder instrument, the PWS will be able to use its full potential also at visible wavelengths.

# Chapter 3

## The pyramid wavefront sensor

This chapter begins with an introduction to the pyramid wavefront sensor and some results, which contribute to the better understanding of the measurements given by this still quite new technique.

The PWS was proposed by Ragazzoni (1996) as a pupil plane wavefront sensor being an alternative to the most commonly used sensors for astronomical purposes, like the Shack-Hartmann, Curvature or Shearing interferometers. This new concept presents some special characteristics, like the easily and continuously adaptable dynamic range and the variable sampling in the pupil plane. But one of the main advantages is the improved sensitivity, compared to the Shack-Hartmann, when used in closed loop diffraction limited in the sensing wavelength (Ragazzoni and Farinato (1999)).

Here we present the more intuitive geometric description of this sensor as well as a diffractive analysis, which allows to get more accurate expressions for the measurement signals given by the PWS.

There are still many open issues related to the measurements of this type of sensor and its limitations. In the last sections some issues, which are directly related to this kind of sensor and which were treated in this thesis, are explained.

### 3.1 Geometrical description

In geometric optics the incoming wavefront is focussed on top of a four-sided prism, which divides the light in four separate beams (see Fig. 3.1). Through a relay lens the entrance pupil is re-imaged on a detector, where four pupil images are formed. If the wavefront is not aberrated the light is equally split by the pyramid and this four pupils are equally and uniformly illuminated. In the case of an aberrated wavefront the focussed beam can be described by a bundle of rays, which do not all hit the pyramid tip. Rays emanating from regions of the pupil where the wavefront presents a local slope, will hit only one side of the pyramid according to the sign of this local slope. According to this only one of the four conjugated pupil-locations on the detector will be illuminated, while the other three remain dark. This means that, as soon as the first

derivative of the wavefront is not strictly zero, the PWS signal saturates, giving only the sign of the local wavefront, like in the analogous Foucault knife-edge test (Foucault (1859)).

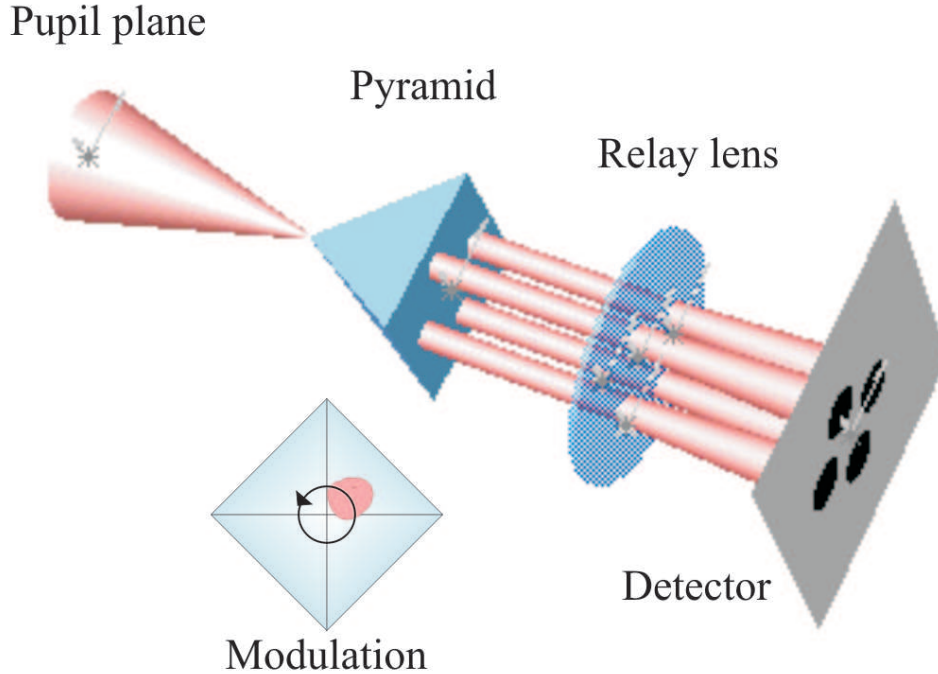


Figure 3.1: A geometrical description of the pyramid wavefront sensor.

The distance from the tip, where the ray hits the pyramid, is determined by the size of the slope. Defining a coordinate system  $(x_i, y_i)$ , having its origin in the entrance pupil center and being normalized on the pupil edges, and a coordinate system  $(x_f, y_f)$  centered on the pyramid edge in the focal plane, aligned with the first one, one can write:

$$x_f = f \frac{\partial W(x_p, y_p)}{\partial x_p} \quad y_f = f \frac{\partial W(x_p, y_p)}{\partial y_p}, \quad (3.1)$$

where  $W(x_p, y_p)$  is the wavefront in the pupil plane to be measured and  $f$  is the effective system focal length. But this information is not accessible in this more simple configuration. To overcome this limitation temporal modulations of the pupil local tilt can be introduced. More intuitively the beam is moved over the four sides of the pyramid at least once during a single integration of the detector. This movement can be introduced in different ways:

- Mechanically through a tip-tilt mirror in the pupil plane (Riccardi et al. (1998)).
- By moving the pyramid itself (Ragazzoni (1996)).
- Through a defocus term with sinusoidally varying amplitude, introduced by a vibrating membrane.

- Statically a similar effect can be achieved by a light diffusing plate introduced in an intermediate pupil plane (Ragazzoni et al. (2002)).

In the first cases the modulation can be seen as the superposition of a tilt made in an incoherent way, by temporal averaging, making the spot size larger than its original size. The second technique uses a coherent modulation by introducing some high order spatial frequencies. These have to be selected in a way to enlarge the spot size but, simultaneously, to avoid the introduction of perturbations on the modes that one wants to measure. In other words: the content of low spatial frequency should be closely enough to zero so as not to perturb the measurement.

Assuming the most simple case of a circular beam movement around the pyramids' tip, the more aberrated rays, which hit the pyramid more distant from the tip in the static case, will spend more time (or equivalently perform a longer path) on one of the pyramid sides during one integration cycle. According to the length of the path the ray follows on each side, the intensity in the correspondent conjugated pixel on the detector will be different. If the amplitude of this modulation movement is at least as big as the biggest local tilt in the wavefront, there will be no saturation and a quantitative estimation can be done. Calculating the path lengths in dependence of the modulation amplitude, the relation between local wavefront derivative and intensity ratios is (Riccardi et al. (1998)):

$$\frac{\partial W(x_p, y_p)}{\partial x_p} = a_0 \sin\left(\frac{\pi}{2} S_x\right) \quad \frac{\partial W(x_p, y_p)}{\partial y_p} = a_0 \sin\left(\frac{\pi}{2} S_y\right), \quad (3.2)$$

where the quantities  $S$ , which we will call *signals*, are defined as:

$$S_x(x_i, y_i) \equiv \frac{(I_1(x_i, y_i) + I_4(x_i, y_i)) - (I_2(x_i, y_i) + I_3(x_i, y_i))}{\sum_{i=1}^4 I_i(x_i, y_i)}$$

$$S_y(x_i, y_i) \equiv \frac{(I_1(x_i, y_i) + I_2(x_i, y_i)) - (I_3(x_i, y_i) + I_4(x_i, y_i))}{\sum_{i=1}^4 I_i(x_i, y_i)}, \quad (3.3)$$

where  $I_i$  are the intensities in the four conjugated positions  $(x_i, y_i)$  in the image plane and  $a_0$  is the angular modulation amplitude. The amplitude of the displacement of the beam in the focal plane is  $a_0 f$ . For small signals  $\sin S_x \approx S_x$  and it can be written:

$$\frac{\partial W(x_p, y_p)}{\partial x_p} = a_0 \frac{\pi}{2} S_x \quad \frac{\partial W(x_p, y_p)}{\partial y_p} = a_0 \frac{\pi}{2} S_y. \quad (3.4)$$

This approximation is valid for slopes smaller than 1 modulation amplitude  $a_0$  or even less and that modulation increases the range in which there is a linear relation between the wavefront slope and the sensor signal.

Modulation also has an effect on the sensitivity of the sensor, which we will define as the ratio between the measured signal and the incoming wavefront slope. This ratio is inversely proportional to the modulation amplitude. The sensitivity of the PWS will decrease with the modulation amplitude.

### 3.1.1 Error propagation

Using the expression for the signal of the sensor in Eq. 3.3 the propagation of noise due to measurement noise can be estimated.

Using the fact that  $S_{x,y}$  are functions of  $I_1$ ,  $I_2$ ,  $I_3$  and  $I_4$  the error on the signals can be written as:

$$\sigma_{S_{x,y}}^2 = \sigma_{I_1}^2 \left( \frac{\partial S_{x,y}}{\partial I_1} \right)^2 + \sigma_{I_2}^2 \left( \frac{\partial S_{x,y}}{\partial I_2} \right)^2 + \sigma_{I_3}^2 \left( \frac{\partial S_{x,y}}{\partial I_3} \right)^2 + \sigma_{I_4}^2 \left( \frac{\partial S_{x,y}}{\partial I_4} \right)^2. \quad (3.5)$$

Due to the statistical nature of photons, they can be assumed as arriving according to a poisson distribution. For the variance associated to  $I_i$  (for  $i = 1, 2, 3$  or  $4$ ) the assumption is made that the aberration is already small, so that the intensities in the four pupils are all approximately  $N/4$ , where  $N$  is the total number of photons arriving at the detector. It follows that  $\sigma_{I_i}^2 \approx \frac{N}{4}$  and therefore the signal error due to photon noise can be calculated as (Feeney (2001)):

$$\sigma_{S_{x,y}}^2 = \frac{1}{N}. \quad (3.6)$$

The reconstruction error due to photon noise in the case of a modal reconstruction reduces then to (Feeney (2001)):

$$\sigma_{\text{rec}}^2 = \frac{1}{N n_s} \sum_{i=1}^{M_{\text{max}}} \frac{1}{\sigma_i^2}, \quad (3.7)$$

where  $n_s$  is the number of pupil sampling points and  $\sigma_i^2$  is the variance of the  $i$ -th mode in signal space.  $M_{\text{max}}$  is the number of modes used in the reconstruction.

Similarly the error on the signal due to readout noise  $\sigma_{\text{RN}}^2$  can be estimated:

$$\sigma_{S_{x,y}}^2 = \frac{4\sigma_{\text{RN}}^2}{N^2}. \quad (3.8)$$

With this the total error on the slope estimation due to photon noise and detector readout noise is

$$\sigma_{\frac{\partial W}{\partial x,y}}^2 = (\pi r)^2 \left( \frac{1}{4N} + \frac{\sigma_{\text{RN}}^2}{N^2} \right). \quad (3.9)$$

## 3.2 Diffractive optical description

Some simulated images of the four pupils on the detector are shown in Fig. 3.2 for a flat wavefront and some zernike modes. It can be seen that the intensity distribution in the four pupils can not be described simply by geometrical optics.

As a simplified analysis of the diffraction effects on the PWS the Foucault knife-edge is recalled. We start with the expression for the signal in the pupil of the knife-edge wavefront sensor, where the knife-edge is located along the  $y$ -axis direction, and we only measure signals in the  $x$ -axis

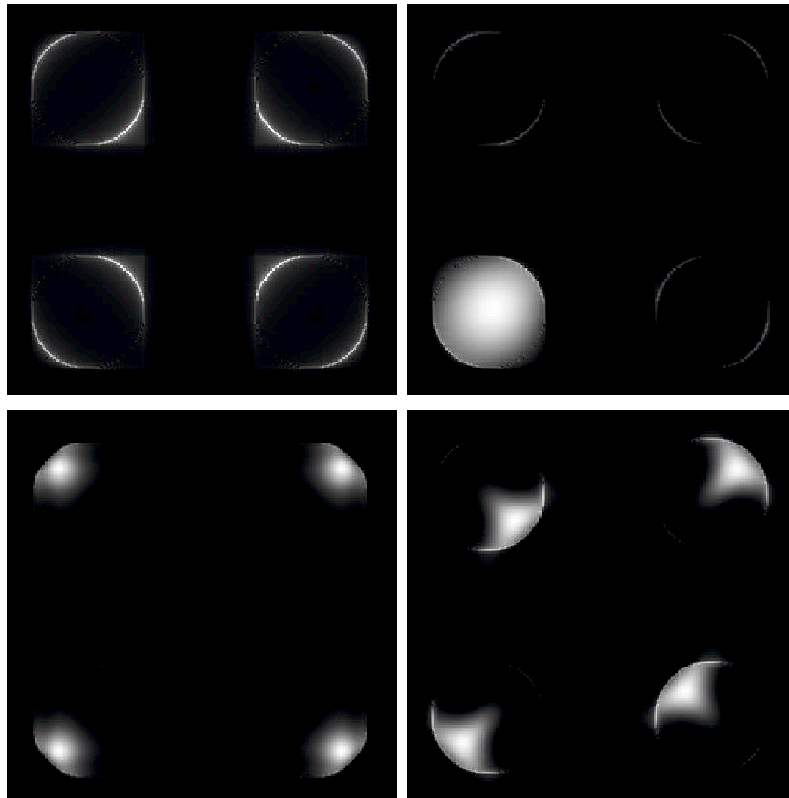


Figure 3.2: This figure shows simulated CCD images, which are obtained with a PWS, for different incoming aberrated wavefronts. Starting at the top left, a flat wavefront, a tilt, a defocus and an astigmatismus are represented. No modulation is used.

direction ( $S_x$ ).

Starting from the expression of Linfoot (1948) and taking into account an image inversion (Wilson (1975)), the complex amplitude of the electromagnetic field in the image plane after diffraction at a knife-edge along the  $y$ -axis can be written as (Feeney (2001)):

$$u_i^{\mp}(x, y) = \frac{1}{2}u_0(x, y) \pm \frac{i}{2\pi} \int_{-B(y)}^{B(y)} dx' p.v. \frac{u_0(x', y)}{(x' - x)}, \quad (3.10)$$

where  $p.v.$  means the principal value distribution. Here  $u_0(x', y)$  is the complex electromagnetic field amplitude in the object plane and  $\pm B(y)$  are the edge points of a chord perpendicular to the knife edge at the coordinate  $y$ . The  $\pm$  are the two complementary positions having the negative or the positive side covered. Since the observable is the absolute square of the complex

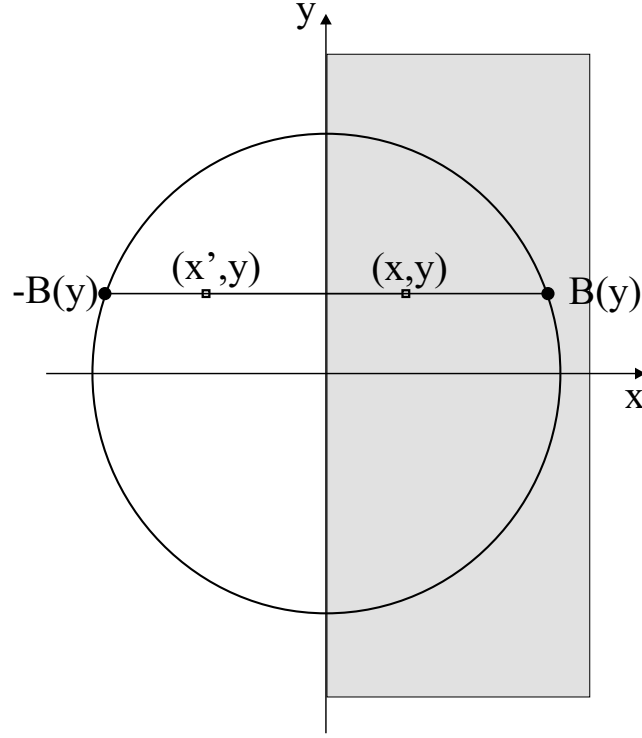


Figure 3.3: The signal computation for the knife-edge wavefront sensor.

amplitude, it can be calculated with:

$$|u_i^+(x, y)|^2 = \left[ \frac{1}{2}u_0(x, y) - \frac{i}{2\pi} \int_{-B(y)}^{B(y)} dx' p.v. \frac{u_0(x', y)}{(x' - x)} \right] \cdot \left[ \frac{1}{2}u_0^*(x, y) + \frac{i}{2\pi} \int_{-B(y)}^{B(y)} dx' p.v. \frac{u_0^*(x', y)}{(x' - x)} \right], \quad (3.11)$$

and similarly for  $|u_i^-(x, y)|^2$ . The signals in x-direction can be calculated as:

$$S_x(x, y) = \frac{|u_i^-|^2 - |u_i^+|^2}{|u_0|^2}. \quad (3.12)$$

Substituting the previous expressions for  $|u_i^\pm|^2$  and  $u_0(x, y) = E \exp[-i\phi(x, y)]$  one gets:

$$S_x = \frac{2i}{4\pi} \left[ u_0^* \int_{-B(y)}^{B(y)} dx' p.v. \frac{u_0(x', y)}{(x' - x)} - u_0 \int_{-B(y)}^{B(y)} dx' p.v. \frac{u_0^*(x', y)}{(x' - x)} \right], \quad (3.13)$$

and after some simplifications:

$$S_x(x, y) = \frac{1}{\pi} \int_{-B(y)}^{B(y)} dx' p.v. \frac{\sin[\phi(x', y) - \phi(x, y)]}{(x' - x)}. \quad (3.14)$$

The integral is performed along a chord in the pupil, perpendicular to the knife-edge, which contains the point  $(x, y)$ , where the signal is being computed. As represented in Fig. 3.3,  $\pm B(y)$  are the edge points of the chord and  $\phi(x, y)$  is the wavefront phase at point  $(x, y)$ . In the integral the contribution of the sine-term is weighted with the distance between the integration point  $(x', y)$  and the point where the signal is being measured  $(x, y)$ .

In the simplified knife-edge case the modulation can be reduced to a linear movement of the beam perpendicular to the edge, where the phase is increased by an oscillating tilt term with amplitude  $a_0$  and period in time  $\Delta t$ :

$$\tilde{\phi}(x, y; t) = \phi(x, y) + a_0 \frac{2t}{\Delta t} x \quad (3.15)$$

for a time  $t$ . Substitution in Eq. (3.14) and integration over one period yields:

$$S_x(x, y) = \frac{1}{\pi} \int_{-B(y)}^{B(y)} dx' p.v. \frac{\sin[\phi(x', y) - \phi(x, y)]}{(x' - x)} \times \underbrace{\Delta t \frac{\sin[a_0(x' - x)]}{a_0(x' - x)}}_{\text{modulation}}. \quad (3.16)$$

The signal has been averaged over one modulation period  $\Delta t$  and  $a_0$  is the modulation amplitude. Since  $\sin x/x \rightarrow 1$ , for small  $x$ , the term added to the integral acts as a delta function reducing the contribution of the more distant pupil points to the signal at  $(x, y)$  and therefore linearizing the signal, so that, for a sufficiently large modulation amplitude, the signal measured will correspond to the local derivative of the wavefront.

### 3.3 Interpretation of the measurements

The diffractive expression for the PWS signals can be used as starting point for a deeper analysis of the sensors measurements. The slope/phase sensor duality of the modulated PWS is one of those, which gives an insight into the interpretation of measurements given by the PWS. As deduced in the paper of V erinaud (2004) the sensitivity of the PWS in the frequency domain shows characteristics of a slope sensor and of a phase sensor depending on the frequency range. The sensitivity in the frequency domain  $\Xi(u)$  can be defined as the standard deviation of measurements for an aberration of frequency  $u$  with the phase variance of  $1 \text{ rad}^2$ . The result given in the paper, stated here without proof is:

$$\Xi(u) = \begin{cases} -i \text{sgn}(u) & , |u| > \frac{\alpha}{\lambda} \\ -\frac{i\lambda}{\alpha} u & , |u| < \frac{\alpha}{\lambda} \end{cases}$$

Here  $\lambda$  is the wavelength and  $\alpha$  is the angular modulation radius. This expression shows that for frequencies lower than  $\frac{\alpha}{\lambda}$  the sensors sensitivity increases linearly with the frequency, as generally

in the case of a slope sensor. This is also the case for a Shack-Hartmann sensor. Above that frequency, the sensitivity stays constant, what is characteristic for a phase sensor.

For frequencies lower than the Nyquist limit, the signal to noise ratio in the frequency domain will be higher for the PWS than for the Shack-Hartmann. This translates into an increase up to 2 in the limiting magnitude for a 100 m telescope.

Clearly there is also an advantage of the PWS in terms of aliasing noise. This noise is caused by higher spatial frequencies which are not sensed by the sensor due to its limited sampling and that are interpreted as lower frequencies, disturbing the measurement. The sensors sensitivity to these higher frequencies is lower as in the case of a pure slope sensor.

The frequency where the behavior slope/phase sensor changes increases with the modulation amplitude. This points to the conclusion that the modulation amplitude should be kept as low as possible.

For the case of no modulation the equations can be simplified. In the case of small aberrations, like is expected in closed loop, the wavefront phase  $\phi(x, y) \ll 1$ , which allows do simplify:  $\sin(\phi) \approx \phi$  and the signal expression for the non-modulated sensor can be written as:

$$S_x(x, y) = \frac{1}{\pi} \int_{-B(y)}^{B(y)} dx' p.v. \frac{\phi(x', y) - \phi(x, y)}{(x' - x)}. \quad (3.17)$$

The integrand will only be equal to the derivative of the wavefront phase  $\phi$  in the limit  $x \rightarrow x'$  or if  $\phi$  varies very little over the telescope diameter. Only in this case the integral will be proportional to the derivative. This explains the fact that the PWS can not be strictly considered a slope sensor.

This integral can be separated:

$$S_x(x, y) = \frac{1}{\pi} \left[ \int_{-B(y)}^{B(y)} dx' p.v. \frac{\phi(x', y)}{(x' - x)} - \phi(x, y) \int_{-B(y)}^{B(y)} dx' p.v. \frac{1}{(x' - x)} \right]. \quad (3.18)$$

The second integral can be calculated

$$\begin{aligned} \int_{-B(y)}^{B(y)} dx' p.v. \frac{1}{(x' - x)} &= \ln(B - x) - \ln(B + x) \\ &= -\frac{2x}{B} + \mathcal{O}\left(\left(\frac{x}{B}\right)^3\right), \end{aligned} \quad (3.19)$$

and introducing this in Eq. (3.18) the expression for the signal can be written:

$$S_x(x, y) = \frac{1}{\pi} \left\{ \int_{-B(y)}^{B(y)} dx' p.v. \frac{\phi(x', y)}{(x' - x)} - \phi(x, y) \left[ \frac{2x}{B} - \mathcal{O}\left(\left(\frac{x}{B}\right)^3\right) \right] \right\}. \quad (3.20)$$

For the case of an infinite telescope size  $B \rightarrow +\infty$  the integral in Eq. 3.19 tends to 0 and the signal  $S_x(x, y)$  can be written as a simple convolution:

$$S_x(x, y) = \frac{1}{\pi} \phi(x, y) \otimes \underbrace{\left[ p.v. \frac{\delta(y)}{x} \right]}_{\xi(x, y)}, \quad (3.21)$$

defining  $\xi$  as the sensitivity function in direct space. Performing a fourier transform the sensitivity function in the frequency space is obtained:

$$\text{FT}(\xi(x, y)) = \Xi(u, v) = i\pi \text{sgn}(u). \quad (3.22)$$

This shows that the fourier transform of Eq. (3.21), giving the frequency spectrum of the signals, is:

$$\begin{aligned} \tilde{S}_x(u, v) &= \frac{1}{\pi} \Xi(u, v) \tilde{\phi}(u, v) \\ &= i \text{sgn}(u) \tilde{\phi}(u, v). \end{aligned} \quad (3.23)$$

The frequency spectrum of the signals is proportional to the frequency spectrum of the wavefront aberration.

### 3.3.1 Error propagation in frequency space

For the one-dimensional model the reconstruction process can be written as:

$$\tilde{\phi}(u, v) = \mathbb{R} \tilde{S}_x(u, v), \quad (3.24)$$

with  $\mathbb{R} = 1/(i \text{sgn}(u))$  being the reconstructor. The propagation error through the reconstruction process can then be calculated from the measurement error  $\sigma_n$ :

$$\begin{aligned} \sigma_\phi^2(u) &= |\mathbb{R}|^2 \sigma_n^2 \\ &= \sigma_n^2, \end{aligned} \quad (3.25)$$

being undefined for  $u = 0$ , where  $\mathbb{R} \rightarrow +\infty$ . For this model it can be seen that the error propagation is constant and equal to unity through all frequencies. This means that the reconstruction process is not increasing the error, which is introduced into the system by the measurement, like photon noise, for example. Note that this model does not take into account any sub-aperture filtering effect (which has been done by (Vérinaud (2004))), which provokes an increase in the error propagation for higher frequencies.

### 3.4 Problems and open issues

The PWS still is a quite new concept, which presents open questions in terms of interpretation of the measurements and technical limitations. In this section an overview on this questions and problems will be given, while later in this work detailed measurements and solutions are showed.

#### 3.4.1 Light loss

One important issue, since adaptive optics and astronomy in general are photon-starving sciences, is the light loss due to the pyramid edges in the wavefront sensor. In case the beam is modulated around the pyramid tip, the size of the latter will be less important, especially with big modulation amplitudes. In this case, the size of the edges should be taken into account, but since the beam is not stable on top of one edge, the damage decreases with the modulation amplitude. For a not-modulated system, that keeps the focus fixed on the pyramid tip, the loss of light through the tip and edges will be considerably greater (see Fig. 3.4). Through simulated images of the pupils on the detector, the effect of non-negligible edges scattering light between the pupils can be seen in Fig. 3.5.

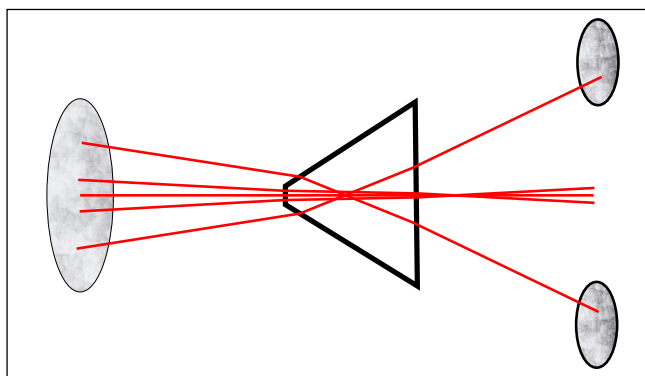


Figure 3.4: Through the edges and the tip of the pyramid the light will be diffracted landing outside of the four pupils. Since at the edges the angle of refraction varies (they are normally less tilted than the 4 surfaces), the stray light will mostly land between the 4-pupil image.

#### 3.4.2 Calibration amplitude

Before performing measurements with the wavefront sensor a calibration has to be performed. This means, in practice, that a set of independent wavefront modes is introduced in the sensor and the corresponding signals are recorded. After this the measured wavefront can be decomposed into the set of modes used in the calibration with a least-squares method. This implies that the recorded signals have a linear relation with the incoming aberration. As happens with every wavefront sensor also in the PWS there is a range where the systems response is linear (see Section 3.1). Beyond this limit, the response is non-linear and the signal saturates, making it impossible to make exact measurements. If the sensor is not modulated, the linear range can

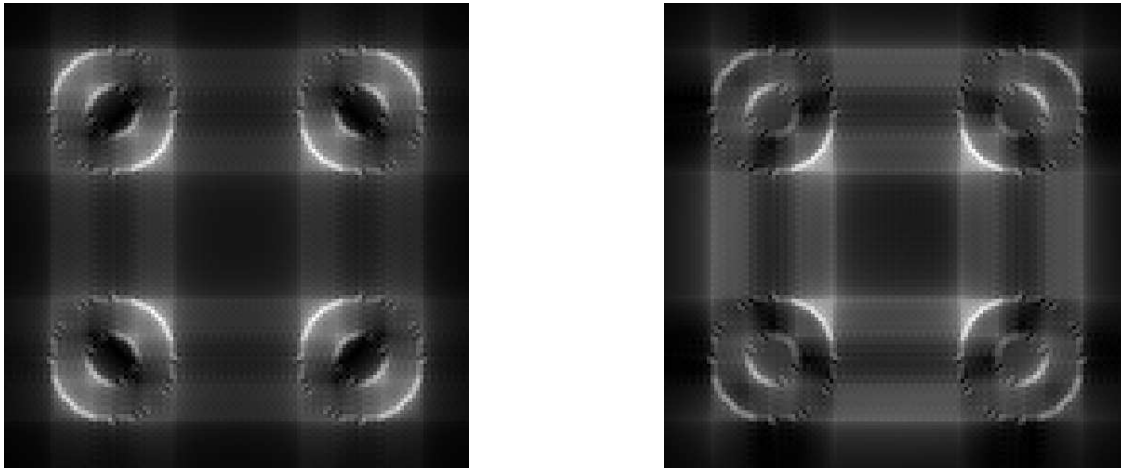


Figure 3.5: The simulated CCD images shown here correspond to a pyramid with an edge lower than  $10\ \mu\text{m}$  on the left and an edge size of  $100\ \mu\text{m}$  on the right. The simulation was done for a system with spot FWHM of  $220\ \mu\text{m}$ . The square root of the intensity is shown, to make the differences more visible.

not be adapted to the conditions.

To choose the best calibration amplitude for the wavefront sensor a trade-off between two situations has to be achieved. One characteristic of the sensor, when it is used in non-modulated regime, is the reduced dynamic range and its non-linear behavior when saturated. This is illustrated in Fig.3.6. The system should be calibrated within its linear range, which is in any case smaller than  $\pm 0.5\ \text{rad}$ . If the system is calibrated with a small amplitude of  $0.1\ \text{rad}$  the system does not overestimate, measuring a higher aberration than the one applied. The slope of the linearity curve is 1 at the origin. With increasing calibration amplitude the system has a range of overestimation of aberrations, before it enters the saturation. This can be an instability factor because in closed loop, when only small aberrations are present, these are overestimated. In case this is known, it can be regulated through a gain factor lower than 1 in the most simple control system, but this will also reduce the saturation level. Having a higher saturation level would be a positive effect of higher calibration amplitudes. These effects may be taken into account with a more complete and complex control system.

The main disadvantage of a calibration with small amplitudes occurs if the deformable mirror, which is used to generate the modes, is not able to deform with high precision at small amplitudes.

The fact that small amplitudes produce small signals increases the noise propagation coefficient for the modes and the condition number<sup>1</sup> of the system will increase.

---

<sup>1</sup>See Appendix C for the definition of condition number

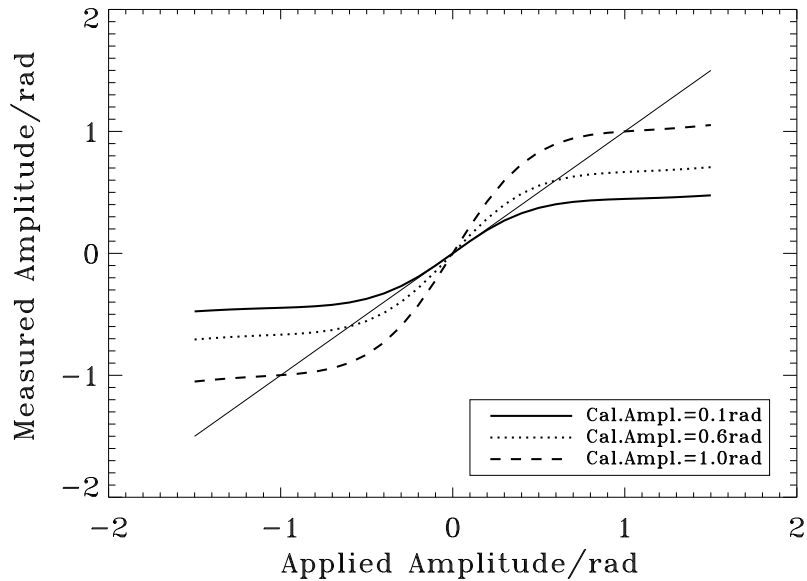


Figure 3.6: Here is shown the behavior in terms of linearity of the sensor, when calibrated with different amplitudes. The measured amplitude is plotted as a function of the applied amplitude. The aberration applied and measured is astigmatism.

### 3.4.3 Modulation

In the optical geometrical approximation the modulation of a PWS plays a central role as it dictates the equivalent focal length of the lenslet array of the Shack–Hartmann wavefront sensor having the same characteristics, at least if the latter is used with a four–quadrant mode to detect the position of the various spots. No modulation translates into infinite focal length and, even in geometrical approximation, this simply means that the signal of the PWS saturates as soon as the first derivative of the wavefront would not be strictly flat. In other words the PWS would be able just to give the sign of the derivative of the wavefront and not any estimation of its amplitude, because, in geometrical approximation, the light spot can be arbitrarily small. Modulation ensures a certain dynamic range prior to the saturation of the signal. In real–world of course spot size is not arbitrarily small and, by heuristic reasoning, it has been shown that sensitivity of a PWS without any modulation is significantly larger than for the Shack–Hartmann sensor (Ragazzoni and Farinato (1999)). Because of the small dynamic range, however, whenever the residual aberrations as seen on the PWS are larger than the dynamic range, some non–linearity will occur leading to a deterioration of the performance. This interesting feature has been studied by Esposito and Riccardi (2001) and it has been shown that, at least under the conditions simulated in the related work, it does usually exist a best modulation amplitude making the magnitude gain the largest as possible.

While we do not investigate here the effects of non–common path aberrations that can lead to a use of modulation to simply avoid to use the wavefront sensor in its saturated regime,

regardless of the above-mentioned consideration, it is to be pointed out that there are some reasons to raise the question if a PWS without modulation can still work at its best conditions, even with a residual aberration different from zero, or, at least, with a small lack of performance. As the absence of modulation is of course a large simplification of the PWS optical design, especially for the multi-wavefront sensors conceived for multi-conjugated AO (MCAO), this is for sure an interesting topic.

Modulation can be seen as the superposition of a tilt made in an *incoherent* way making the spot larger than its original size. The incoherence here is attained by temporal averaging and for this reason, the spot still preserves all the wavefront information. A different technique described in Ragazzoni et al. (2002) uses a coherent modulation by introducing some high order spatial frequencies. These are to be selected in a way to enlarge the spot size but, simultaneously, to avoid to introduce perturbation on the modes that one wants to measure. In other words the content of low spatial frequency should be closely enough to zero so as not to perturb the measurement.

### 3.4.4 Static aberrations

One of the questions that raise with the use of a PWS in the non-modulated regime is for sure the effect of the presence of static aberrations in the non-common path of the sensor. These aberrations must not be corrected, because this would introduce the inverse aberrations into the science path, which should be avoided. It follows then, that this aberrations have to be included, like in other WFSs, in the calibration. In case of a non-modulated PWS, the linear range of the sensor is already reduced, if compared to a modulated one. This linear range also can not be increased to adapt it to the measurement conditions, like in the modulated case. It can only count on the modulating effect of the atmosphere (see Chapter 4), the one possibly coming from other aberrations and the control system.

### 3.4.5 Pyramid roof

One of the main problems in the pyramid manufacture through polishing is the roof-shaped tip (see Section 6.1). This has the effect that the amount of light which hits the pyramid tip is not equally spread into four parts, even with a perfect airy-disk, as explained in Fig. 3.7. Two pupils, formed by two diagonal sides of the pyramid will be more illuminated, what is demonstrated in Fig. 3.8.

This difference in illumination will also vary with the shape and size of the PSF, which makes it difficult to define a normalization factor for the intensities. Most aberrations produce non-symmetric PSFs, and each aberration has a very characteristic shape. If the spot is very extended, as in the case of high aberrated systems, this effect will not be very high, but while the system is correcting the aberrations, the spot-size decreases and the difference in illumination increases.

If the PWS is working in modulated regime the effect of the roof will decrease with the modu-

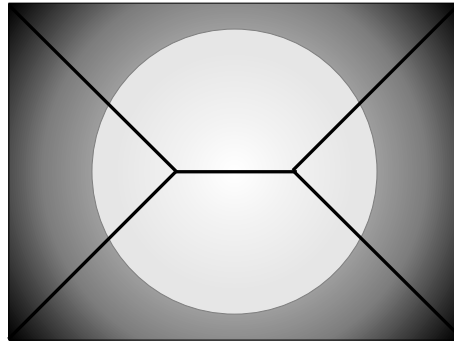


Figure 3.7: A roof-shaped tip of the pyramid leads to a difference in the illumination in the four pupils on the detector, since one diagonal will have more light. This effect will be especially high in a non-modulated PWS and will decrease with modulation amplitude.

lation amplitude and even get negligible, while this is not the case in the static regime.

### 3.4.6 Spatial filter

The positioning of a spatial filter in the focal plane, just in front of the pyramid, has been studied in the laboratory. The main reason for the study of this component has been the reduction of sky background in the PYRAMIR instrument. This has as a consequence of the limitation of the field of view of the sensor. In the case of the CHEOPS wavefront sensor project the pinhole comes in the form of a fully reflective mirror in the focal plane, which transmits most of the light of

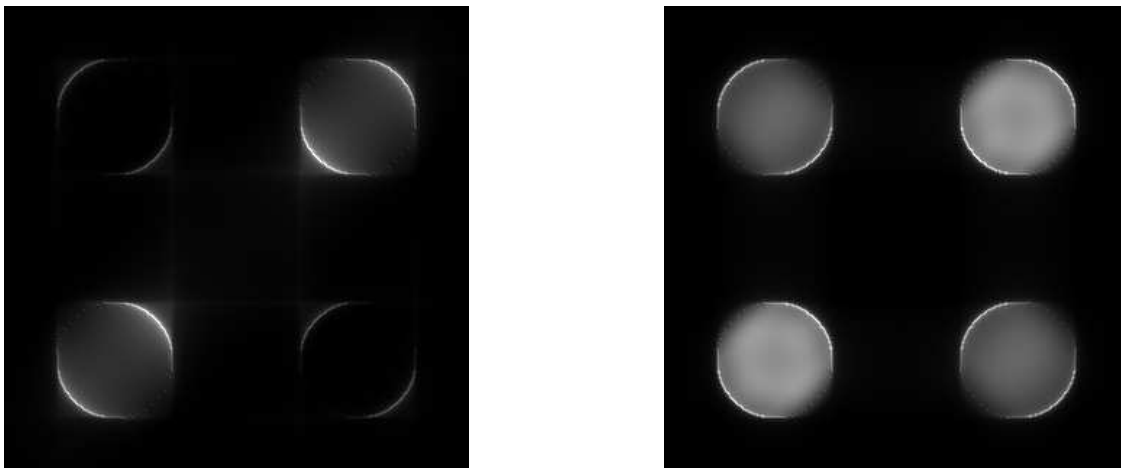


Figure 3.8: A roof-shaped tip of the pyramid generates a different illumination in the four pupils already for a flat wavefront. This effect is demonstrated in the two images above, where the CCD image for a roof of  $100\ \mu\text{m}$  in the case of no modulation (on the left) and modulation of  $2\lambda/D$  (on the right) for a PSF full-width at half maximum of  $107\ \mu\text{m}$ . The roof is located along one diagonal of the images.

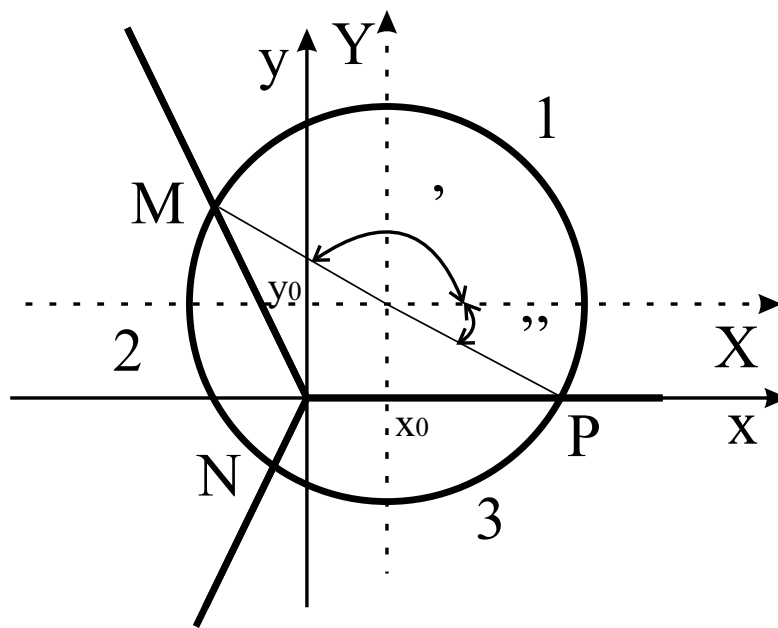


Figure 3.9: This image shows the geometrical approach for the calculation of the expressions for the signals in x and y directions.

the bright central star into the wavefront sensor and reflects the surrounding light, including the one coming from possible faint companions, to the science camera (Feldt et al. (2004)). This filter can only be used with the PWS in non-modulated regime or by also modulating the aperture.

The effect of such a spatial filter is the filtering out of spatial frequencies above a certain value given by the size of the aperture, reducing their power. If this size is chosen according to the wavefront sensors spatial frequency limit (due to spatial sampling), the high frequencies, which are not seen by the sensor will be filtered out. These high frequencies have the unpleasant effect of erroneously being seen as low frequencies, corrupting the measurement results. The attempt of correction from the system will be biased producing errors. This effect, called aliasing, can be significantly reduced by this filtering (Poyneer and Macintosh (2004)).

### 3.4.7 Three-sided pyramid

In previous sections the afforded pyramid quality in terms of edge and tip size has been estimated. The specifications given to the manufacturers have been a maximum tip and edge size of  $10\ \mu\text{m}$ . This has not yet been achieved to my knowledge. This difficulty led to a search for other solutions. The manufacture of a pyramid with three sides presents less difficulties in the quality of the tip, because the over-polishing of one of the sides will not lead to a roof, like in the four-sided case. The information about the derivative in two perpendicular directions is especially intuitive in the four-sided case, but it is also possible to extract it from the three pupils in the three-sided case.

To deduce the expressions for signal calculation<sup>2</sup>, the geometrical approach of a beam modulated around the tip of a three-sided pyramid was used. Two coordinate systems are used: CS1  $(x, y)$  centered on the tip of the pyramid and CS2  $(X, Y)$  having its origin on the center of the circular movement.  $x_0$  and  $y_0$  are the coordinates of the center of the circular movement of the spot in CS1, which are proportional to the slopes of the wavefront  $W$  in both directions. The amplitude of modulation is  $r$ , so it can be written:

$$X^2 + Y^2 = r^2 \Leftrightarrow (x - x_0)^2 + (y - y_0)^2 = r^2. \quad (3.26)$$

The coordinates of M, the point where the beam crosses the edge between face 1 and face 2 (see Fig. 3.9), can be found using:

$$Y = \underbrace{-\sqrt{3}}_a X - \underbrace{(y_0 + \sqrt{3}x_0)}_b \quad (3.27)$$

and substituting this in Eq. 3.26. Taking the negative root one gets an expression for  $X^M$  in terms of  $a$ ,  $b$  and  $r$ :

$$X_-^M = \frac{-ab - \sqrt{(a^2 + 1)r^2 - b^2}}{a^2 + 1} \quad (3.28)$$

The coordinates of N and P are found similarly. The angle subtended by the circumference inside face 1 can be calculated as  $\theta'_1 + \theta''_1$  with:

$$\begin{aligned} \theta'_1 &= \arccos \frac{X_-^M}{r} \\ \theta''_1 &= \arccos \frac{X_+^P}{r}. \end{aligned} \quad (3.29)$$

The ratio of intensity on side 1 by the total intensity is equal to the ratio of the angles:

$$\frac{I_1}{I_{\text{total}}} = \frac{\theta'_1 + \theta''_1}{2\pi}. \quad (3.30)$$

Similar expressions are obtained for  $I_2$  and  $I_3$ . After substituting the expressions for the angles from Eq. 3.29, performing some substitutions and applying some trigonometric relations one gets:

$$\begin{aligned} 2\pi \frac{I_1}{I_{\text{total}}} &= \frac{2\pi}{3} + \arcsin \left( \frac{y_0 + \sqrt{3}x_0}{2r} \right) + \arcsin \left( \frac{y_0}{r} \right) \\ 2\pi \frac{I_2}{I_{\text{total}}} &= \frac{2\pi}{3} + \arcsin \left( \frac{y_0 - \sqrt{3}x_0}{2r} \right) - \arcsin \left( \frac{y_0 + \sqrt{3}x_0}{2r} \right) \\ 2\pi \frac{I_3}{I_{\text{total}}} &= \frac{2\pi}{3} - \arcsin \left( \frac{y_0 - \sqrt{3}x_0}{2r} \right) - \arcsin \left( \frac{y_0}{r} \right) \end{aligned} \quad (3.31)$$

---

<sup>2</sup>Parts of the deduction of the formulas in this section have been done with the help of a private communication of A. Riccardi.

This allows to determine the position of the center  $(x_0, y_0)$ , which corresponds to the slope of the wavefront times the focal length  $(f \frac{\delta W}{\delta x}, f \frac{\delta W}{\delta y})$ :

$$\begin{aligned} x_0 &= \frac{2\pi r}{3\sqrt{3}} \left( \frac{I_1 - 2I_2 + I_3}{I_{\text{total}}} \right) \\ y_0 &= \frac{2\pi r}{3} \left( \frac{I_1 - I_3}{I_{\text{total}}} \right). \end{aligned} \quad (3.32)$$

The signals expressions for the signals calculated from the intensities in the three pupils are proportional to the slopes and can be defined as:

$$\begin{aligned} S_x &\equiv \frac{4}{3\sqrt{3}} \left( \frac{I_1 - 2I_2 + I_3}{I_{\text{total}}} \right) \\ S_y &\equiv \frac{4}{3} \left( \frac{I_1 - I_3}{I_{\text{total}}} \right). \end{aligned} \quad (3.33)$$

The multiplicative constants have been chosen in a way to have

$$f \frac{\partial W}{\partial x} = \frac{\pi r}{2} S_x \quad f \frac{\partial W}{\partial y} = \frac{\pi r}{2} S_y \quad (3.34)$$

as in the four-sided case (see Eq. 3.4 where  $a_0 = rf$ ).

### Error propagation

The error in the signals due to photon noise can be calculated in the same way as has been done for the four-sided pyramid case in Section 3.1.1. The corresponding expression for the three-sided case is:

$$\sigma_{S_{x,y}}^2 = \frac{32}{27N}, \quad (3.35)$$

being slightly higher than for a four-sided pyramid.

The error on the signal due to readout noise  $\sigma_{\text{RN}}^2$  can be estimated:

$$\sigma_{S_{x,y}}^2 = \frac{32\sigma_{\text{RN}}^2}{9N^2}, \quad (3.36)$$

in this case being slightly lower than for the four-sided case.

The total error on the slope estimation due to photon noise and detector readout noise is in this case:

$$\sigma_{\frac{\delta W}{\delta x,y}}^2 = (\pi r)^2 \left( \frac{8}{27N} + \frac{8\sigma_{\text{RN}}^2}{9N^2} \right). \quad (3.37)$$

In case photon noise is the dominant source of error a three-sided pyramid will have a higher total error than a four-sided pyramid.



# Chapter 4

## The Modulation of the Atmosphere

The pyramid wavefront sensor in its original form works with a mechanical modulation, generally introduced by a tip-tilt mirror in the pupil plane, which moves the focus over the faces of the pyramid at least once during a single integration of the detector. The amplitude of this light-spreading adapts the linear range of the sensor to the seeing and sensing conditions.

In this chapter it is shown, for adaptive optics systems working in an astronomical context, i.e., under the influence of the atmosphere, how the aberrations produced by the atmospheric turbulence, which are not seen by the sensor due to its limited temporal bandwidth, act as a modulation. These have the same effect of increasing the linear range and localizing the measurement as the mechanical modulation. In this way the impact of residual wavefront aberrations is estimated for some example conditions of telescope diameter, system bandwidth, wind velocity and Fried parameter (Costa (2004)).

An astronomical verification of the ability to close the adaptive optics loop without mechanical modulation and a comparison with the modulated case is described at last. It was done with the PWS of the Telescopio Nazionale Galileo, a 4m class telescope sited at the observatory of Roque de Los Muchachos, La Palma, Canary Islands (Costa et al. (2003b)).

### 4.1 Introduction

The key point in this chapter is that residual aberration can play the role of modulation in a *natural* way. It is clear, from the reasoning given in section 3.4.3, that to avoid saturation and hence non-linearity effects one would need modulation proportional to the amount of residual aberrations in closed loop. On the other hands the residual aberrations are, by definition, proportional to the residuals. Not all the residuals are useful, however. We can distinguish phenomenologically the following two:

- Aberrations at temporal frequencies larger than the ones sensed by the PWS. These automatically can play the role of *natural* modulation and their strength is dictated by the number of corrected modes and by the spectrum of turbulence;

- Aberrations sensed by the wavefront sensor and only partially corrected. In this case still these can play the role of natural modulation.

All the considerations made here alone are not, of course, enough to establish firmly if modulation can be avoided at all (on the other hand it can be easily seen that by building a turbulence spectrum *ad-hoc* there is clearly need of modulation in a number of occasions) but provides some physical means on which basis a similar result can be founded.

In Section 3.2 the concept of modulation and its effect on the signals given by the sensor has been presented. Here, in Section 4.2 a model is developed to describe how the residual aberrations, not sensed by the PWS due to its temporal bandwidth, can act as a natural modulation. Then, in Section 4.3 we perform a quantitative analysis, giving some examples on the size of this effect. At last, in Section 4.4 the telescope verification results are described.

## 4.2 A model to describe the natural modulation

To understand the effect of modulation on the PWS it is enough to study the more simple case of modulation on a knife-edge sensor.

One can decompose the phase in the pupil  $\phi(x, y; t)$  in polynomial terms:

$$\phi(x, y; t) = \sum_n c_n(t) A_n(x, y), \quad (4.1)$$

where the  $A_n(x, y)$  are a complete set of functions, which are orthogonal over a unit circle and  $c_n(t)$  are the time-varying coefficients. We assume that the functions  $A_n(x, y)$  have a diagonal covariance matrix (like Karhunen-Loeve polynomials). For every  $c_n$  there is a gaussian distribution with a variance  $\sigma_n$  for each  $c_n$ , which gives the probability of finding a certain value:

$$P(c_n) = \frac{1}{\sigma_n \sqrt{2\pi}} \exp\left(-\frac{c_n^2}{2\sigma_n}\right). \quad (4.2)$$

We know that the measured signal is obtained from the integration of the signal during an amount of time  $T$ . So we can separate  $\phi(x, y; t)$  in two parts: One which almost does not change on time-scales smaller or equal to  $T$  and therefore is "static" and can be measured, the other one which changes in a statistical way in such time-scale (and can't be measured).

Let us therefore separate  $\phi(x, y; t)$  in two parts:

$$\phi(x, y; t) = \phi_s(x, y) + \sum_j c_j(t) A_j(x, y). \quad (4.3)$$

Here  $\phi_s(x, y)$  is the part, that can be measured (because it almost does not change during  $T$ ). The second term is the part of the phase, which can not be measured with our sensor because of temporal limits.

For the mean value of the signal over one measurement cycle we get

$$\langle S_x(x, y) \rangle = \frac{1}{T} \int_0^T dt S_x(x, y; t). \quad (4.4)$$

Substituting Eq. 3.14, the expression for the signals in the pupils of a knife-edge wavefront sensor, where the knife-edge is located along the y-axis, and Eq. 4.3, and replacing the integral over time by an integral over all possible configurations of  $c_j$ , multiplied by their probability, we get:

$$\begin{aligned} \langle S_x(x, y) \rangle &= \frac{1}{C} \int_{+\infty}^{-\infty} \prod_j dc_j \frac{1}{\pi} \int_{-B(y)}^{B(y)} dx' p.v. \frac{\sin [\phi_s(x', y) - \phi_s(x, y)]}{x' - x} \\ &\times \cos \left\{ \sum_j c_j [A_j(x', y) - A_j(x, y)] \right\} \exp \left( - \sum_j \frac{c_j^2}{2\sigma_j} \right). \end{aligned} \quad (4.5)$$

This can be written as

$$\langle S_x(x, y) \rangle = \frac{1}{\pi} \int_{-B(y)}^{B(y)} dx' p.v. \frac{\sin [\phi_s(x', y) - \phi_s(x, y)]}{x' - x} \times M(x', x, y), \quad (4.6)$$

where the "modulation"  $M(x', x, y)$  is

$$M(x', x, y) \equiv \frac{\prod_j}{C} \int_{-\infty}^{+\infty} dc_j \exp \{ ic_j [A_j(x', y) - A_j(x, y)] \} \exp \left( - \frac{c_j^2}{2\sigma_j} \right). \quad (4.7)$$

It should be noted that Eq. 4.6 and Eq. 4.7 are similar to Eq. 3.16, the expression for the signals in the pupils in the modulated case.

With  $\int_{-\infty}^{+\infty} dc \exp \left( - \frac{c^2}{2\sigma} + icA \right) \propto \exp \left( - \frac{\sigma A^2}{2} \right)$ , one gets

$$M(x', x, y) = \exp \left\{ - \sum_j \frac{\sigma_j}{2} [A_j(x', y) - A_j(x, y)]^2 \right\}. \quad (4.8)$$

Clearly, the modulation function satisfies  $M(x, x, y) = 1$  and  $M(x', x, y) \leq 1$  and if  $\sigma_j \neq 0$  for several  $j$ ,  $M$  has the effect of cutting off the integral for large  $x' - x$ , linearizing the  $\sin[\phi_s(x', y) - \phi_s(x, y)]$  in the integral, so that

$$\langle S_x(x, y) \rangle \rightarrow C \frac{d\phi_s(x, y)}{dx}, \quad (4.9)$$

for a constant  $C$ . This is exactly the same as the effect of a "mechanical" modulation.

### 4.3 A quantitative estimation of the atmospheric modulation effect

To make a quantitative estimate of the shape of the modulation function defined in the previous section, we calculate the temporal power spectrum of each Zernike mode (Conan et al. (1995)), where  $\nu$  is the temporal frequency and  $\nu/V$  the spatial frequency  $f_x$ :

$$w_{Z_j}(\nu) = 0.033 \frac{C_N^2 dh}{V} (2\pi)^{-2/3} \left(\frac{2\pi}{\lambda}\right)^2 \int_{-\infty}^{+\infty} df_y \left| \tilde{Z}_j\left(\frac{\nu}{V}, f_y\right) \right|^2 \left[ \left(\frac{\nu}{V}\right)^2 + f_y^2 \right]^{-11/6} \quad (4.10)$$

where  $\tilde{Z}_j(f_x, f_y)$  is the fourier transform of the  $j^{\text{th}}$  Zernike polynomial  $Z_j(x, y)$ ,  $(f_x, f_y)$  is the spatial frequency vector  $f$ , and  $n$  and  $m$  are the radial degree and the azimuthal frequency, respectively:

$$|\tilde{Z}_j(f_x, f_y)| = (n+1)^{1/2} \frac{2 |J_{n+1}(\pi D f)|}{\pi D f} \begin{cases} \sqrt{2} |\cos(m\theta)| & , m \neq 0 \\ \sqrt{2} |\sin(m\theta)| & , m \neq 0 \\ 1 & , m = 0 \end{cases} \quad (4.11)$$

The wind velocity  $V$  is taken along the  $x$  direction (to generalize to any wind direction one just has to rotate the axes, so that the new  $f_x$  is parallel to the wind direction). The Taylor hypothesis of frozen turbulence is assumed. The index structure coefficient is  $C_N^2$ , the layer thickness is  $dh$  and the wavelength  $\lambda$ .

To get the residual variance,  $\sigma_j$ , Eq.4.10 has to be weighted with the error transfer function square modulus  $|T(\nu)|^2$  and integrated:

$$\sigma_j = \int_{-\infty}^{+\infty} |T(\nu)|^2 w_{Z_j}(\nu) d\nu, \quad (4.12)$$

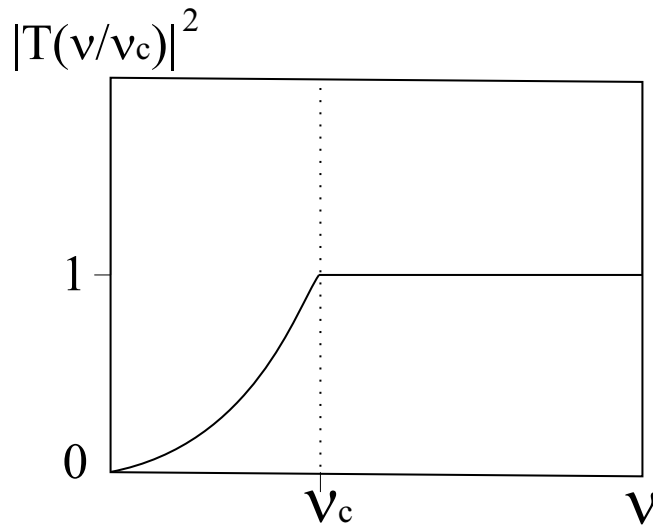


Figure 4.1: The square modulus of the error transfer function for a system with bandwidth  $\nu_c$ .

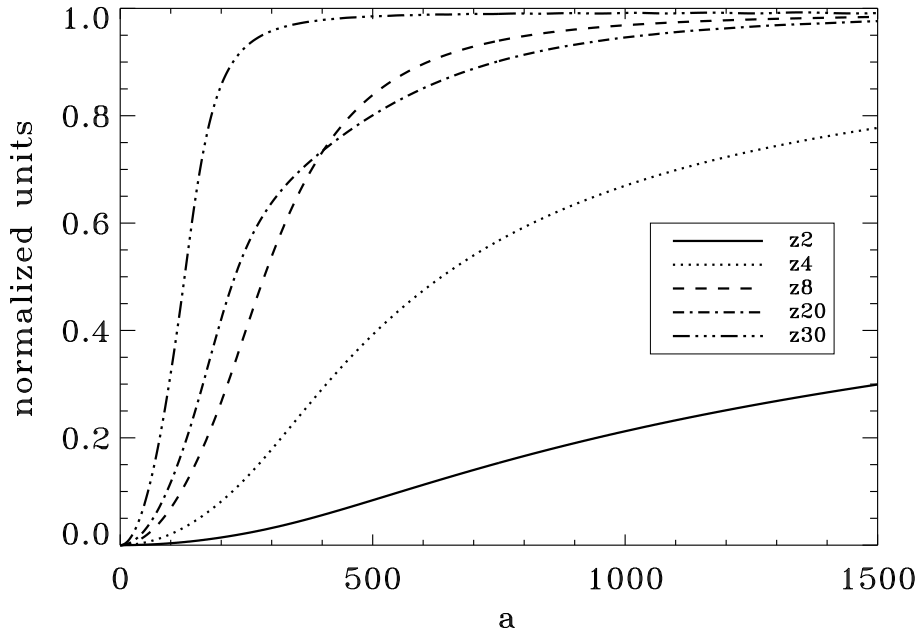


Figure 4.2: Normalized residual variance  $\sigma_j/(\Delta_j - \Delta_{j+1})$  for some Zernike polynomials as a function of  $a$ , the ratio of the wind speed over the system bandwidth multiplied by the telescope diameter ( $a = V/(\nu_c D \pi)$ ).

where we take:

$$\left| T\left(\frac{\nu}{\nu_c}\right) \right|^2 = \left(\frac{\nu}{\nu_c}\right)^2 \theta \left[ 1 - \left(\frac{\nu}{\nu_c}\right)^2 \right] + \theta \left[ \left(\frac{\nu}{\nu_c}\right)^2 - 1 \right]. \quad (4.13)$$

Here  $\nu_c$  is the system bandwidth and  $\theta$  represents the step function, which is 0 for negative input values and 1 elsewhere. The function  $T$  is represented in Fig. 4.1.

This means that there will be a residual contribution to the error from frequencies  $\nu < \nu_c$ . Frequencies with  $\nu > \nu_c$  contribute with weight 1. In practice what we did was to calculate

$$\sigma_j = \frac{\int_{-\infty}^{+\infty} |T(\nu)|^2 w_{Z_j}(\nu) d\nu}{\int_{-\infty}^{+\infty} w_{Z_j}(\nu) d\nu} (\Delta_j - \Delta_{j+1}) \quad (4.14)$$

with  $\Delta_j$  given by the Zernike-Kolmogoroff residual errors (Fried (1965); Noll (1976)):

$$\Delta_j \approx 0.2944 j^{-\sqrt{3}/2} \left(\frac{D}{r_0}\right)^{5/3}. \quad (4.15)$$

Here  $D$  is the telescope diameter and  $r_0$  is the Fried parameter. This can be done because  $\int_{-\infty}^{+\infty} w_{Z_j}(\nu) d\nu = (\Delta_j - \Delta_{j+1})$  and it allows to drop all the constants outside the integrals. For

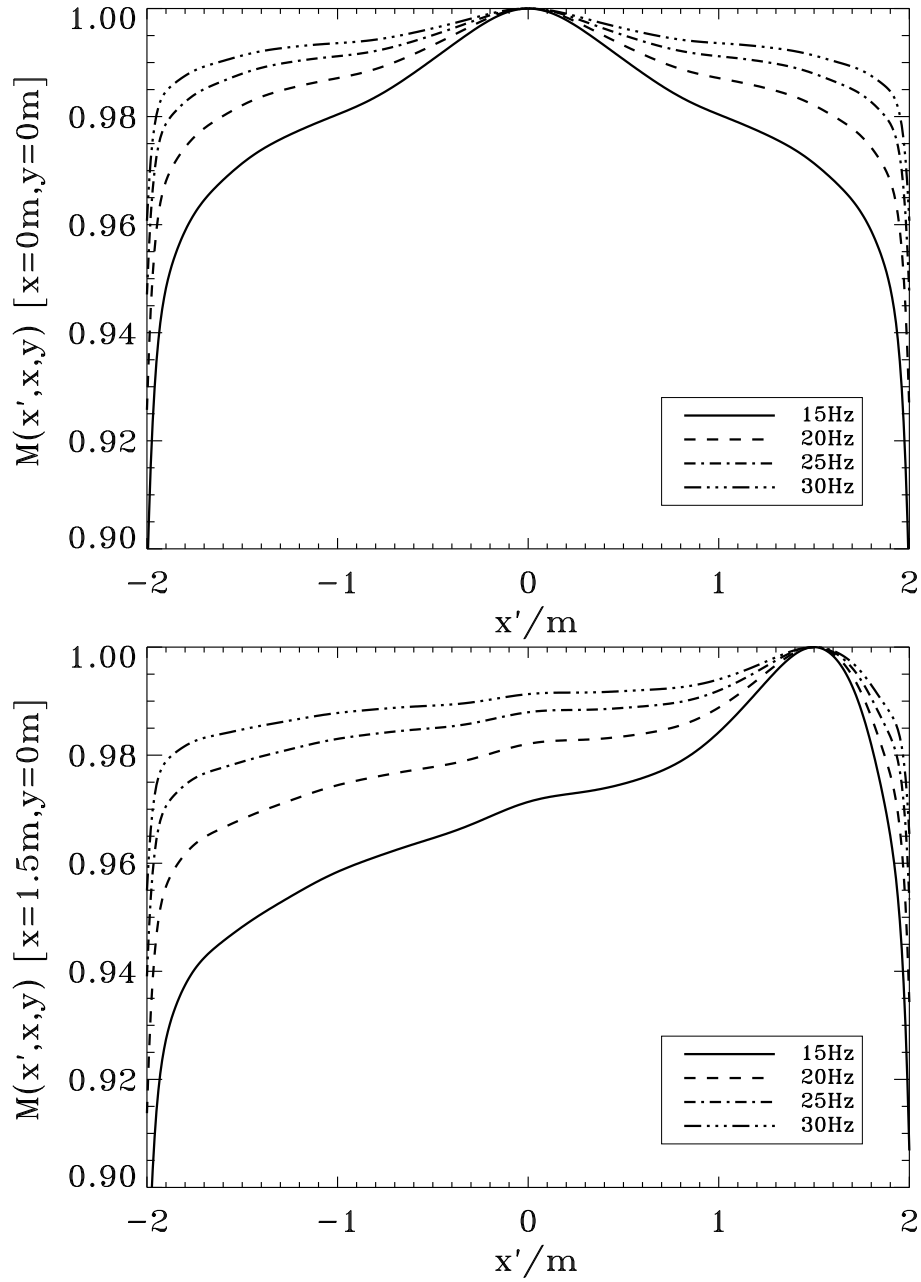


Figure 4.3: Modulation function across the telescope aperture (in the pupil center represented in the upper figure, and at point  $(x=1.5\text{ m}, y=0\text{ m})$  in the lower figure) for different system bandwidths  $\nu_c$ , for a telescope diameter of 4 m, wind velocity of 30 m/s and an  $r_0$  of 1 m.

the derivation and numerical integration of the equations refer to Appendix A at the end.

The modulation function obtained depends on a variable, that we define as  $a = V/(\nu_c D \pi)$ , and on  $Dr_0^5$  (see Appendix B). Its effect will increase with higher wind velocity  $V$ , and decrease with bigger telescope diameters ( $D$ ), higher  $r_0$  (better seeing) and higher system bandwidth  $\nu_c$ . This can be seen in Fig. 4.2, where the normalized residual variance for different Zernike modes,

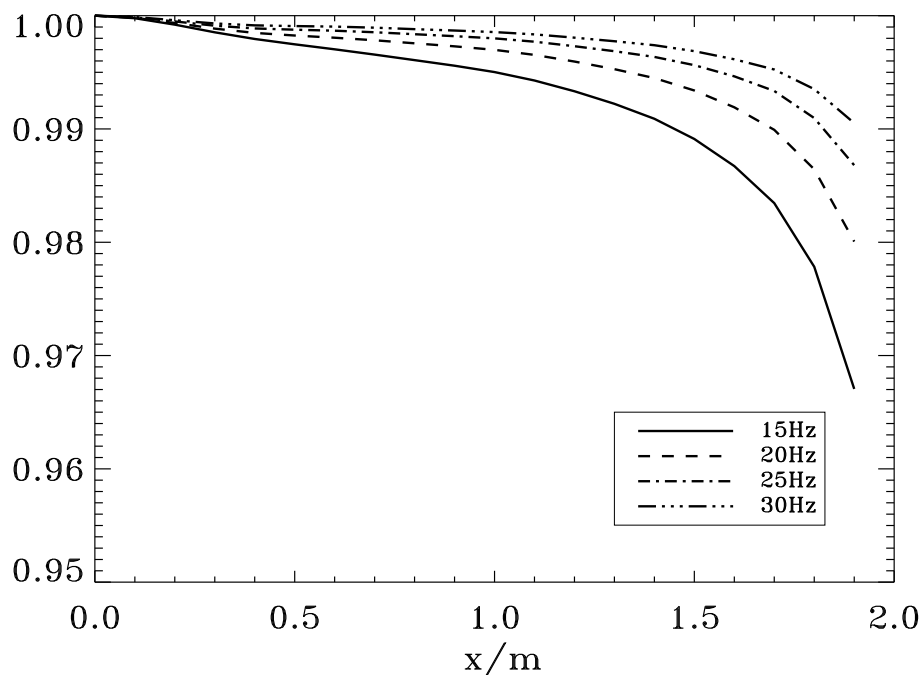


Figure 4.4: Integrated modulation function across the telescope aperture for different points along the  $y=0$  chord, normalized with the integral at  $(x=0\text{ m}, y=0\text{ m})$ , for different system bandwidths  $\nu_c$ , for a telescope diameter of 4 m, wind velocity of 30 m/s and an  $r_0$  of 1 m.

as a function of  $a$ , is plotted. We also plotted the modulation function in certain different conditions, and made a mapping over the pupil for two different pupil positions (see Fig. 4.3 as an example).

We integrated the modulation function across the pupil chord for the plots presented excluding the point, where it has the value 1, normalizing it with the integral of the modulation function at the pupil center, and we show the results in Fig. 4.4. The value obtained gives an estimate of the suppression of the contribution of points on the same chord to the signal. The modulation effect does not change more than 1–2 percent over the pupil, at least under the conditions simulated. It shows a slightly greater modulation effect at the edges of the pupil. In future it should be further analyzed, if this could have a physical meaning or if it could be due to numerical approximations.

Here we have used Zernike modes, neglecting the non-zero terms in the covariance matrix. The numerical analysis is done in the same way with Karhunen-Loeve polynomials, but we expect no significant difference in the magnitude of the modulation obtained.

For comparison with the mechanical modulation, we plotted in Fig. 4.5 the atmospheric modulation in certain conditions and the effect of a tilt modulation with different amplitudes in  $\lambda/D$  units. The size of the diffraction limited spot on the pyramid tip corresponds to  $1\lambda/D$ . To move the complete spot over all the pyramid sides the smallest amplitude is  $0.5\lambda/D$ . In the conditions simulated, the atmospheric modulation effect is comparable to a mechanical modulation of  $0.2\lambda/D$ .

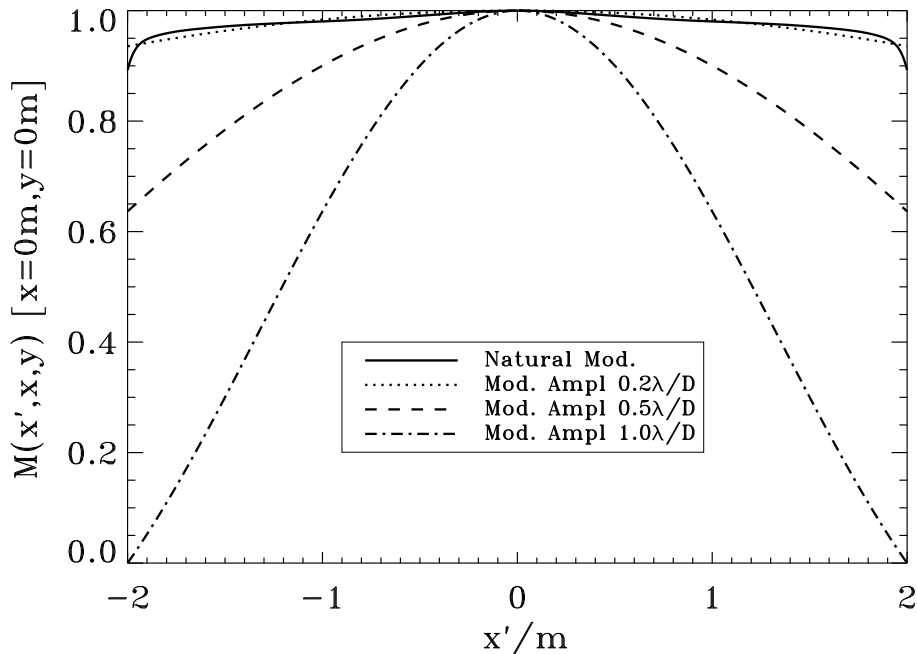


Figure 4.5: Modulation function for a telescope with diameter of 4 m, with a wind velocity of 30 m/s, with  $r_0=1$  m and a system bandwidth of 15 Hz (for  $x = 0, y = 0$ ) (solid line). For comparison we have also plotted the mechanical modulation function for different modulation amplitudes in  $\lambda/D$  units (dashed lines).

## 4.4 Experimental Verification with real Stars

The experimental verification was performed on sky with the PWFS of the 4m class Telescopio Nazionale Galileo (TNG), sited at the observatory in La Palma, Canary Islands. The adaptive optics module of TNG, AdOpt@TNG, is the only AO system that currently implements a pyramid as a wavefront sensor for AO, and its latest performances show that this kind of sensor is comparable to the wavefront sensors normally mounted on other AO systems (Ghedina et al. (2003)).

We choose for the purposes of our test a set of 8 stars with scaling magnitudes from 5.4 to 9.2 and for each of them we took a series of closed loop images, alternatively switching off and on the modulation of the pyramid. The pyramid of AdOpt@TNG is mounted on an XY stage, and to introduce or not the modulation is an immediate task. In this way the elapsed time between the two different measurements (with and without modulation) on the same star was negligible: this assures the same overall conditions of the system during the test.

On the pin of the pyramid at the plate scale of AdOpt@TNG, being the effective F ratio  $F/32$ , and at the effective wavelength of sensing ( $\lambda = 800$ nm), the modulations of  $\pm\lambda/D$  corresponds

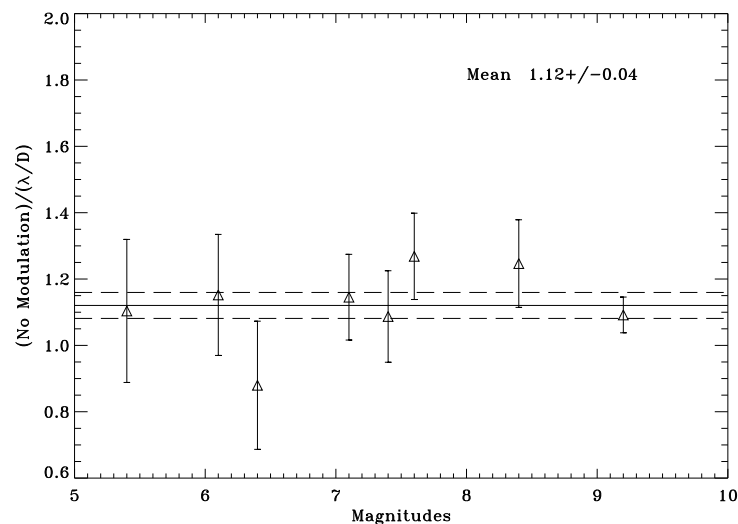
	Star Name	mV	Date	Time(UT)
1	HR3951	5.4	27/04/02	21:42
2	HR4550	6.1	27/04/02	22:35
3	HR5415	6.4	27/04/02	00:50
4	HR5280	7.1	27/04/02	01:38
5	HR5414	7.6	27/04/02	02:01
6	HD149662	7.4	27/06/02	23:09
7	HD149561	8.4	27/06/02	23:35
8	HD149579	9.2	28/06/02	01:29

Table 4.1: Stars observed for the test of the Pyramid Wavefront Sensor

to a circular modulation with diameter  $\approx 51\mu\text{m}$ . Amplitude and frequency of the modulation were checked with an oscilloscope to correspond to the desired values.

Actually we split the pupil on the CCD into  $\approx 8 \times 8$  subapertures, although correction was performed only up to the first 14 K-L polynomials. Accordingly to the number of corrected polynomials we could have sampled the pupil at  $4 \times 4$  but we used the standard observational mode of AdOpt@TNG.

The differences in performance were calculated by direct Strehl measurements on the scientific cameras, and for every measurement we took several Strehl data with and without the modulation of the pyramid, but, as we said before, within a negligible amount of time between one measurement and the following.

Figure 4.6: Ratio of S for no modulation versus  $\lambda/D$  modulation. Mean value is  $\approx 1.12 \pm 0.04$ .

To override in the analysis of the results some problems due to the change of the atmospheric and instrumental observing conditions we decided to explore only the ratio between the Strehls and not their absolute values, referring the no-modulation data to the data of the  $51\mu\text{m}$  amplitude as it can be seen in Fig.4.6.

A fit of the experimental data of Fig.4.6 shows that the PWS performs marginally better, being the mean value of the ratio  $1.12 \pm 0.04$ , when there is no dynamic modulation of the pyramid. Anyway we have to point out that, as described in the theory, the residual of the correction on the pin of the pyramid can be considered as a modulation itself, from which it seems straightforward that it is better to not modulate. However we have always been during the observations in the condition that the correction was not full but limited, that is far from the diffraction limit on the pin of the pyramid, a regime where maybe other diffraction effects could play an important role.

## 4.5 Results

It was shown through analytically and numerically that the residual aberrations of the atmospheric turbulence not seen by the sensor due to the systems limited temporal bandwidth can themselves act as a modulation, contributing to the linearization of the signal. This effect can be numerically estimated for each condition of telescope diameter, atmospheric conditions (wind velocity and  $r_0$ ) and system bandwidth. The comparison of this "natural" modulation with a mechanical modulation of the PWS signal shows that in certain conditions they may have comparable effects.

It is known that modulation allows a better localization of the signal measured, approaching the PWS to a local slope sensor. This will be naturally, and unavoidably, increased by the atmospheric turbulence, with its potentially good effects, like the increased linear range of the sensor, and bad effects, where one of them is the loss of the delocalized information. The ability to use this information is actually one of the potential advantages of the PWS in non-modulated regime.

Here we only estimate the effect of one atmospheric layer, while it can in the same way be generalized to more layers, what will of course increase the modulation effect.

It would be interesting to further investigate, where the point lies in which the non-linearities do not allow to close the adaptive optics loop anymore, which is equivalent to how much modulation is needed in each case. For every case, when the optimal modulation amplitude is estimated, it should be taken into account the natural one, which might be enough, especially in cases where the common path aberrations, enlarging the spot on the pyramid and therefore imposing a greater linear range, are small.

A further analysis of the effect of modes not seen due to the spatial sampling of the sensor would also be very interesting at this point.

At the telescope the experiment of closing the loop and comparing the achieved Strehl Ratio with a mechanically modulated and an only atmospherically modulated PWS was performed. The modulation amplitude was relatively small, of the order of  $0.5 \lambda/D$ . Even though the results shows a slight advantage in the mechanically non-modulated case, what supports the theory that atmospheric modulation is at least not far from the optimum.



# Chapter 5

## Laboratory setup and simulation technique

The laboratory experimental setup has been developed with the purpose of testing the PWS working in different conditions, as well as gaining experience for the development and construction of the PYRAMIR instrument.

First the laboratory setup and its components are described and characterized. The techniques developed for calibration of the system and for measurement of aberrations are explained. The system is able to perform open-loop measurements as well as static closed-loop corrections.

A simulation of a complete adaptive optics system using a PWS, which models the adaptive optics correction loop with its different components and in different stages is described next. The simulated adaptive optics loop works in open-loop or closed-loop real-time correction of the atmosphere.

### 5.1 Description of the laboratory system

#### 5.1.1 Optical setup and hardware

The light source for our pyramid wavefront sensor in the laboratory setup, sketched in Fig.5.1, is the He–Ne laser connected to a Twyman–Green interferometer, providing a light beam with a wavelength of  $\lambda = 632.8 \text{ nm}$ , used with an objective, which has an aperture diameter of 50 mm. A field stop with 9 mm determines the diameter of the beam. The parallel light beam illuminates our deformable mirror (DM), wherefrom it is reflected back to the interferometer, so that the actual shape of the mirror can be seen at any time. In this configuration the shape of the mirror provokes a static defocus, which is corrected optically in the design by a shift of the DM along the optical axis of the beam. The remaining static aberrations are corrected through a flattening routine described at a later point in this chapter.

Through a 50/50 beamsplitter the light coming from the DM is separated into the WFS. A

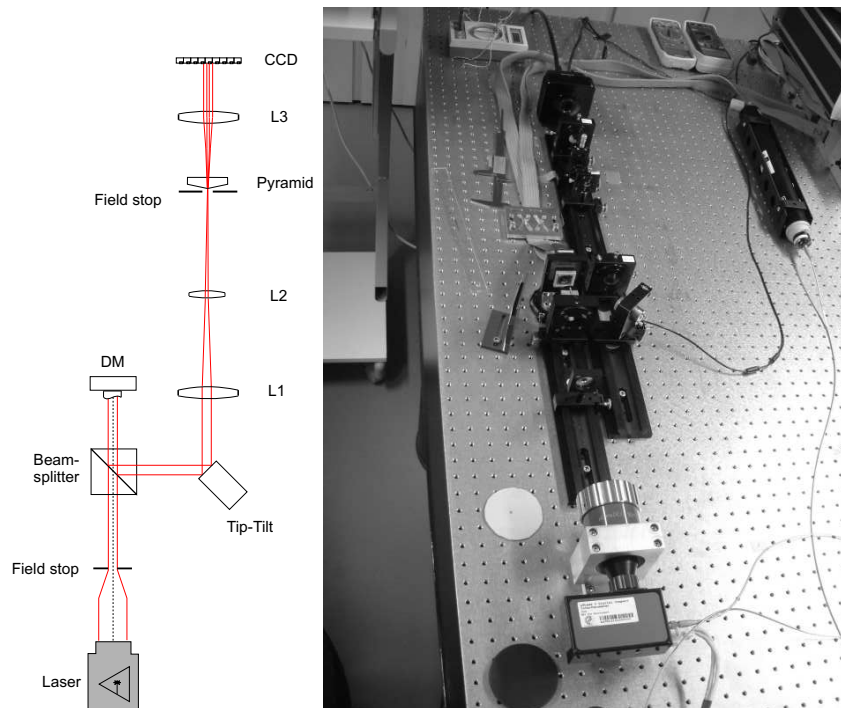


Figure 5.1: A schematic representation of the laboratory setup together with a photograph.

tip-tilt mirror allows us to use the system also with a dynamic modulation, as was done in the previous setups (Esposito et al. (2000a)). Two lenses form an F/170 beam, which is focussed on the tip of a glass pyramid. The choice of the F-ratio leads to a spot size of approximately  $100\ \mu\text{m}$  on the pyramid tip, which is comparable to the spot size in the PYRAMIR instrument. This allows to have the same effect of light loss in both cases (refer to Section 6.2 for details on light loss through the edges of the pyramid). The lenses used are achromatic lenses, where the second one is a Barlow lens. This was necessary, despite the considerably higher optical adjustment precision necessary, because the optical setup had to be kept within certain space limits.

The pyramid surfaces form a relatively small angle of  $0.57\text{deg}$  with the focal plane and the material is BK7 glass. The quality of the tip and of the surfaces was measured with a profilometer. The roof size has been estimated to  $19\ \mu\text{m} \times 46\ \mu\text{m}$  (see Section 6.1). There is the choice of introducing a field stop with variable diameter immediately before the pyramid. The four beams are re-imaged on a CCD through a third achromatic lens. Each of the four pupils has an optically defined diameter of 80 pixels, but the camera pixels can be re-binned, so that a different number of pixels per diameter is obtained. The camera and the DM are in conjugated planes, so that the wavefront introduced by the mirror surface is re-imaged on the CCD.

### The interferometer

The interferometer used is a  $\mu\text{Phase 2 HR Digital Compact Twyman Green}$  interferometer from FISBA Optik. In the experimental setup it is used as light source and as independent reference

wavefront sensor. The He–Ne laser provides a light beam with a wavelength of  $\lambda = 632.8$  nm. Various objectives are provided with the interferometer. For the setup the objective, with an aperture diameter of 50 mm was used. In this configuration the interferometer image of the DM has 175 pixels per diameter.

### The deformable mirror

The DM is a micromachined membrane deformable mirror from OKO Technologies (first described in Vdovin (1996)) with 15 mm diameter of mirror surface and 37 control actuators. It has 7 actuators per mirror diameter. The membrane is coated with a layer of gold.

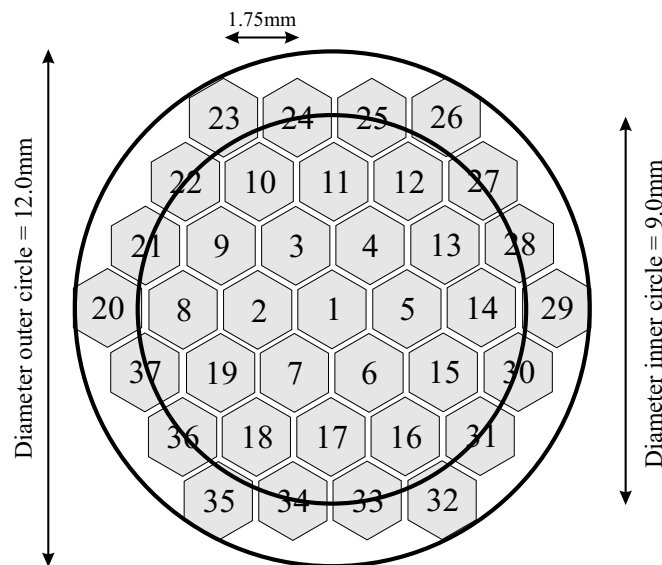


Figure 5.2: The geometry of the actuator array of the deformable mirror. The outer circle represents the active area under the membrane, the inner circle is the illuminated area in our set-up.

The actuators are concentrically distributed under the membrane, as can be seen schematically in Fig. 5.2. The deformation of the membrane is driven by electrostatic forces which are provoked by voltages applied to the actuators. These forces  $F$  can be described with:

$$F = \frac{\epsilon\epsilon_0 V_c^2 A}{d^2}, \quad (5.1)$$

where  $\epsilon\epsilon_0$  is the effective dielectric constant of the medium between the electrodes,  $A$  is their area,  $V$  is the control voltage and  $d$  is their distance. Since  $A \gg d$ , small voltages allow to achieve relatively high forces. To allow deformations in both directions, the mirror can be biased to a constant non-zero voltage. This corresponds to applying an initial voltage to the actuators. In this case, as can be seen in Fig. 5.3, a smaller applied voltage is enough to achieve the same electrostatic force.

The output channels are provided with an 8-bit digital voltage control, which allows a range of

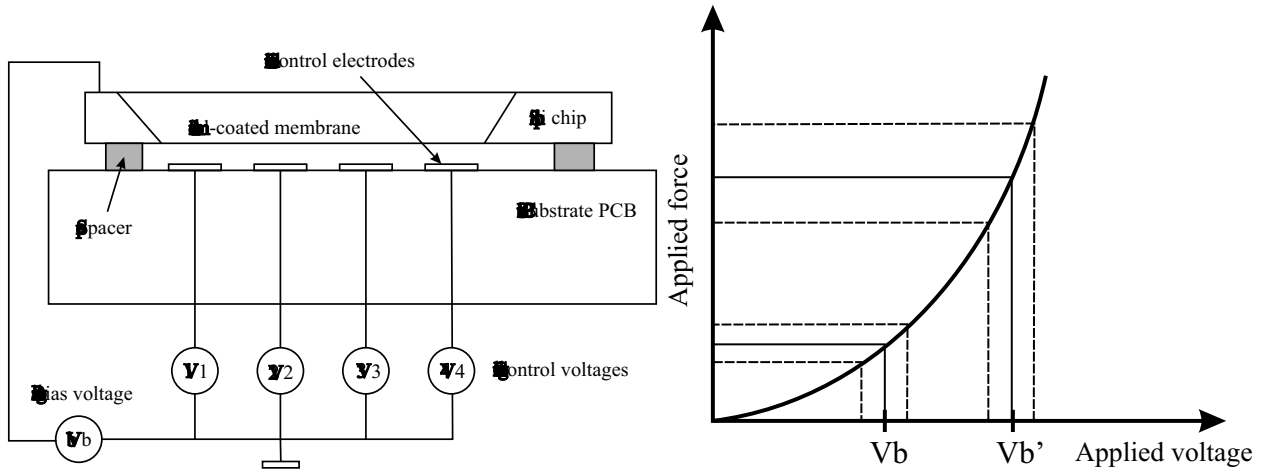


Figure 5.3: On the left a schematic section of the micromachined adaptive mirror (taken from the technical passport). On the right the force on the electrodes by applying a voltage. When biasing is applied, a smaller voltage is enough for achieving the same electrostatic force.

0-255 V for the final desired voltage for each electrode. Since the mirror response to the voltage is not linear, but quadratic, the applied voltage ( $V_{ap}$ ) to the electrodes is scaled according to:

$$V_{ap} = \sqrt{255 \text{ Value}}. \quad (5.2)$$

Here *Value* is the corresponding value calculated for a mirror having a linear behavior. During the calibration of the sensor zernike modes are applied sequentially to the mirror. These modes are mapped on a model of the DM, giving the height of the membrane at the position of each actuator. The voltage applied to each actuator was calculated according to Eq. (5.2). Bias voltage is considered for this calculation, so that the zernike mode is centered within the dynamic range of the mirror.

The deformable mirror is held at approximately half the dynamic range. In this configuration the shape of the mirror provokes a static defocus, which is corrected optically in the design. After applying this correction the DM has a RMS of  $32 \mu\text{m}$ . Since the PWS, when it is not modulated, is very sensitive, the static aberrations left could still be seen in the CCD image as a non-uniform illumination in the four pupils. These static aberrations, which are mainly astigmatism, are corrected through a flattening routine. This procedure consists in taking an interferometer image of the DM at the position of a bias of 64. The surface of the DM is fitted to a perfect zernike defocus and the differences between the fit and the real image are calculated. The corresponding actuator commands are calculated and applied to the DM. This procedure is done sequentially, till a tolerable RMS is achieved. In our case the final RMS is 7 nm. The different images can be seen in Fig. 5.4.

The illuminated circle of the DM corresponds to ca. 56% of the active area (see Fig.5.2). The use of ca. 60% of the active area has shown to be the best choice for the highest number of independent modes (Prieto et al. (2000); Fernández and Artal (2003)). This implies that the

number of actuators inside the illuminated area is only 5 per diameter.

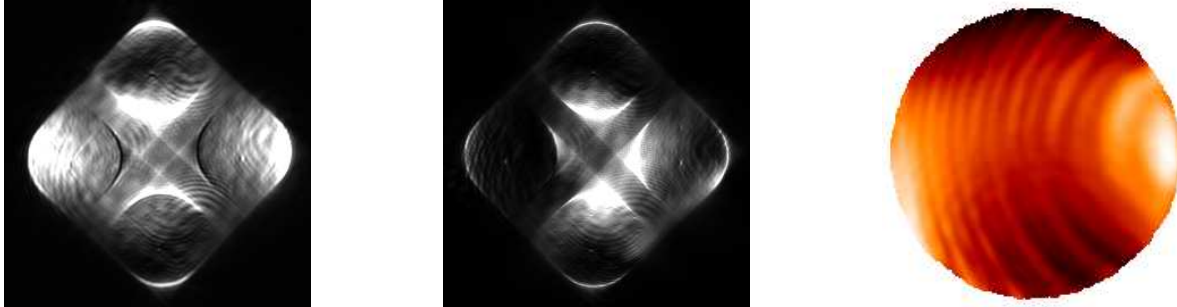


Figure 5.4: From left to right the four pupils on the CCD for the DM biased to a constant value of 64, biased to values obtained through a flattening routine and an interferometer image of the difference between the flattened and biased mirror surfaces.

While this mirror is very useful for laboratory use, especially because of its accessible price and ready to use delivery, it has some drawbacks, which will become clear in the next sections, where the characteristics of the system are described. One of them is the influence function each one of the actuators, which spreads over the full surface. This results in cross-talk between the actuators and does not allow to reproduce accurately zernike modes on the mirror surface linearly. To reproduce the zernike modes correctly on the mirror membrane, a closed-loop fitting routine using the interferometer images (like it was done for flattening the DM) would be a good solution. Also possible is the measurement of the influence functions for each of the actuators with the interferometer. These influence functions allow to construct an interaction matrix, which can be inverted through SVD and used to calculate the voltage that has to be applied to each actuator to achieve a given zernike mode.

On the optical bench the mount of the DM shows a slow but non-systematic permanent shift, an effect which could not be completely eliminated. This provokes that tip and tilt increase during the measurements. This effect can clearly be seen, especially in measurements that are extended in time like the closed loop sequences are. This implies that during a closed loop sequence the results of the measurements of tip and tilt are biased, because they are being corrected by the DM itself in every loop and the accumulated correction of these two modes continuously increases.

### The tip-tilt mirror

The tip-tilt-Mirror is an ultra-fast piezo tip-tilt platform (S-330) including a circular mirror with a diameter of 25 mm from Physik Instrumente GmbH Germany. It is equipped with two pairs of low-voltage piezo-electric linear drives operating as a unit in push/pull mode. The voltage range from 0 – 100 V is divided into values of 0 - 4095 digital units which were applied to the electronic device. The mirror is positioned by two piezoelectric drives, which allow to tilt it in two orthogonal directions.

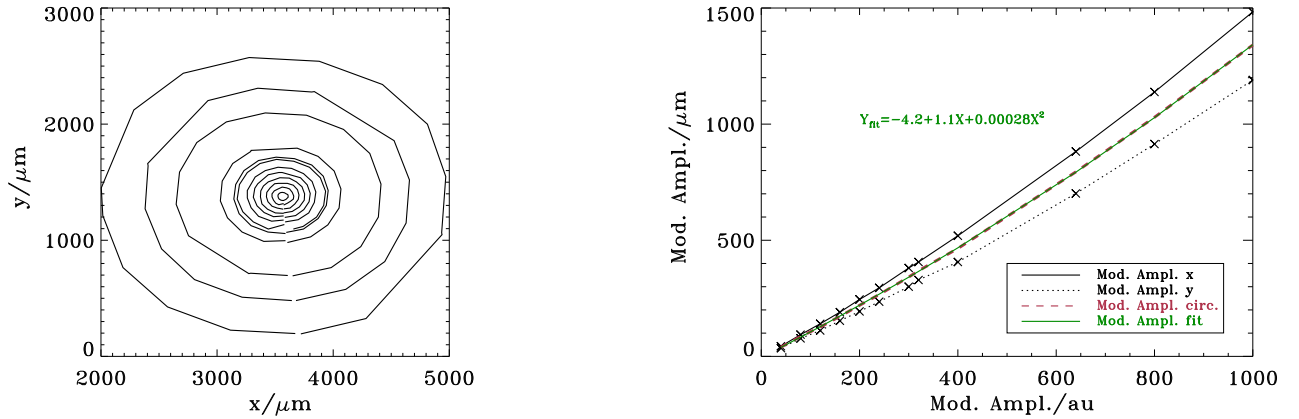


Figure 5.5: The plot on the left side shows the displacement of the focus during one rotation cycle for modulation amplitudes of 40, 80, 120, 160 and 1000 au (digital units). The path of the beam is not a perfect cycle but an ellipse for all modulation amplitudes. On the right side the displacement in  $x$  and  $y$  direction, which are the directions of the axes of the ellipsoid, is shown for the same modulation amplitudes. The equivalent circular radius, which gives a circle with the same perimeter, is also shown. The best fit, which is a polynomial of 2nd degree, is also represented.

The beam was aligned on the optical axis with the mirror set to 2048 digital units, permitting half of the tilting range, which is 2 mrad, in each direction. For modulation of the beam over the pyramid tip, the mirror was programmed to perform circular movements with variable amplitude around the central position. The frequency of the oscillation was dependent on the number of steps performed during one cycle. Maximum step frequency has been used in all experiments. According to the specifications of the tip-tilt platform this maximum frequency is 2.4 kHz. The camera integration time was adapted to the frequency of the oscillation, when measurements with modulation were performed. This avoided the oscillation effect that appears when the integration time is not a multiple of the modulation period (or at least much longer).

The mirror shows a small hysteresis effect when applying sequences of increasing and decreasing voltages to the actuators. This effect has been estimated by Stumpf (2004). It is not expected that it has influence on the results obtained when the sensor is modulated, due to the small size of the effect.

The displacement range of the focus on top of the pyramid is determined by the angular range of the tip-tilt mirror and the combination of lenses before the pyramid. To test the displacement of the beam on the pyramid, the CCD was positioned in the focal plane and images were taken during rotation cycles with different amplitudes. The 2-dimensional displacement of the beam is shown on the left side of Fig. 5.5. It shows that the movement of the beam is not perfectly circular but has the form of an ellipse with the major and minor axes along the  $x$  and  $y$  directions (which are coincident with the edges of the CCD). This is even more evident on the

right side of Fig. 5.5, where the displacements in  $x$  and  $y$ -direction are shown for a number of modulation amplitudes. Both curves diverge even for small amplitudes. Since the ellipsoidal movement is also centered on the pyramid tip, it also stays  $1/4$  of cycle on each side. This is an approximation, which is at least valid if the turbulence is not degrading the spot-shape and spot-size too much and if the eccentricity of the ellipse is not too big. We approximated the modulation amplitude radius as the equivalent radius of a circle which has the same perimeter as the respective ellipse. This curve is also shown in the plot and an approximation to this curve is given. A simply linear approximation would not be such a good approximation for the small amplitudes, which are the ones that we used most. A quadratic polynomial fit is given, which is very near to linear, especially for small modulation amplitudes.

### The spatial filters

A choice of spatial filters can be introduced in the focal plane just before the pyramid tip, partially masking out the outer rings of the PSF. They have been blacked to avoid reflections. This spatial filters have diameters of 0.2 mm, 0.5 mm, 1.0 mm, 2 mm and 5 mm. The filter can also be removed, so that all the light arrives at the pyramid.

### The pyramids

The pyramids tested and used in the laboratory setup were mostly pyramids, which were manufactured for the PYRAMIR instrument. Our requirements, explained in Section 6.1 and in Chapter 7, were very challenging for the standard polishing techniques. They are shown in Tab. 5.1, together with the characteristics of the pyramid used in the setup. It is a BK7 four-sided glass prism with a side angle of  $0.57^\circ$ . This pyramid is not directly suited for PYRAMIR on one side due to its angle, resulting in pupil overlap on the detector, and on the other hand due to its glass type, which has reduced transmission in the near-infrared range. In the laboratory neither the angle nor the glass type are problematic because the F-ratio of the beam is big enough for the pupils not to overlap and the setup works with visible light with regulatable intensity. The edge quality of this pyramid was by far the best from the sample tested.

For a more detailed description of the characterization of the different pyramids see Section 6.1.

### The CCD

The CCD used is DVC-1412 monochrome camera from CHROMAPHOR Analysen-Technik GmbH. This CCD has a high resolution of  $1392(\text{H}) \times 1040(\text{V})$  pixels having 12 bits, with a pixel size of  $6.45\mu\text{m} \times 6.45\mu\text{m}$  in square format. There is the possibility to bin the pixels in different modes up to  $8 \times 8$ . The camera has a high specified quantum efficiency of 62% at 550 nm and a readout frequency of 18 MHz. The read noise is  $8 e^-$  at 18 MHz.

## 5.1.2 Image Treatment and Software

### Pupil-finding routine

The light that passes the the glass pyramid forms an image on the CCD which consists of four illuminated circular pupils, as shown in Fig. 5.4. The quality of the pyramid edges determines

	Specifications	Lab-Pyramid
<b>Material</b>	Low-dispersion & High-transmittance in 1-2.35 $\mu$ m	BK7
<b>Shape</b>	Square or Circular	Circular
<b>Number of Sides</b>	4 (3)	4
<b>Size</b>	$\varnothing = 12$ mm	$\varnothing = 12$ mm
<b>Height</b>	$\leq 5$ mm	5 mm
<b>Angle</b>	$1.5^\circ - 1.9^\circ$	$0.57^\circ$
<b>Surface Quality</b>	$< 0.1$ $\mu$ m	$< 0.1$ $\mu$ m
<b>Tip Size and Edge Width</b>	$< 10$ $\mu$ m $\times$ $10$ $\mu$ m	$19$ $\mu$ m $\times$ $46$ $\mu$ m

Table 5.1: Required parameters for the pyramidal optical component and the parameters of the pyramid used in the laboratory setup. The edge and surface measurements were done with a profilometer.

the amount of scattered light between them.

The stray light between the pupils makes it difficult to have a completely automatized pupil search. The routine used by default to find the pupils on the CCD used 3 points per pupil given by the experimentalist per mouse-click directly on an image taken, to find the pupil positions and mask them out. This had to be done at the beginning of a measurement sequence and only had to be repeated, when the position of the optical components had been changed, changing the pupil positions on the camera.

### Signal calculation

After an image is taken with the CCD, the image can be re-binned numerically, if this has not already been done internally with the CCD. This binning is necessary because the 80 pixels per pupil diameter used exceed by far the degrees of freedom given by the DM, which has only 7 actuators per diameter and 5 per illuminated diameter (see Fig. 5.2). The signals are calculated in the usual way from the intensity distribution in the four pupils (according to Eq. 3.3):

$$S_x(x, y) = \frac{\left( I_1(x_p, y_p) + I_4(x_p, y_p) \right) - \left( I_2(x_p, y_p) + I_3(x_p, y_p) \right)}{\sum_{i=1}^4 I_i(x_p, y_p)}$$

and respectively for  $S_y$ .

This calculation is first done with a flat DM. The signals obtained, which are called the offset signals and are always non-zero, are generally subtracted from the signals of the subsequent signals. The necessity of this subtraction is made clear in the next sections. It works as a kind of flat-fielding of the sensor.

## Calibration

Before performing measurements with the sensor, a calibration sequence has to be done to get a basis set of mirror modes. For a modal reconstruction this consists of introducing into the system a sequence of deformed wavefronts, which are ideally an independent set of modes, like the Zernike or Karh unen-Loeve polynomials as example. Zernike modes generated by the DM have been used. For zonal reconstruction every actuator is poked to a certain height, being this mirror shape the independent "mode".

The signals calculated for each mode are written as a matrix  $\underbrace{I_p}_{q \times z}$ , where  $q$  is the number of pixels inside each pupil and  $z$  is the number of modes. This matrix is called the interaction matrix. Through SVD (see Appendix C for a brief description of this computational technique) this matrix is inverted, giving the reconstruction matrix of the system  $\underbrace{R_p}_{z \times q}$ . As the name indicates, this matrix will be used for the reconstruction of the wavefront after taking a measurement.

To generate a set of independent zernike modes on the DM one approach is to calculate the necessary voltage for each of the actuators according to their location on the circle and applying Eq. 5.2. Due to not-independent actuator influence functions this method produces modes with limited independence. Another more complicated technique is to first poke every actuator and take an interferometer image of the DM surface. The heights of each pixel of the interferometer image for every actuator poked are then used to build an interaction matrix  $\underbrace{I_i}_{p \times a}$ , where  $p$  is the number of pixels of the DM-image on the interferometer and  $a$  is the number of DM actuators. This matrix is inverted by SVD so that  $\underbrace{R_i}_{a \times p}$  is obtained. Multiplying this matrix with a theoretically calculated matrix  $\underbrace{Z_i}_{p \times z}$ , where the theoretical heights for the interferometer pixels for each zernike polynomial are written, gives a matrix  $\underbrace{Z_{DM}}_{a \times z}$ . In columns are written the best combinations of actuator voltages to obtain each zernike polynomial (best in a least squares sense and assuming a linear behavior of the DM).

## Measurements: Open-loop and closed-loop

To perform an open-loop measurement of an aberrated wavefront the signals obtained are multiplied with the reconstruction matrix. This gives an array with the combination of modes, which best reconstruct the disturbed wavefront in least-squares sense.

For closed-loop sequences the DM is used to introduce aberrations into the system, as well as to correct them afterwards. For the correction, the aberrations calculated from the PWS signals are transformed into mirror commands and applied to the mirror. To stabilize the loop a gain factor (generally between 0 and 1) is multiplied with the calculated modes before applying the corrections to the DM. Since the aberrations applied to the DM are static, and not chang-

ing in real-time, like the atmosphere, this running mode will be called a "static closed-loop". To check the DM flatness achieved, an interferometer image of the DM is taken after every correction.

## 5.2 Description of the simulation

The simulations describe an AO system using a PWS and were written in IDL (Interactive Data Language). They can be divided in calibration routines, simple measurement routines and simulation of closed loop regime with successive measurements and corrections.

The basic parameters, like telescope diameter, central obscuration size, working wavelength, F-ratio and detector pupil sampling are chosen in advance, as well as the guide star magnitude, sky magnitude, detector characteristics and instrument optics transmission. Optional parameters are pyramid edge width, modulation amplitude, field stop diameter, three-sided pyramid and static non-common path aberrations.

### 5.2.1 Calibration

For the calibration the initial input to the system are successive phase screens representing the different calibration modes, like zernike polynomials. In the case of static non-common path aberrations these are also introduced at this point. Here their sum is called  $W(x, y)$  and gives the phase error in radians at point  $(x, y)$  in the pupil plane. The complex generalized pupil function  $P(x, y)$  (Goodman (1996)) is obtained through:

$$P(x, y) = P(x, y) e^{iW(x, y)}, \quad (5.3)$$

where the pupil function  $P(x, y)$  is unity inside the pupil and zero outside (masking the telescope aperture and obscuration). Performing a Fourier Transformation (in the simulation a Fast Fourier Transformation (FFT) was used) the electric field  $\vec{E}$  in the focal plane is obtained. The Point Spread Function (PSF) is calculated by squaring this field, and the Strehl Ratio (SR) by normalizing the maximum of the PSF with the diffraction limited peak value. In the focal plane the pyramid is introduced. This can be simulated by a phase shifting plate  $W_{Pyr}$ , which is multiplied with the electric field:

$$E_{Pyr}^{\vec{}} = \vec{E} e^{-iW_{Pyr}}. \quad (5.4)$$

This phase shifting plate simulates the phase shifts provoked by the transversion of the glass pyramid, taking into account parameters like refraction index, angle, edge size and glass thickness. Physically this is a better model for the effect of the pyramid, than just masking out the four pyramid sides, which results in a loss of the interference effects. Just in front of the pyramid, also in the focal plane, a field stop, acting as a spatial filter can be introduced. This spatial filter is centered on the tip of the pyramid and acts as a mask on the electric field. With a second FFT the preliminary image on the detector is obtained. Generally it consists of four (or three, in the case of a three-sided pyramid) separated pupil images with some diffracted light between them. In case of a modulated sensor, the last steps are repeated for one full rotation of

the focus around the pyramid tip and the intensity on the detector is integrated. The detector model includes a rebin of the numerical pixels to the actual detector pixel size. Photon statistics is introduced by calculating the poisson noise introduced by the calibration star photons and the background photons, as well as the poisson noise by the dark current of the detector as well as the read-out noise per pixel. These last parameters vary according to the detector which is modelled. The result is then the final detector image. From the final detector image the signals are extracted according to Eq. 3.3.

This can be modified for the case of a pyramid with different number of sides or a different signal calculation scheme. The latter can be a change in the normalization-factor, dividing by the total intensity on the detector, instead of by the sum of the intensities of the four conjugated pixels.

In the next step the offset signal, i.e. the signal pattern obtained for a flat wavefront (only static aberrations are included in case they are present) is subtracted. With this signals the interaction matrix is built, writing in each column the signals corresponding to one mode. This matrix is decomposed by singular value decomposition, allowing the inversion, so that the reconstruction matrix is obtained.

### 5.2.2 Measurements

In the case of a simple measurement the input to the system consists of a phase screen with a pre-defined pattern of aberrations or one which simulates the atmosphere in certain conditions. The atmospheric phase screens are calculated through a simplified version of the TurboLenz Code (Weiss (2000)). The procedure described in the last section is followed till the signals are obtained, which are then multiplied by the reconstruction matrix, giving a vector with the calculated aberrations. These are obtained as a decomposition into the previously calibrated set of modes.

### 5.2.3 Closed-loop operation

For the simulation of an AO system working in closed loop the measurement routines remain basically the same, with some new features for the temporal evolution of the atmospheric turbulence and the correction of the measured aberrations. The measurement is performed on a sequence of phase screens, which are generated with a certain temporal step between them. Depending on the integration time of the detector, a number of pupil intensities are integrated on the detector, before the signals are calculated. The aberrations estimated by the sensor through multiplication by the reconstruction matrix are then used to calculate an estimated wavefront, which is subtracted from the next phase screens. No additional model for the correction device is introduced. At this point a system control is added, which in this simulations consists of the multiplication of a constant factor with the measured wavefront before the subtraction is performed. The measurement continues like before till the new wavefront is estimated. This is summed to the previous estimated wavefront, passes the control and is subtracted from the next phase screens. This is repeated for a predefined number of loops.

This program allows to follow the wavefront as well as the PSF and Strehl evolution during a closed loop correction limited by some of the wavefront sensor characteristics.

# Chapter 6

## Laboratory experiments and simulations

This chapter is mainly devoted to the description and the analysis of the results from the tests performed with the laboratory setup as well as to some interesting features found through the modelling of a full adaptive optics setup based on this sensor. In Section 3.4 the main questions handled in this chapter have been described.

While most of the optical components of the setup were standard, the pyramidal-shaped glass prism had to be developed especially for the requirements. I explain our specifications and describe the main problems that were encountered to meet them. The amount of light lost through edges of the pyramid and its imperfections have been analyzed. The manufacture of suited glass pyramids was a difficult task for many companies. The characterization process of the pyramids is also described and the results are shown here.

Especially the issue of the need for modulation and its effect on the performance of the sensor were one of the priorities, since there might be no need for it in some cases. It is shown that the sensor can work without modulation. Some points that require some special attention in the case of using the sensor in non-modulated regime have been studied. This is the case for static non-common path aberrations, which can limit the linear range of the sensor, and the effect of big edges and tip sizes or even a roof-shaped tip of the pyramid, which is almost unavoidable with standard polishing techniques.

The effect of a spatial filter, which is introduced in the setup just before the pyramid in the focal plane has been tested.

As an outlook to a solution to some of the problems related to the pyramid, the use of a three-sided pyramid is studied. Through numerical simulations this pyramid has given similar results to the four-sided one.

## 6.1 Pyramid characterization

One of the most critical components of this wavefront sensor is the glass pyramid, which separates the light into four beams. The edges and the tip of this pyramid have to satisfy certain specifications to avoid the loss of light, which could affect the limiting magnitude that this sensor should achieve. Especially because the sensor is supposed to work without any modulation, all the light will be focussed on the pyramid tip. The specification given for the tip and the edge-sizes was  $10\ \mu\text{m}$ . It was estimated, that for this edge size the additional light lost through the edges, for a F/100 beam, would stay below 10% for the working wavelength range. The material chosen had to be a glass with high transmission in the wavelength range of PYRAMIR (1.0-2.35  $\mu\text{m}$ ) and low dispersion to avoid a chromatic shift of the pupils on the detector. The chromatic shift has also been reduced by specifying a small pyramid height of 5 mm. To keep the readout time of the detector as short as possible the four re-imaged pupils have been positioned very close to each other. An angle of  $1.5^\circ$  between the sides and the horizontal plane was specified, avoiding an overlap of the pupils and of the stray light around them. The glass types combining these characteristics have shown to be very problematic in the polishing process, so that compromises were done in the glass type used. PYRAMIR will work with a fused silica glass pyramid, even though the dispersion is higher than first planned. This was corrected with a more complicated optics in the re-imaging combination of lenses.

Many companies from Europe and USA were contacted and some of them manufactured some pyramids on a best effort basis. These were first analyzed under a light microscope, allowing a rough estimate of the quality (see Fig. 6.1). This first check, as well as the "naked eye" check, just by looking at them, allowed to classify most of them as not usable.

Achieving the small angle required and the small edge size has been a challenging task for the polishing process. The main problem found was a big roof size. This feature is a consequence of the polishing procedure. The four sides have to be polished one after the other, and a control of the tip is only done afterwards. It is not possible with this technique to have all the four sides joining at the same point. Generally a roof is formed due to an over-polishing of one of the sides (see Fig. 6.1).

One different problem encountered were rounded faces. A pyramid, where the faces have a certain curvature, provokes a movement of the pupils when a tilt is applied. A shift of the pupil position during measurements would need a constant repetition of the pupil finding procedure, which is not desirable.

There were also problems with broken pieces at the tip and deeply scratched surfaces. Some materials with low dispersion and high near-infrared transmission were too soft, breaking easily. The material choice was at the end fused silica, a glass with high transmission in the near-infrared bands. The dispersion is higher than for other glass types but could be accounted for in the optical design making it only slightly more complicated. The silica pyramids for PYRAMIR have been observed with a light microscope, allowing as a rough estimate, that the tip quality is at least comparable to the BK7 pyramid, that was used in the laboratory setup for testing purposes. The silica as well as the BK7 pyramids have been manufactured by the same company.

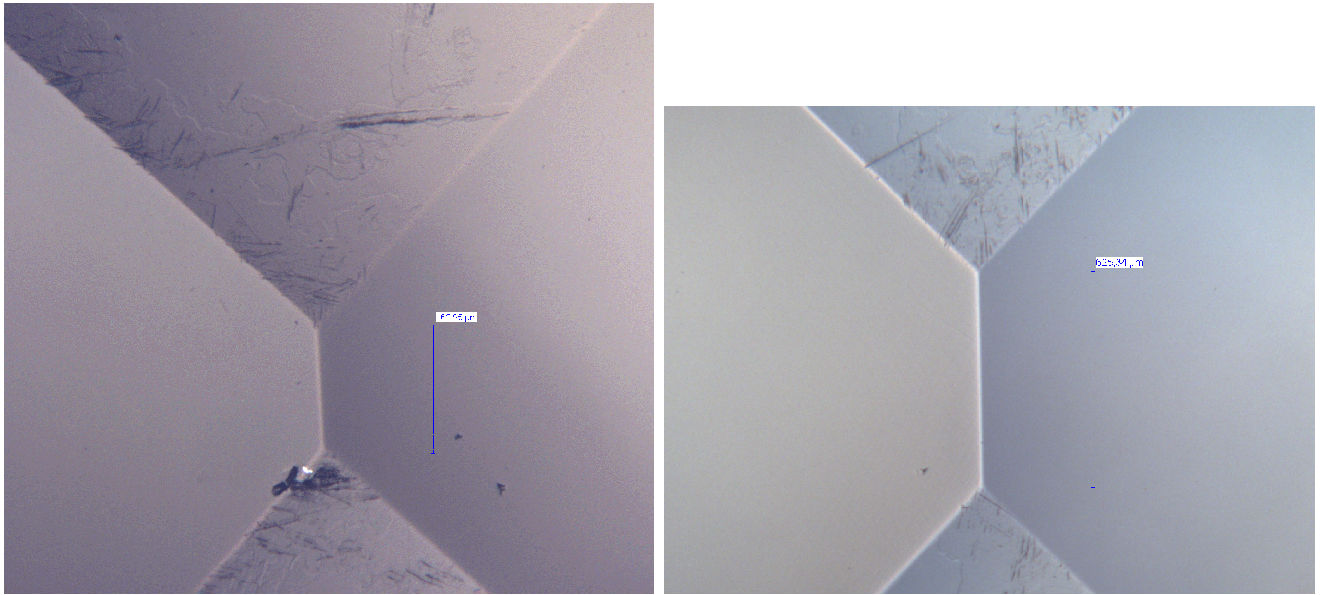


Figure 6.1: These images were taken with a light microscope. They show two of the first four-sided pyramids, which were polished for this project. The roof sizes were estimated as  $163 \mu m$  for the left pyramid and  $625 \mu m$  for the right pyramid. It can be seen that the first two sides that have been polished are scratched due to the polishing of the other two sides. These were polished over the limit, producing the typical roof.

All pyramids have been characterized with a profilometer (Tencor P-10). With this instrument the surface of the pyramid was scanned in two perpendicular directions, along the roof and perpendicular to it. This allowed a plot of the surface height (see Fig. 6.2) and an estimation of the size of the roof at the tip, as well as the determination of the angle of the pyramid sides to the horizontal (with the assumption that the angle has the same value on the two facing sides). The tip was defined as the region, where the surface differs more than  $0.1 \mu m$  from the tangent plane on both sides of the scan cut on each of the four pyramid sides. The principle is exemplified in Fig. 6.2 and the results of the measurements are tabulated in Tab. 6.1. For the laboratory pyramid two independent measurements with two different profilometers are given. Measurement(b), with the estimated bigger tip size, is most probably correct because measurement(a) had some problems due to a small scan region in one of the directions. In any case, as next step, the BK7 and the silica pyramid will be characterized by the same method again.

Also two three-sided pyramids have been polished for this project. As stated in Section 3.4.7 there is no problem with a roof creation in this case. These pyramids have also been characterized with the profilometer technique. A three-dimensional plot is shown in Fig. 6.4 and the parameters measured are given in Tab. 6.1. The tests in the laboratory to determine their performance in the PWS are scheduled for very soon.

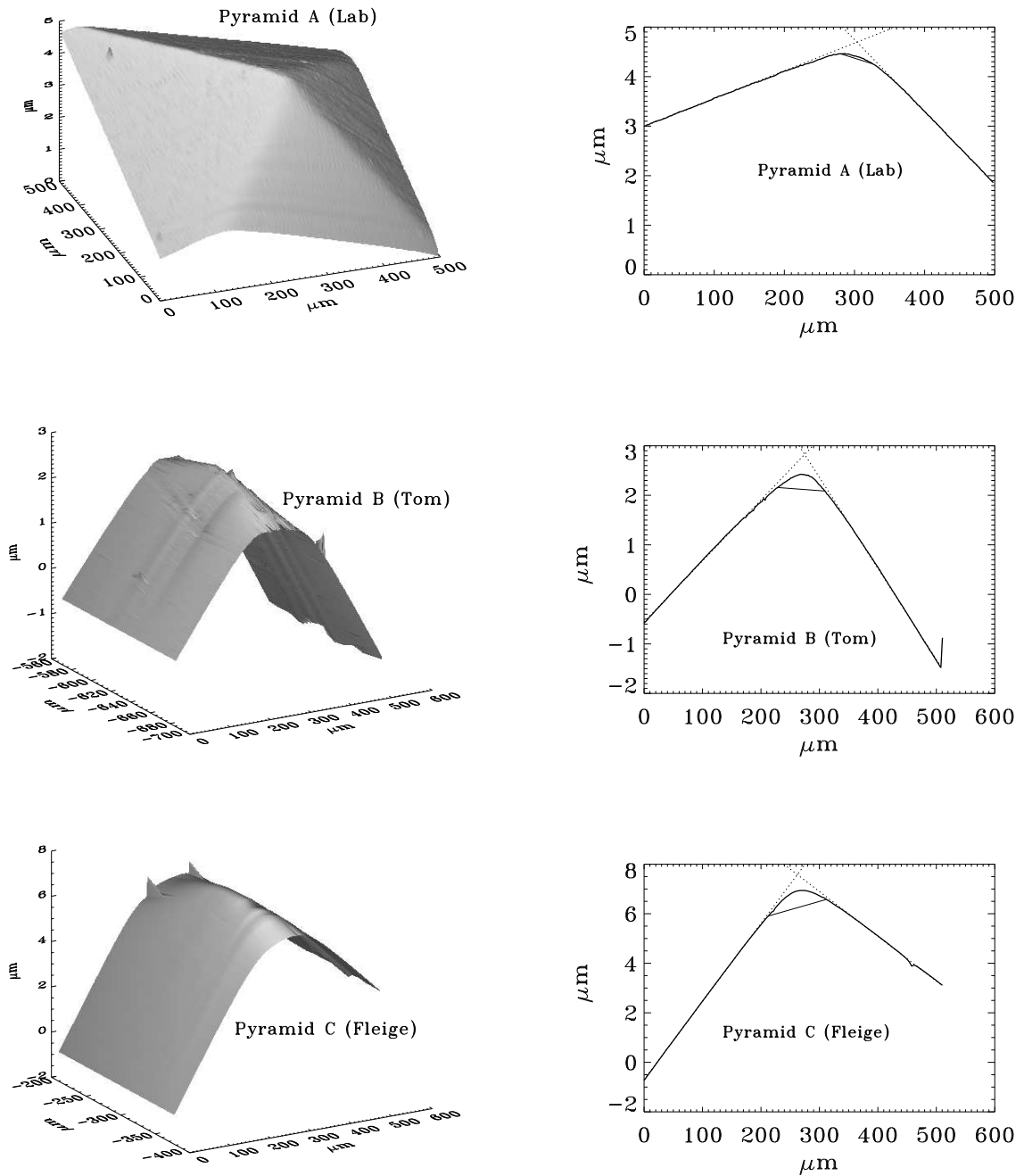


Figure 6.2: These measurements were done with the profilometer. On the left is shown the surface plot of the pyramid, on the right one of the line scans is plotted. The dotted lines show the fitted tangents for angle estimation and for tip size estimation. All axes are in  $\mu\text{m}$ . For explanation and results see text and Tab.6.1. The top images correspond to the laboratory pyramid. These were done with a profilometer that allowed to make an automatic 3-dimensional plot since it performed an automatic 2-dim scan. The second line of images are from the pyramid polished by Tom Herbst. For these and the following a profilometer with only 1 direction of automatic scan was used. To obtain a 3-dimensional image manual shifts were made, reducing the precision in one direction. Scans along the roof and perpendicular to it were made. Here the perpendicular scans are shown. The third line corresponds to the Fleige Pyramid.

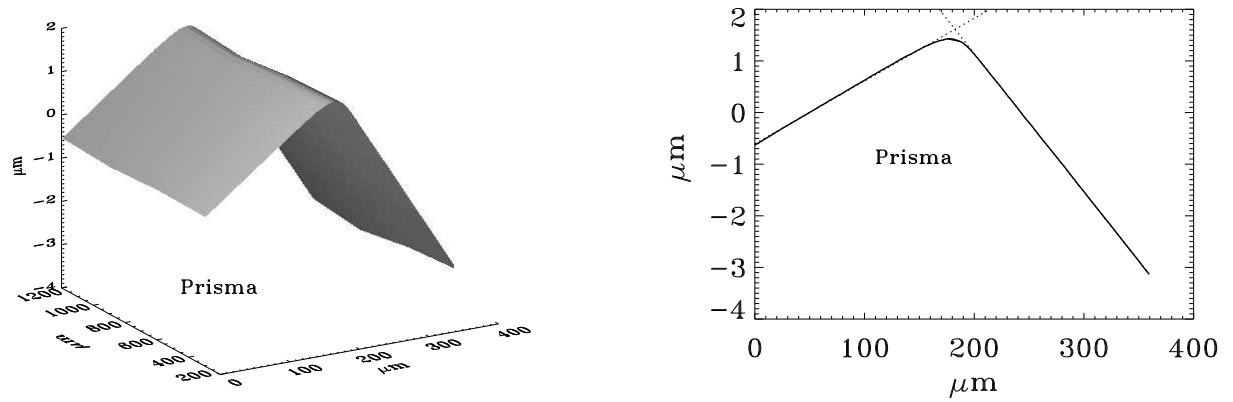


Figure 6.3: These images correspond to the two-sided prisma manufactured as a first test, where the edge quality as well as the surface quality is very good.

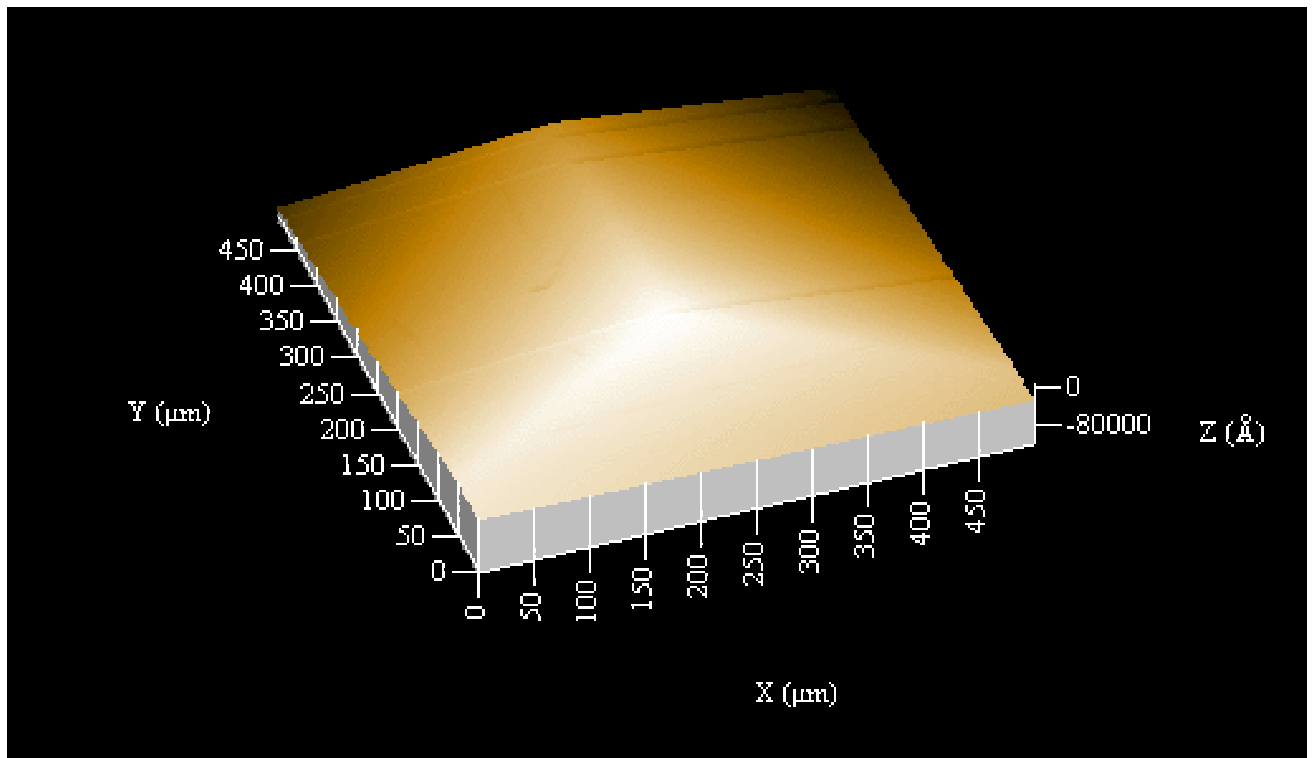


Figure 6.4: This is a 3-dimensional plot of the three-sided pyramid, given by the profilometer. The x-axis and y-axis are given in  $\mu\text{m}$  and the z-axis in Angström.

	<b>A-Lab</b>	<b>B</b>	<b>C</b>	<b>D-Prisma</b>	<b>E</b>	<b>F-3sided</b>
<b>Company</b>	WZW Optic AG (Switzerland)	Tom/Precision Optics (USA)	Fleige Optik	TNO Delft (Netherlands)	Applied Optics (USA)	Applied Optics (USA)
<b>Material</b>	BK7	S-FPL53 Ohara	N-PK52	BK7	S-FPL53 Ohara	S-FPL53 Ohara
<b>Shape</b>	Circular	Square	Square	Square	Square	Square
<b>Size</b>	$\varnothing = 12\text{ mm}$	$8.0\text{ mm} \times 8.0\text{ mm}$	$20\text{ mm} \times 20\text{ mm}$	-	$20\text{ mm} \times 20\text{ mm}$	$20\text{ mm} \times 20\text{ mm}$
<b>Height</b>	$5\text{ mm}$	$5\text{ mm}$	$3.6\text{ mm}$	-	$5\text{ mm}$	$5\text{ mm}$
<b>Angle</b>	$0.57^\circ$	$0.9^\circ$	$1.4^\circ$	$1.12^\circ$	$1.3^\circ$	
<b>Surface Quality</b>	$< 0.1\ \mu\text{m}$	rounded faces	o.k.	$< 0.1\ \mu\text{m}$	irregular	not evaluated
<b>Tip Size (a)</b>	$3.5\ \mu\text{m} \times 19\ \mu\text{m}$	$80\ \mu\text{m} \times 95\ \mu\text{m}$	$100\ \mu\text{m} \times 125\ \mu\text{m}$	$12\ \mu\text{m}$	$76\ \mu\text{m} \times 133\ \mu\text{m}$	-
<b>Tip Size (b)</b>	$18.5\ \mu\text{m} \times 46\ \mu\text{m}$					

Table 6.1: Characterization of some of the pyramids tested. The first one, pyramid A, was used in the laboratory setup and was manufactured by the same company, which delivered us the silica pyramids for PYRAMIR. We assume that the measurement(b), with the estimated bigger tip size, is correct. Measurement(a) had some problems due to a small scan region in one of the directions. There are also given the parameters of some of the other pyramids. The pyramid B had the drawback of rounded faces. Pyramid C had a very big roof size. D refers to a two-sided prisma tested, which had very good quality. Pyramid E had a very irregular surface quality because of the deep scratches near to the edge. This did not allow to reconstruct a three-dimensional plot, as for the other ones (see Fig. 6.2 and 6.3). An estimation of the angle and of the tip size had to be made out of the most reliable measurements only. The estimation of the angle for this pyramid differed by  $0.3^\circ$  in the measurements along and perpendicular to the roof. The last column refers to the three-sided pyramid delivered (see Fig. 6.4 for a three dimensional view). The laboratory tests of its usability for the PWS are scheduled for soon.

## 6.2 Light loss

This effect was studied through numerical simulations and in the laboratory, during a collaboration with Simone Esposito at the Astronomical Observatory of Arcetri in Florence, Italy.

### 6.2.1 Numerical estimation

The amount of light lost through the pyramid in the not modulated case could be estimated numerically, using the simulation described in Section 5.2. The parameters used are a 3.5 m telescope, with a central obscuration ratio  $\epsilon$  of 0.39 working at  $2.2 \mu\text{m}$  with an F/100 beam. The full width at half maximum of the diffraction limited PSF is then  $220 \mu\text{m}$ . This reproduces the optical conditions of the PYRAMIR instrument working at the Calar Alto 3.5 m telescope. The plot in Fig. 6.5 shows that 10% of the overall light which enters the sensor is lost at the edge if it has a size of  $50\text{-}60 \mu\text{m}$ . It also shows that even if the pyramid edges are perfect and in the diffraction limited case, 50% of the initial light is lost outside the pupils. This means that at  $40 \mu\text{m}$  10% of the light that can land inside the pupils is lost.

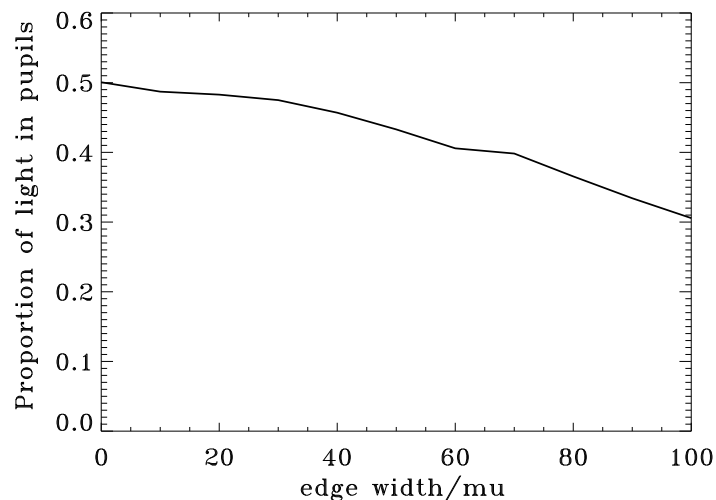


Figure 6.5: This plot shows the proportion of light, which can still be detected inside the four pupils on the detector after being refracted by the pyramid. This is plotted as function of different edge sizes. Normalization constant is the amount of light in the system before refraction by the pyramid. The simulation was done for a 3.5 m telescope, working with a  $2.2 \mu\text{m}$  wavelength and a F/100 beam. The total of light lost from inside the pupils increases with edge size.

In presence of optical aberrations the focus on the pyramid will not be diffraction limited and therefore more extended. This will spread more light over the sides of the pyramid, resulting in a smaller effect of the edges finite size. In Fig. 6.6 this is shown for a range of aberration amplitudes of defocus and astigmatism. The simulated edge size is 0. It can be seen that in case the aberrations are of the order of  $0.5 \mu\text{m}$  RMS, the amount of light lost decreases to less than

20%.

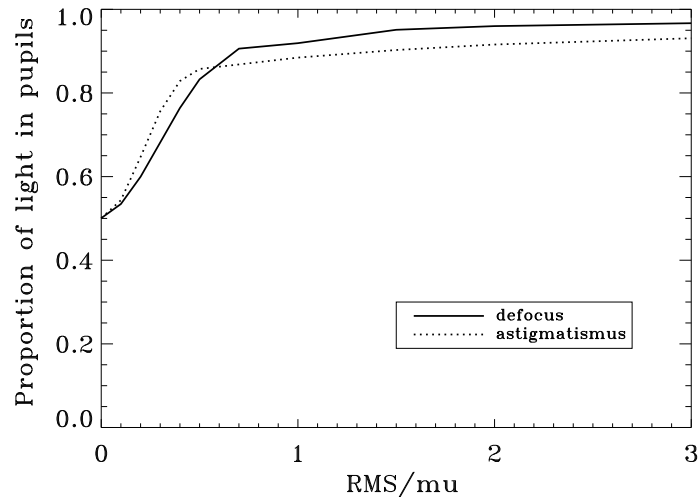


Figure 6.6: Here are shown simulation results for the proportion of light, which can be detected inside the four pupils on the detector, in relation to the amount of light present before refraction by the pyramid, as a function of the RMS of the wavefront. Aberrations increase the PSF size and the effect of the edges on the light lost is reduced. With an aberration of  $0.5 \mu\text{m}$  RMS more than 80% of the intensity is inside the pupils. The simulation parameters were a 3.5 m telescope, working with a  $2.2 \mu\text{m}$  wavelength and a F/100 beam.

## 6.2.2 Laboratory experiments

The following experiments were done with the laboratory setup in Arcetri, which is described with great detail in (Feeny (2001)). The setup is similar to the one described before, so that I will not refer to details here. The main difference is the F-ratio, which is 86 in this setup. The interferometer which provided the light source is a Fizeau type one, with a wavelength of  $0.63 \mu\text{m}$ . After the pyramid, a photographic objective with 50 mm focal length creates a four-pupil image on the 8-bit CCD (CCD1). Each of the 4 pupils has 80 pixels diameter and the distance between their centers is ca. 300 pixels.

The measurements performed had the main goal of quantifying the amount of light lost due to the presence of a pyramid, and the amount of light lost, when the light was spread in four pupils, disentangling both effects.

One problem was the laser intensity instability in time. To get a normalization factor, that allowed to account for this effect, the light was split before being focussed on the pyramid. This was done with a beamsplitter, which reflects ca. 10% of the light to the pyramid, the transmitted

light being focussed on another CCD (CCD2).

The effect of introducing the pyramid was tested by comparing the intensities on the complete CCD1 without pyramid and with pyramid, the latter in a position in which the light is focussed on only one of the sides, producing only one pupil. There was no relevant light loss, just by introducing the pyramid, if the light was not diffracted by the edges.

Sequences of measurements of each of the four pupils independently were made, having the focus modulating only on one side of the pyramid, as well as with the beam focussed on the tip of the pyramid, modulating around it, having four pupils on the CCD. The measurements were normalized by the laser intensity, taken with CCD2 and the integration time, which was longer for the four-pupil images. The main results are shown in Fig. 6.7. The light completely lost from the CCD chip and the light lost between the pupils just by introducing the pyramid were calculated with:

$$I_{\text{out of CCD}} = 1 - \frac{I_t^{4p}}{I_t^{1p}} \quad (6.1)$$

$$I_{\text{out of pupils}} = 1 - \frac{I_i^{4p}}{I_t^{1p}} \quad (6.2)$$

$$I_{\text{between pupils}} = I_{\text{out of pupils}} - I_{\text{out of CCD}}. \quad (6.3)$$

$I_t$  means the intensity on the complete CCD chip,  $I_i$  the intensity inside the four pupils, the subscripts give the number of pupils of the image (1 or 4). This measurements were done for different modulation amplitudes ranging from 0 V to 7 V. For this setup the correspondence of the control voltage  $V$  to modulation amplitude size  $\alpha$  in  $\lambda/D$  units is (Feeney (2001)):

$$\alpha[\lambda/D] = 3.2V, \quad (6.4)$$

corresponding to 0 – 22.4  $\lambda/D$  diameter.

The greatest amount of light is lost by diffraction at the edges just by introducing the pyramid. With increasing modulation amplitude this amount of light lost completely from the CCD decreases from more than 60% to around 20%, especially steeply between 0 and 1 V. This is probably the region of the roof. The light between the pupils also decreases but more continuously over the hole range.

## 6.3 Laboratory setup characterization

Here the tests performed on the laboratory setup for optimizing the calibration and measurement techniques are detailed. The description of the setup is given in Chapter 5.

### 6.3.1 The focus on the pyramid

The PWS in the laboratory works with an F-ratio of around 170, what implies that the beam is very narrow in the region of the focus. The position of the focus along the optical axis could

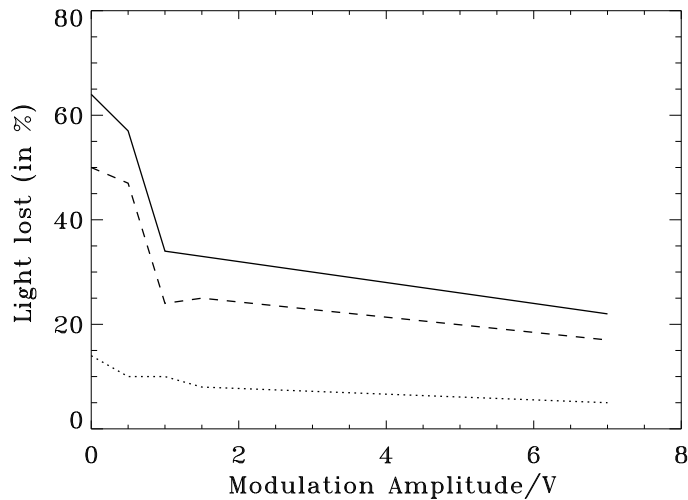


Figure 6.7: Here is shown the light loss in percent when the light beam is focussed on or modulated around the tip of the pyramid with different modulation amplitudes. The continuous line gives the light lost from inside the four pupils, the dotted line represents the light lost between the four pupils, which is still detected on the CCD and the dashed line plots the light loss completely from the detector chip.

not be found through the optical design previously made for the setup, because the tolerances of the lenses and the uncertainties in their positioning already provoked a shift of the focus of the order of some millimeters (or even centimeters). The position of the focus, as well as its size and shape were determined by placing the CCD at the pyramids position. Cuts through the image of the focus were fitted to gaussian curves, as seen in Fig. 6.8. The flat region in the center of the focus is due to CCD saturation at the value of 4095. A series of measurements showed that the full width at half maximum is  $(104 \pm 5) \mu\text{m}$ , being the focus slightly larger in horizontal than in vertical direction (see Tab. 6.2).

	<b>FWHM</b>
<b>Horizontal</b>	$(108 \pm 2) \mu\text{m}$
<b>Vertical</b>	$(99 \pm 2) \mu\text{m}$
<b>Total</b>	$(104 \pm 5) \mu\text{m}$

Table 6.2: Full width at half maximum of the focus of the PWS.

When the full PWS system is mounted, a defocus on the pyramid can generally be seen in the illumination pattern of the four pupils, but very small shifts along the optical axis stay invisible at first view. Since the PWS is very sensitive, it will nevertheless wrongly try to correct it. To check if the pyramid was slightly defocussed, the focus point was searched with a small pinhole,

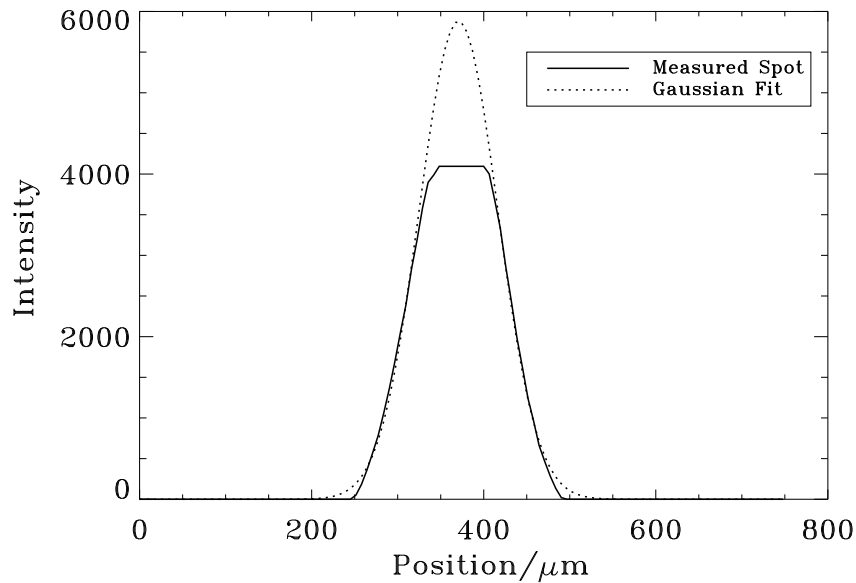


Figure 6.8: A horizontal cut through an image of the focus of the PWS. The central part of the focus is saturated. A gaussian curve was fitted to the measured intensity pattern, showing a FWHM of approximately  $100\ \mu\text{m}$

which was shifted along the optical axis. The focus position is found when a maximum of light was reaching the CCD .

### 6.3.2 Offset subtraction

In simulations it can be seen that in any case it is better to subtract the offset signals (which are calculated from the CCD pupils when no aberrations are applied) and especially in case static aberrations are present in the system it is very important. In the laboratory system this was tested by subtracting the offset signals obtained through a measurement with the mirror in its bias position. The results obtained in the calibration measurements confirm this, as can be seen in Fig.6.9. This calibration sequences were done for 9 modes and with a DM bias of 64, which leads to an intrinsic astigmatism and to a quite high defocus, where the latter is optically corrected in the PWS. The interferometer is also calibrated to this defocus, so that it is always subtracted in the measurements. The calibrations were repeated for different amplitudes of the modes applied. The amplitude of the modes is given in "au" since no RMS can be defined for one amplitude (see Section 6.3.4). We see in the two figures that the condition number<sup>1</sup> is generally lower for the calibrations with offset subtraction.

---

<sup>1</sup>See Appendix C for the definition of condition number

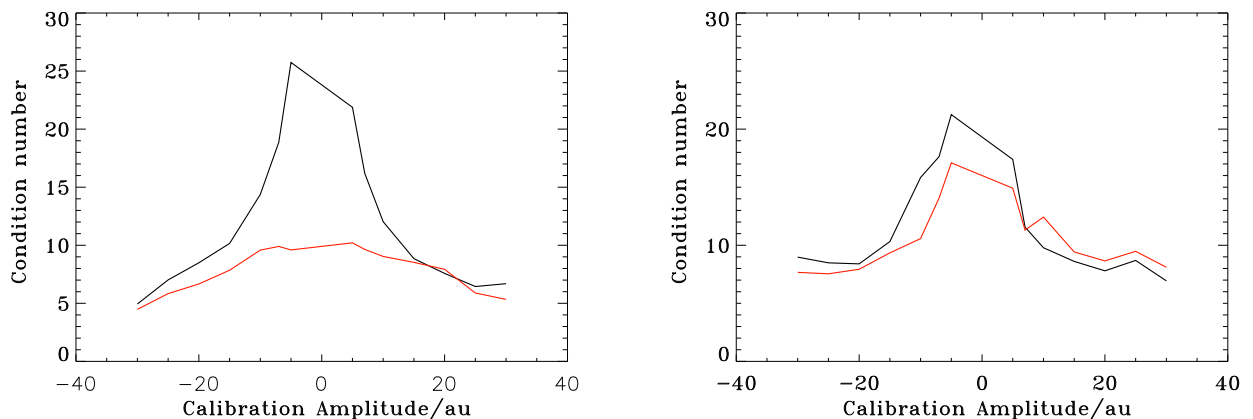


Figure 6.9: Both figures represent the condition number of our laboratory system for different calibration amplitudes reaching from -30 to 30 au. In both cases the number of modes calibrated was 9. On the left side the normalization radius for the zernike modes was 6 mm (complete mirrored surface), while on the right side the radius was 4.5 mm. The black and the red lines correspond to the calibration without and with offset signal subtraction respectively.

### 6.3.3 Normalization diameter

The complete mirrored surface of the DM has a radius of 6 mm, while the illuminated circle only has a radius of 4.5 mm. It was therefore tested which was the best normalization radius for the zernike modes. Calibrations were made with the zernike polynomials normalized on the complete mirror surface as well as only on the central 9 mm. In this case the actuators lying outside this radius were poked to the height given by the zernike polynomial outside the normalization radius. In Fig.6.9 we see that for a bigger mirror, in case the offset is subtracted, the lowest condition numbers are achieved, hence the zernike modes were always normalized on the complete mirror.

### 6.3.4 Quality of the modes

The modes to calibrate an AO system are desired to be independent and to have a linear behavior. The quality of the zernike modes used for calibration which are produced by the DM was analyzed. This was done with the interferometer by monitoring the mirror surface when different modes were applied to it.

The first 9 zernike modes were applied sequentially to the DM and the surface imaged with the interferometer. In Fig.6.10 the RMS of this surfaces is plotted as function of the applied amplitude and of the zernike mode. It can be seen that the RMS is not constant for all the modes at the same amplitude. Modes of lower order generate higher DM distortion, but the RMS is nearly linearly proportional to the amplitude, having a different proportionality constant for every mode. The amplitude will be measured in arbitrary units "au" in the following, since the correspondence with the RMS is not constant, but depends on the mode.

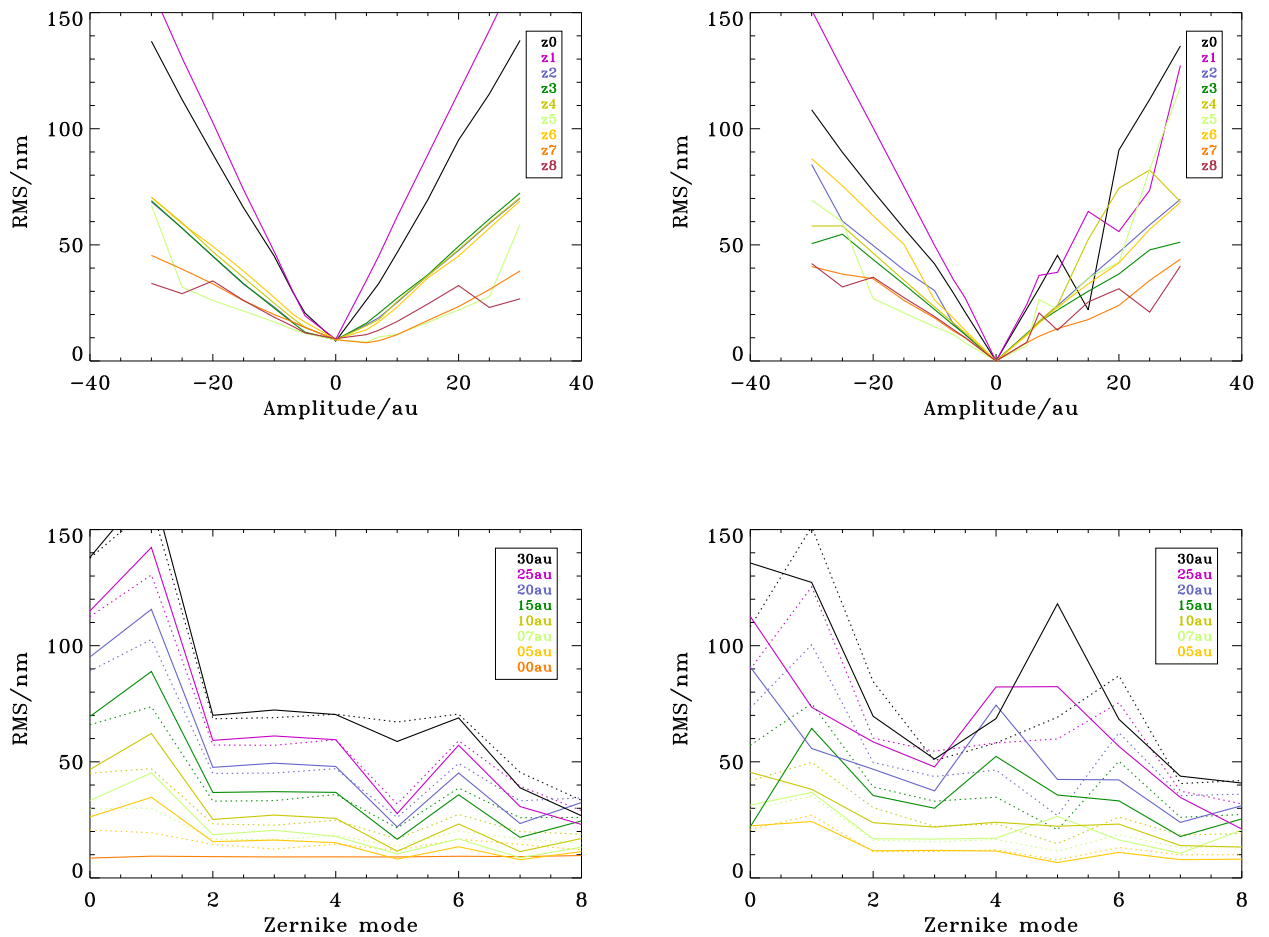


Figure 6.10: The figures on the left side correspond to a mirror biased to a constant value of 64. On the right side the mirror was biased to the actuator values obtained through a flattening routine. In the top images the RMS of the mirror surface is plotted as a function of the amplitude of the mode applied (in au). The bottom images show the RMS as function of the zernike mode ( $z_0$ - $z_8$ ). The dotted lines correspond to negative calibration amplitudes.

One can see that the lower order modes have a higher RMS for the same calibration amplitude, which generally decreases when the order increases. In the case of the flattened mirror the positive amplitudes do not have a decrease in stages of the RMS with the amplitude. The mirror biased to 64 shows a more linear behavior.

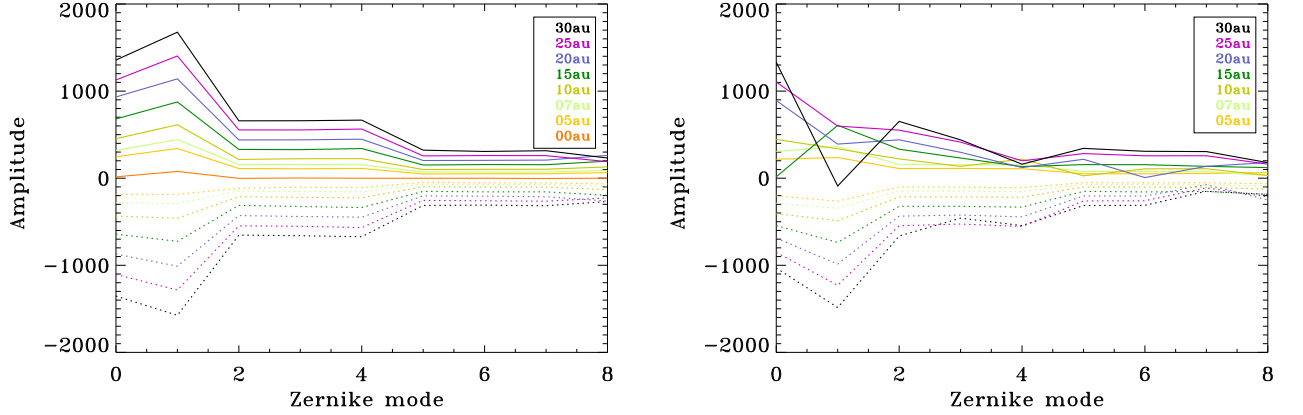


Figure 6.11: For the first 9 mirror modes the corresponding surface plots measured with the interferometer were decomposed into zernike modes. For each of the mirror modes the corresponding amplitude of zernike mode is plotted. This is shown on the left for a mirror biased to a constant value of 64 and on the right for a flattened mirror. Although these mirror modes were calculated according to zernike modes, due to its limited spatial sampling and non-linearity, the theoretical modes are not exactly reproduced. The amount of zernike polynom in a mirror mode decreases in two main steps, when there is a change in polynom order (first with defocus and then with the coma terms). Despite this steps, the amount of "correct" zernike mode in the corresponding mirror mode increases linearly with the applied amplitude, with exception of the positive amplitudes applied over a flattened surface, as before.

In the case of the positive amplitudes with the DM biased to the flattened surface, there is no linear behavior like described in the last paragraph. Very likely this is due to the fact that the flattened mirror produces a tilt, which may affect the dynamic range and the quadratic behavior with voltage.

The calibration amplitude should be inside the linear range of the sensor on one side, but on the other side the condition number should also be kept low so that a tradeoff has to be made. The amplitudes 7 au and 10 au were chosen as the most suitable, since their RMS is mostly lower than 60 nm, which corresponds to  $0.1\lambda$ . This can be seen in Fig. 6.10 where it has to be taken into account that the interferometer measures the surface RMS, but for our PWS the distortion has to be doubled due to the reflection.

Additionally the quality of the modes generated by the DM was tested. The mirror surface height plots obtained with the interferometer were decomposed in theoretical zernike modes by the following procedure: On a circular mask of the same size as the interferometer images, with  $q$  pixels, theoretical surface plots of the first  $n_Z$  zernike modes were generated. These were written as columns of a matrix  $Z$ :

$$\underbrace{S_I}_q = \underbrace{Z}_{q \times n_Z} \underbrace{C_Z}_{n_Z}. \quad (6.5)$$

$S_I$  is a vector giving the theoretical heights of all the pixels of the interferometer image.  $C_z$  is a vector with each element being the amplitude of the zernike polynom.  $Z$  can be decomposed through SVD (see Appendix C), and the pseudo-inverse of  $Z$ , called here  $Z^+$ , can be calculated. A least-square minimum length solution to the decomposition of a surface plot into zernike modes can be estimated through

$$\underbrace{C_Z}_{n_Z} = \underbrace{Z^+}_{n_Z \times q} \underbrace{S_I}_q. \quad (6.6)$$

An analysis of the zernike modes produced by the DM can be seen in Fig.6.11. It allowed to establish the main modes which have cross-talk, i.e. which mirror modes are contaminated by more than one zernike. The strongest effect of mode-mixing appears in the coma modes with the corresponding tip and tilt terms. The figures show the calculated coefficient for each zernike mode for different amplitudes. The coefficients have a linear behavior with the amplitude applied, although they decrease with higher orders. This means that the higher the order of the mode which is applied to the DM, the less of this mode is really present in the decomposition of the surface plot but this amount increases linearly with the amplitude. The exception is again the behavior of the flattened mirror for positive amplitudes where the linearity is disturbed. This was expected from the previous results of the RMS.

### 6.3.5 Pupil sampling

To have the freedom of choosing the size of the sampling of the pupils on the CCD the pupil diameter was set 80 pixels on the CCD, and through different binning the effective sampling could be set. Most measurements were done with 8 pixels or 5 pixels, the latter being the sampling better adapted to the DM actuator sampling, which has also 5 actuators per diameter of the illuminated area (see Fig.5.2).

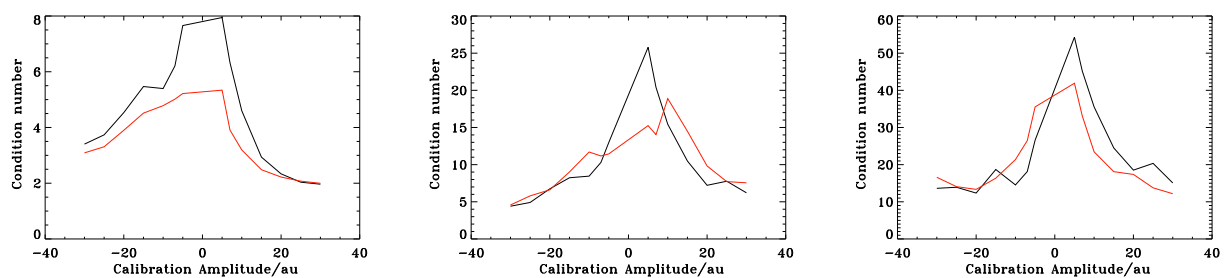


Figure 6.12: These three plots represent the condition numbers for a system calibrated with 5, 9 and 14 modes from left to right, as a function of the calibration amplitude in au. The black line shows the results for 8 pixels and the red line for 5 pixels per pupil diameter on the CCD.

The system was calibrated for different number of modes having a diameter size of 5 pixels and 8 pixels. The analysis of the condition number for this calibrations is shown in Fig.6.12. For a relatively small number of 5 modes the lower number of pixels shows a better condition number

Array Size	1024 px
Entrance Pupil Size	80 px
Wavelength	1.0 $\mu\text{m}$
Calibration Amplitude	0.06-0.6 rad
PSF size (FWHM)	12.8 px
Pupil Size on CCD	8 px
Modulation Amplitude	0-2 $\lambda/D$

Table 6.3: The parameters for the simulation comparing the calibration results for different modulation amplitudes.

at all calibration amplitudes. But in both cases the condition number stays less than 10, what is very good. A significant difference appears only for small calibration amplitudes (0-5 au), where the sensor with 5 pixels per diameter performs better. Especially for a low order of calibrated modes, the system with 5 pixels shows lower condition numbers.

## 6.4 The modulation

In this section the effects of modulation on the sensor measurements were studied through numerical simulations as well as through laboratory verification.

### 6.4.1 Simulation results

The effects of modulation were studied through a numerical simulation, which models a complete adaptive optics system with a pyramid wavefront sensor. A description of this simulation is given in Section 5.2. To study the general behavior of a PWS system with different modulation amplitudes various steps of an adaptive optics system were analyzed.

The calibration of the wavefront sensor was done by calculating the response, in terms of signals, of the wavefronts corresponding to the first zernike modes (the calibrations were done with a number of zernike modes from 2-35). This allows to construct the interaction matrix and to obtain the reconstruction matrix through singular value decomposition (see Appendix C for an explanation of this technique and the applications of it in this work). The singular values obtained allow an analysis of the system in terms of sensitivity. The more sensitive a system is, the higher the singular values are. On the other hand, if a singular value is very small, there is a combination of modes which is very sensitive to noise and which will harm the system. Looking at the condition number of the system gives a measure of the noise propagation through the reconstruction process. The condition number is proportional to the sensitivity of the system to slight perturbations in the interaction matrix or the measurements.

The main parameters used are given in Tab. 6.3. Complete calibration sequences were performed for increasing number of modes, different calibration amplitudes and different modulation am-

plitudes ( $0-2\lambda/D$ ). In this simulation no photon statistics is considered and no spatial filter is located in front of the pyramid. The edge size of the pyramid is supposed to be smaller than  $13\mu\text{m}$ , the sampling size of the focal plane.

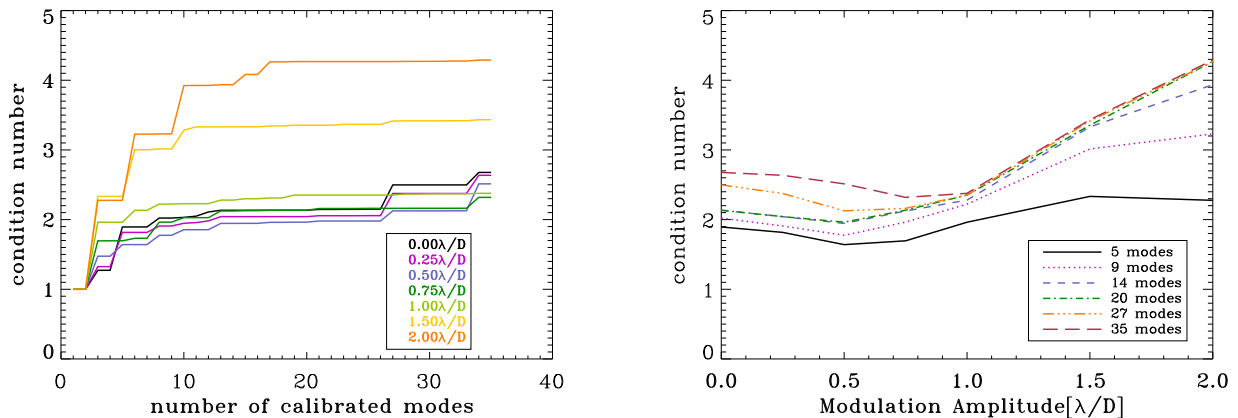


Figure 6.13: In the left figure the condition numbers of sequences of calibrations are plotted as a function of the number of calibrated modes. Seven different modulation amplitudes, ranging from  $0.25-2.0\lambda/D$  radius, were tested. The same set of data is plotted on the right side, but as a function of the modulation amplitude. Here the smallest calibration amplitude of  $0.06$  rad was used.

As shown in Fig.6.13 the ideal modulation amplitude in terms of condition number for a small calibration amplitude of  $0.06$  rad lays around  $0.5\lambda/D$ .  $\lambda/D$  is the angular full width at half maximum (FWHM) of the diffraction limited PSF.  $0.5\lambda/D$  is the smallest modulation amplitude in which the complete diffraction-limited PSF passes through every side of the pyramid. In the case of small calibration amplitudes, like the one used, the PSF size is almost diffraction limited size.

For bigger calibration amplitudes the PSF size increases and the modulation amplitude, correspondent to half FWHM is bigger. This explains the result that was obtained in simulations that the optimum modulation amplitude increases with calibration amplitude.

### Closed-loop simulations

To simulate the closed-loop regime a temporal sequence of measurements and corrections had to be performed, taking into account the temporal evolution of the atmosphere. With a sequence of phasescreens, simulating the phase-shifting properties of the atmosphere at a rate of 1 screen per ms and over an array of  $1024\times 1024$  pixels, the influence of the atmosphere on a given (flat) wavefront was determined. These phasescreens have been generated with the TurbuLenZ-code (Weiss (2000)), an atmospheric turbulence simulator.

The integration time of the detector was taken into account integrating the intensity on the

detector images for 10 successive phasescreens (this represents an integration time of 10 ms). The signals were calculated from the integrated image and the wavefront reconstructed. This estimate of the wavefront was subtracted from the following 10 screens. A new intensity integration and reconstruction led to a new estimate of the residual wavefront.

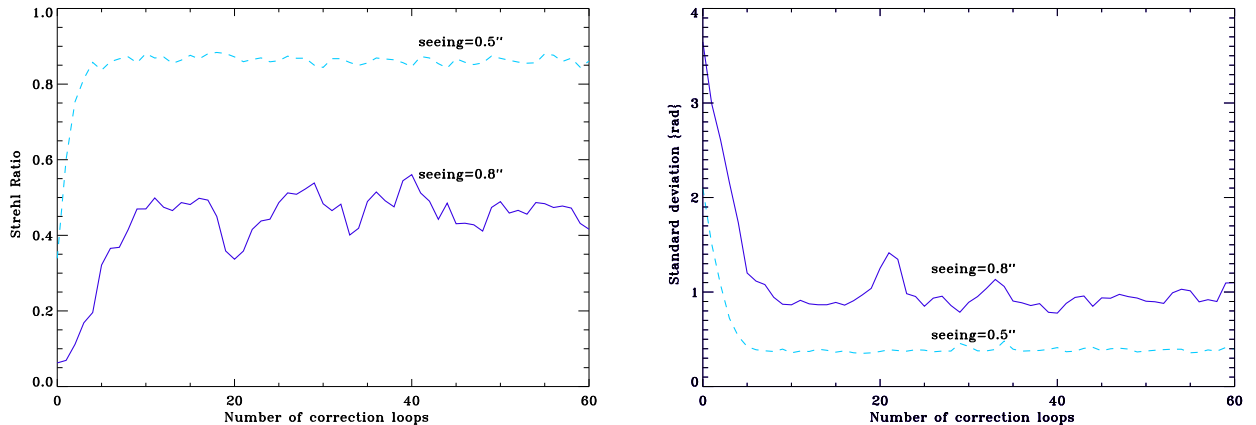


Figure 6.14: Evolution of the Strehl Ratio and the standard deviation for different atmospheric conditions in closed loop compensation.

This was done for 0.6 seconds, corresponding to 60 correction cycles, for seeing of 0.5'' and 0.8''. The parameters of the phasescreens are a  $\tau_0^2$  of 100 ms, a telescope diameter of 5.7 m and a wavelength of 2.2  $\mu\text{m}$ . The results in terms of residual standard deviation and Strehl ratio (SR) are shown in Fig. 6.14. The plots include the bootstrapping phase, showing that it is possible to close the loop without modulation on sky. At least for the time period simulated, the correction was stable for both seeing conditions.

Preliminary results from independent simulations, made for the first-light AO system of LBT (Carbillet et al. (2003)) with a code (the software package CAOS) that permits the simulation of a dynamical modulation, have been used for comparing different cases with and without modulation (see Costa et al. (2003b)). In Fig. 6.15 on the left side there are two cases plotted, one with a good SNR (top) and the other one with a poor (bottom) SNR. The interaction matrices have been recorded with  $\pm 7 \lambda/D$  for the top and  $\pm 8 \lambda/D$  for the bottom curve. During the closed-loop different modulations were used. The curves show that, when using an interaction matrix recorded with a given (relatively high) modulation, the differences between modulating or not during correction is small.

In the right plot, which is to be compared to the upper case of the left plot, the same modulation that was used during calibration,  $\pm 1 \lambda/D$ , was used also for the correction, only changing the gain. The result is that the performances could reach again the performance of the top curve in the left plot. All the curves should be compared to the 3dot-line, which represents correction at

<sup>2</sup> $\tau_0$  is a time constant related to the Greenwood frequency  $f_G$  by  $\tau_0 = 0.134/f_G$ .

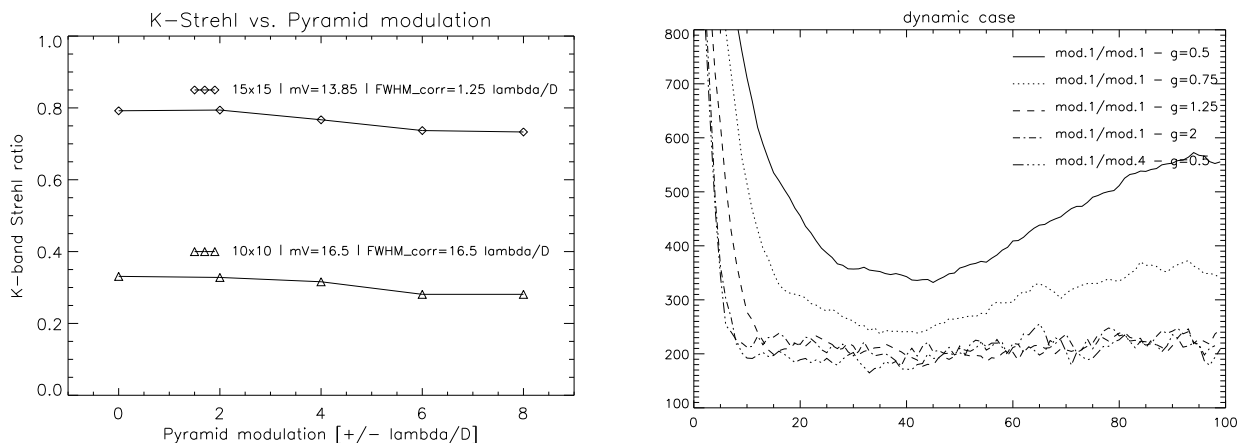


Figure 6.15: left: Strehl ratios achieved in K-band for closed-loop compensation with different modulation amplitudes. In the top curve we have a good SNR ( $mV=13.85$ ), while in the bottom one we have a poor SNR ( $mV=16.5$ ).

right: Wavefront deviation (in arbitrary units) as a function of the increasing loop step number for different combinations of calibration and correction modulations.

modulation  $\pm 1\lambda/D$  and interaction matrix taken at  $\pm 4\lambda/D$ , with a gain of 0.5. These parameters allow the best average SR in this case ( $SR=0.767$ ). Then the same simulation has been run with a modulation of  $\pm 1\lambda/D$  during calibration. With a gain of 0.5 the performance is bad, because the temporal error is high. But for a gain of 1.25 the SR reaches 0.750, very near to the first case. This curve essentially shows that by optimizing the gain of the loop, we retrieve, even with a matrix recorded at low modulation, the same result as by recording at high modulation and correcting at low modulation.

## 6.4.2 Laboratory verification

The laboratory setup has the possibility to work without and with modulation. This modulation was performed by the tip-tilt mirror, which was programmed to perform a circular movement of the beam focus around the pyramid tip. The amplitude of this movement can be varied according to Fig. 5.5. In Fig. 6.16 images of the four pupils on the CCD in modulated and not modulated regime are shown. When the beam is modulated the immediate main differences are the amount of light outside the pupils, which is lower in this case, and the smoothness in the illumination inside the pupils. The pupil illumination in the not modulated case has stronger intensity variations, which can extend over the complete dynamic range of the CCD.

A first analysis of the systems performance was done through the analysis of the condition numbers analogous to Section 6.4.1. The system was calibrated with different calibration amplitudes. In Fig. 6.17 the condition numbers for the system calibrated from 2-20 zernike modes are shown. This was done for three different calibration amplitudes. It shows that there is a decrease in the condition number with the modulation amplitude in every case, excluding for a 2-mode system (only tip and tilt sensing), where it keeps approximately constant. This decrease

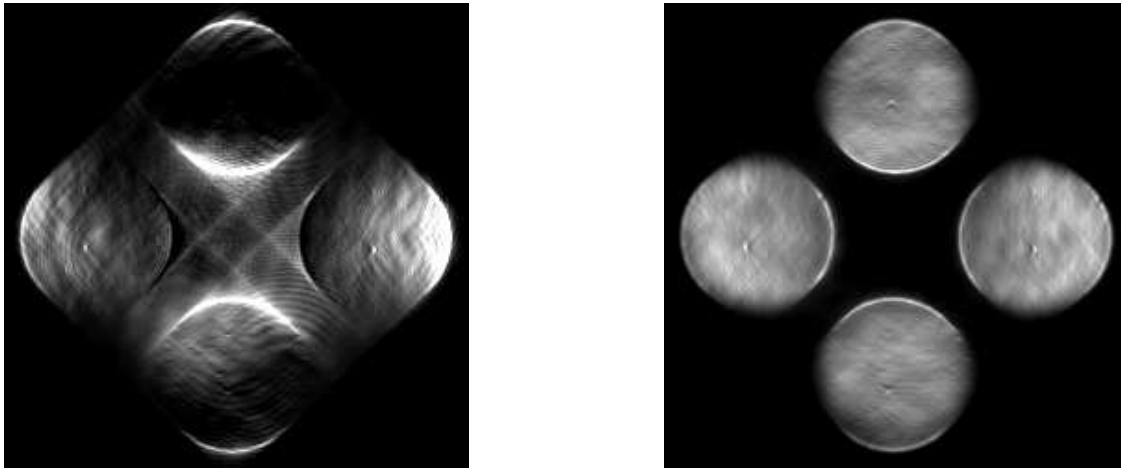


Figure 6.16: Images of the four pupils on the CCD, when the PWS is working in non-modulated regime (on the left side) and in modulated regime (on the right side).

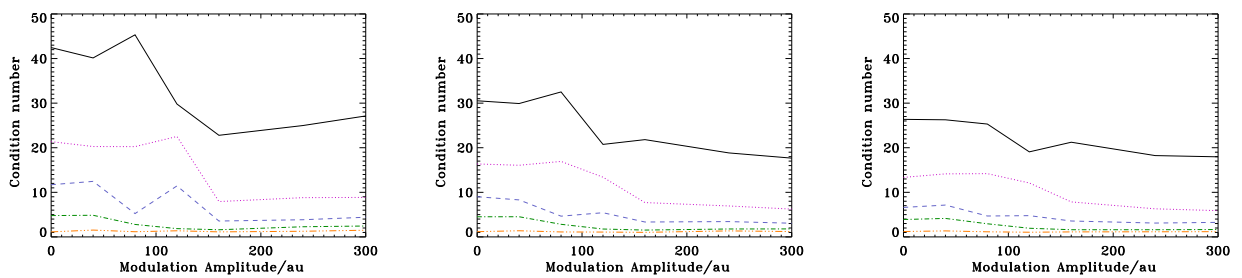


Figure 6.17: Here the condition number is plotted as function of the modulation amplitude. In each figure this is plotted for a system calibrated with 2 (red), 5 (green), 9 (blue), 14 (pink) and 20 modes (black) with different colors. The three figures show the system calibrated with different amplitudes (-10, -15 and -20 au from left to right).

is not constant, the condition numbers keep approximately constant till modulation amplitudes between  $50\text{-}100\ \mu\text{m}$ , then decrease more or less steeply till  $150\ \mu\text{m}$ , and remain constant after that. The corresponding modulation amplitudes can be expressed in  $\lambda/D$  units, the full width at half maximum of the diffraction limited PSF. The steep decrease starts around the size of  $0.5\text{-}1.0\ \lambda/D$ . This is approximately the size of the focus on the pyramid or a bit less, so it is very likely that it is the reason for the decrease. When the modulation has the size of at least  $0.5\ \lambda/D$  the spot crosses all four sides with the FWHM. The fact that there could not be seen any increase in the condition number after that point may have a variety of reasons like static aberrations present in the system and the roof shaped tip of the pyramid. These issues are analyzed in the following sections.

The difference in the condition numbers with the modulation amplitude has effect on the number of independent modes that can be calibrated by the system. In case the condition number is too

high the set of modes does not allow a stable closed loop regime. This is a first indication that the system will be able to close the loop with higher order modes if it is modulated. We see in Fig. 6.18 five different initial pseudo-random combinations of aberrations, which are corrected in a static closed loop. This means that the aberrations are sent to the DM and the signals are measured with the PWS. With the corresponding reconstruction matrix the combination of mirror commands which is appropriate to correct these aberrations, is calculated. To achieve more stable loops, a gain factor of 0.5 is multiplied with the mirror commands. These are sent to the mirror and the next measurement follows. The results shown are for 40 correction loops. After 10 loops an interferometer image is taken to check the mirror surface. The RMS of this surface measurements is shown in the vertical axis. The correction performance of reconstructors for two different modulation amplitudes as well as for no modulation is here demonstrated.

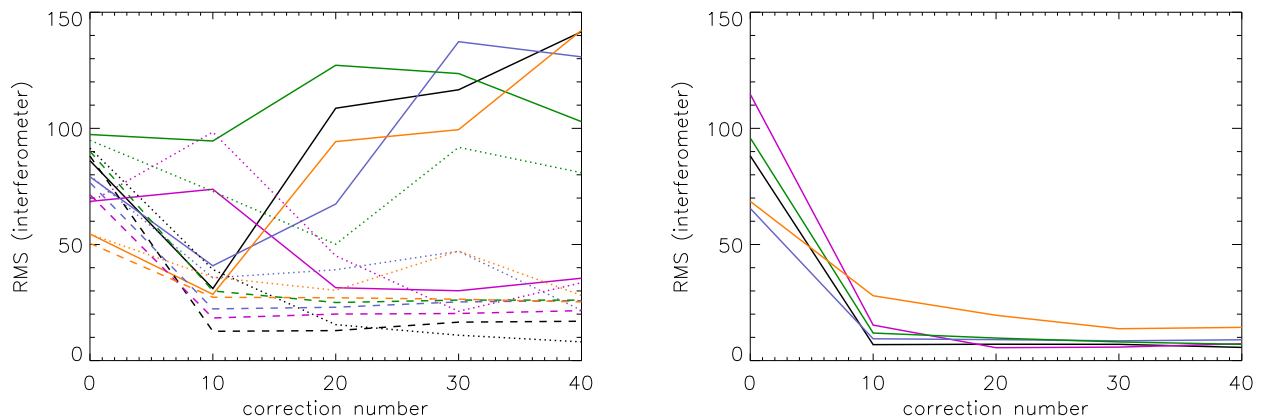


Figure 6.18: The RMS through different closed loop sequences of 40 cycles is shown, as a function of the correction cycle number. The effective RMS for the PWS is twice the value in the vertical axis, because the reflection at the mirror introduces double its deviation into the light path. The different colors correspond to different initial deformations of the DM. The system was calibrated in each case with 14 zernike modes, with an amplitude of  $-10$ . The number of pixels per diameter is 5. The continuous line shows the evolution of the system without modulation, the dotted line is for a modulation amplitude of  $40 \mu\text{m}$  and the dashed line for  $120 \mu\text{m}$ .

On the right side the results of corrections of the same five aberrated surfaces are shown, this time for a system calibrated only with 9 modes. The lines plotted show the evolution of the correction for the non-modulated case.

This exemplifies the fact that with modulation the same wavefront aberration can be better corrected and the loop does not diverge so frequently. Even for the small modulation amplitude (which is  $40 \mu\text{m}$ ) this stabilization shows. In the case of only 9 modes calibrated the loop closes very easily without modulation and the DM surface gets flat, as can be seen on the right side of Fig. 6.18. Very interesting is to note the fact that the surface RMS after the 40 cycles is lower in this case, than in the cases of 14 modes.

For this setup the calibrated modes without modulation have high cross-talk, especially for modes higher than z8. They show high cross-talk especially with the astigmatism of lower order. Since in this measurements the mirror was not flattened, but only biased to a constant value (see Section 6.3.4), the astigmatism is also a static aberration, which is introduced into the system by the intrinsic deformation of the DM. This affects the estimation of the coefficients of this modes (see Section 6.6 for discussion on the effect of static aberrations).

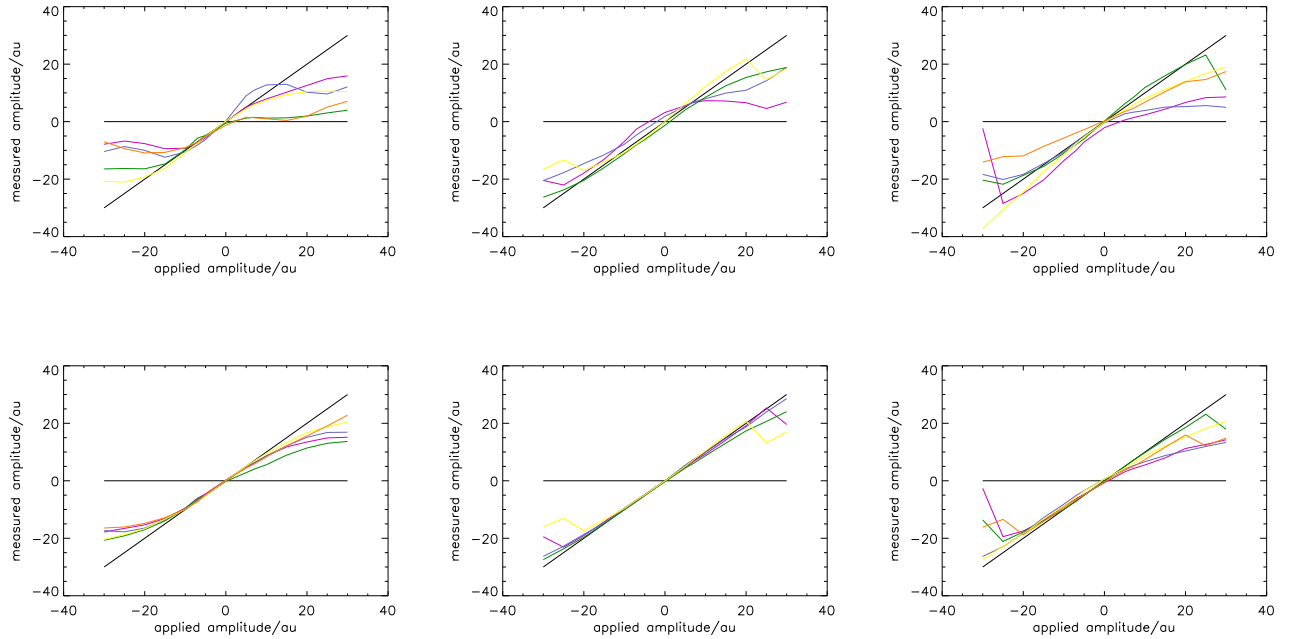


Figure 6.19: In these plots the amplitude measured by the PWS as a function of the applied amplitude is shown for the first 14 modes. The straight line has a slope of 1, so that it would be the answer of a perfectly linear sensor. The upper row shows the results for 0 modulation and the lower one corresponds to a modulation amplitude of  $85 \mu\text{m}$ . The 14 modes are distributed over 3 plots to avoid overlap of the lines. The color sequence for increasing mode index is purple, blue, green, yellow and orange. The linear range for the measurement of modes with modulation is bigger than with no modulation. The behavior of the modes in terms of linearity is different for different modes in the 0 modulation case. (The calibration amplitude was  $-10 \text{ au}$  for all measurements.)

The linear range of the sensor was estimated by open-loop measurements. Sequentially the modes were applied with increasing amplitude and measured by the PWS. This was done with and without modulation. It can be seen in Fig. 6.19 that especially for the low order modes z0 to z4 the sensor behaves more linear in modulated regime. In the non-modulated regime the tilt is overestimated, due to the fact that this mode has the highest RMS for a given calibration amplitude, in this case exceeding the linear regime. Generally the aberrations are underestimated, which by itself should not be a severe problem. After some correction cycles the correction should have approached the real value. Also the control system may take this effect into account, increasing or decreasing the gain in the most simple case. One other problem, which can

also be seen in the not modulated case, is the fact that some modes do not measure correctly the 0. This leads to the result that a complete correction of the corresponding mode is not possible. A solution may also be given by an appropriate control system, which adapts the correction of each mode to the actually measured behavior.

## 6.5 Effect of the pyramid roof

In Section 3.4 the problem of a non-negligible tip or even a roof-shaped tip of the pyramid was described. Especially in the latter case this alters the measurements made by the pyramid sensor due to the non-symmetric light-spread over the four sides. It is not possible to solve this problem by simply using a suited normalization which could be different in every pupil because the asymmetry in illumination changes with the size and shape of the spot on the pyramid and thus with the residual aberration, which changes during correction as long as the diffraction limit has not been reached.

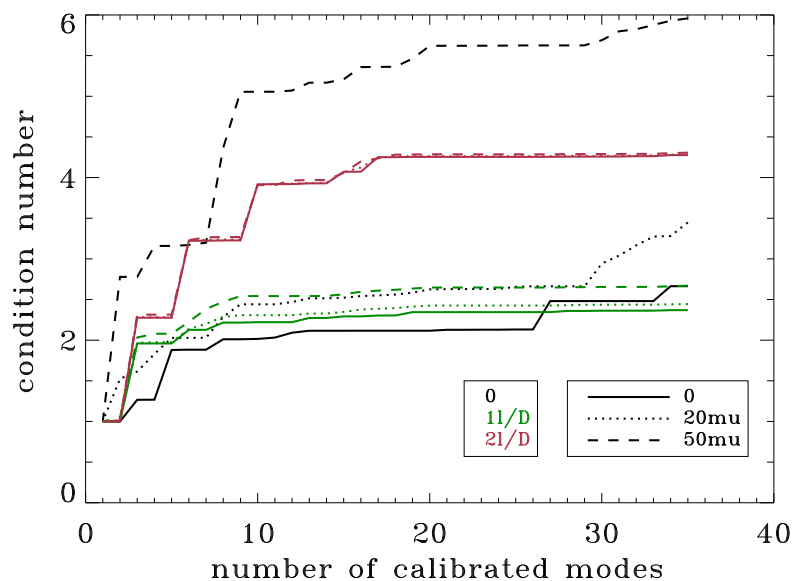


Figure 6.20: The condition number for systems modulated with modulation amplitudes of 0,  $1\lambda/D$  and  $2\lambda/D$  as a function of the number of calibrated modes is shown for roof sizes of  $0\ \mu\text{m}$ ,  $20\ \mu\text{m}$  and  $50\ \mu\text{m}$ . The system used has a  $\lambda/D=107\ \mu\text{m}$ , which corresponds to 12.8 pixels. The calibration amplitude is 0.1 rad.

In Fig. 6.20 the effect of roof shaped tips with different sizes is shown using a numerical simulation. For a modulation amplitude of  $2\lambda/D$  the effect of the roof is negligible in terms of the condition number. For a modulation amplitude of  $1\lambda/D$  (which corresponds to  $107\ \mu\text{m}$ ) a roof size of  $50\ \mu\text{m}$  already increases the condition number. The effect is very pronounced in the non-modulated case where the bigger roof size more than doubles the condition number. In this

case, with a roof size of  $50\ \mu\text{m}$ , like the pyramid used in the laboratory setup has, the condition number is higher than with modulation already with only two modes calibrated. This is for sure a reason for degradation of the measurements without modulation in the laboratory.

For an AO system working in closed loop, having an almost diffraction limited PSF, this effect may be very harmful. The pyramid roof should be smaller than  $20\ \mu\text{m}$  for a system like the laboratory setup or PYRAMIR, which has the same spot size on the pyramid for the lowest wavelength range.

## 6.6 Static aberrations

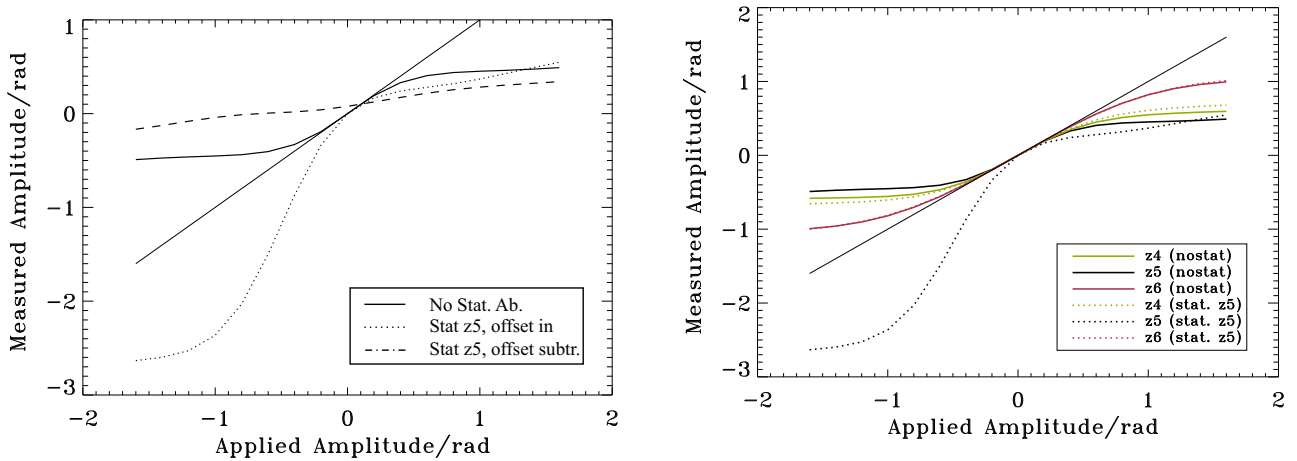


Figure 6.21: On the right side it is shown how a static astigmatism ( $z_5$ ) changes the linearity measurements of the correspondent mode and of other modes like defocus ( $z_4$ ) or the  $90^\circ$  rotated astigmatism ( $z_6$ ).

If a PWS-system has some static aberrations which are in the non-common path of the sensor and science camera, it can not correct them without introducing aberrations into the science path. The system has to be calibrated with the static aberrations, but they will nevertheless increase the PSF size, so that in worst case, the sensor stays in non-linear regime even when there are no aberrations to be corrected. Even if this is not the case, some aberration included in the calibration will change the linear range. In Fig. 6.21 it is shown what happens when the offset signals are not subtracted from the calibration measurements: The system gets insensitive to the corresponding mode and it does not measure correctly the 0. Subtracting the offset signal changes the linearity curve for the corresponding mode. It gets insensitive in one direction, because it reaches the saturation in this direction. For other modes, which are not present in the system as static aberration, the change in the linear range is very small.

The laboratory measurements also show this effect for the not modulated case. The system

has some intrinsic astigmatism introduced by the DM is biased to a value of 64. Since the intrinsic defocus of the DM is not corrected, but taken into account optically, it is very likely that there is some residual focus error left, which could not be seen in the alignment process, especially because there are also other deformations like the astigmatism which make the pupil pattern non-uniform. In Fig. 6.19, in the top left plot, where the linear range of the not-modulated sensor for the first 5 modes is shown, the curves for astigmatism and defocus have this saturation effect for positive amplitudes. This effect could be taken into account in the reconstruction process, if the curve is measured in advance. The error in the estimation of the best correction could be reduced.

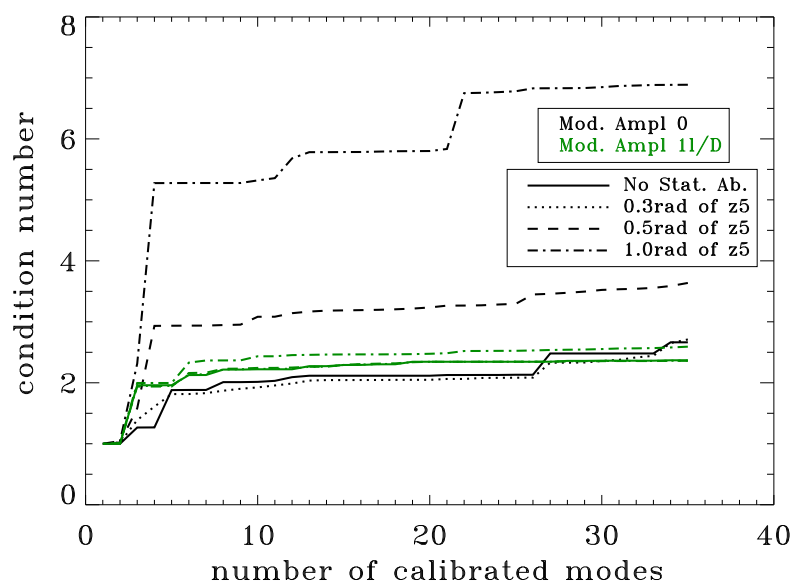


Figure 6.22: This figure shows the effect of modulation on the condition number of the system with different amplitudes of static aberration. Modulation amplitudes of 0 and  $1\lambda/D$  are represented.

In Fig. 6.22 are plotted the condition numbers as function of the number of calibrated modes for systems with different amplitudes of static aberration, and the effect of modulation on this systems performance. This simulation was done for conditions similar to the laboratory setup (pupil diameter of 4.5 mm, a wavelength of 632.6 nm and an F-ratio of 170). The simulation was done with arrays of  $1024 \times 1024$  pixels and the number of pixels per FWHM of the diffraction limited PSF is 12.8. The number of pixels per pupil diameter is 8 and the maximum number of calibrated modes was 35. It can be seen that above a certain tolerance limit of the system, the static aberrations increase the condition numbers, as explained in the next paragraphs.

In the case of no static aberrations present in the system, the condition number increases when modulated, as has already been showed in Section 6.4 through numerical simulation.

Static aberrations, which are present in the system (in the case of Fig.6.22 it is a static astigmatism) cause the condition numbers to increase (although there is some tolerance range in which the increase can not be seen or there is even a decrease in the condition number as can be seen with 0.3 rad of astigmatism.).

By introducing modulation in this kind of system, the condition number stabilizes on the level of the modulated system without static aberration. The increase due to static aberrations can be delayed with the use of modulation. This can be seen in the overlapping of the first three green lines.

For PYRAMIR the requirement has been established at a maximum of  $0.1\lambda$  of static aberration. The optimization of the actual optical design predicts not more than  $0.05\lambda$  of non-chromatic static aberrations.

## 6.7 Spatial filter

A circular pinhole just in front of the pyramid in the focal plane acts as a spatial filter on the wavefront signal. Spatial filters with diameters of 0.2 mm, 0.5 mm, 1.0 mm, 2.0 mm and 5.0 mm were mounted in the setup. The effect of this filtering on the CCD image is simulated in Fig. 6.23. One can see that the pupils get blurred, due to the high frequencies, which are filtered out. In these configurations the system was calibrated using the method described before (with 7 au) for an increasing number of modes. The condition numbers of the matrices obtained are shown in Fig.6.24. It can be seen that for the 0.2 mm pinhole the increase is especially steep if more than 7 modes are calibrated. The figure also shows that the condition numbers for the 2.0 mm pinhole are higher than for other smaller diameters. This is probably due to a measurement error and is not meaningful.

With these calibrations a set of randomly generated aberration patterns were corrected in a static closed-loop. The number of modes used for correction were 14. The mean result of the evolution of these corrections can be seen on the right side of Fig.6.24, where the mean Strehl ratio after each correction cycle is plotted. It can be seen that an almost perfect correction could be achieved in every case, except for the smallest field stop with 0.2 mm. With the 2.0 mm pinhole the system was able to correct the aberrations in most cases, but was less stable. This worse performance can be explained by the fact that the matrices obtained in the calibration had higher condition numbers.

The limiting size of the pinhole for the laboratory setup is between 0.2 mm and 0.5 mm. This corresponds to  $2-5\lambda/D$  (in terms of diffraction limited PSF size to 2-5 FWHM).

The Nyquist sampling theorem states that there can not be any frequency content with absolute value above  $\pm 1/2d$ , where  $d$  is the subaperture size in the pupil plane. In the laboratory setup this corresponds to  $\pm 4\lambda/D$ , where  $D$  is the entrance pupil size. This means a field stop with a diameter of  $8\lambda/D$  cuts out the frequencies, which can not be sensed due to the sampling, preventing aliasing. A smaller field stop will cut out frequencies, which can be sensed and

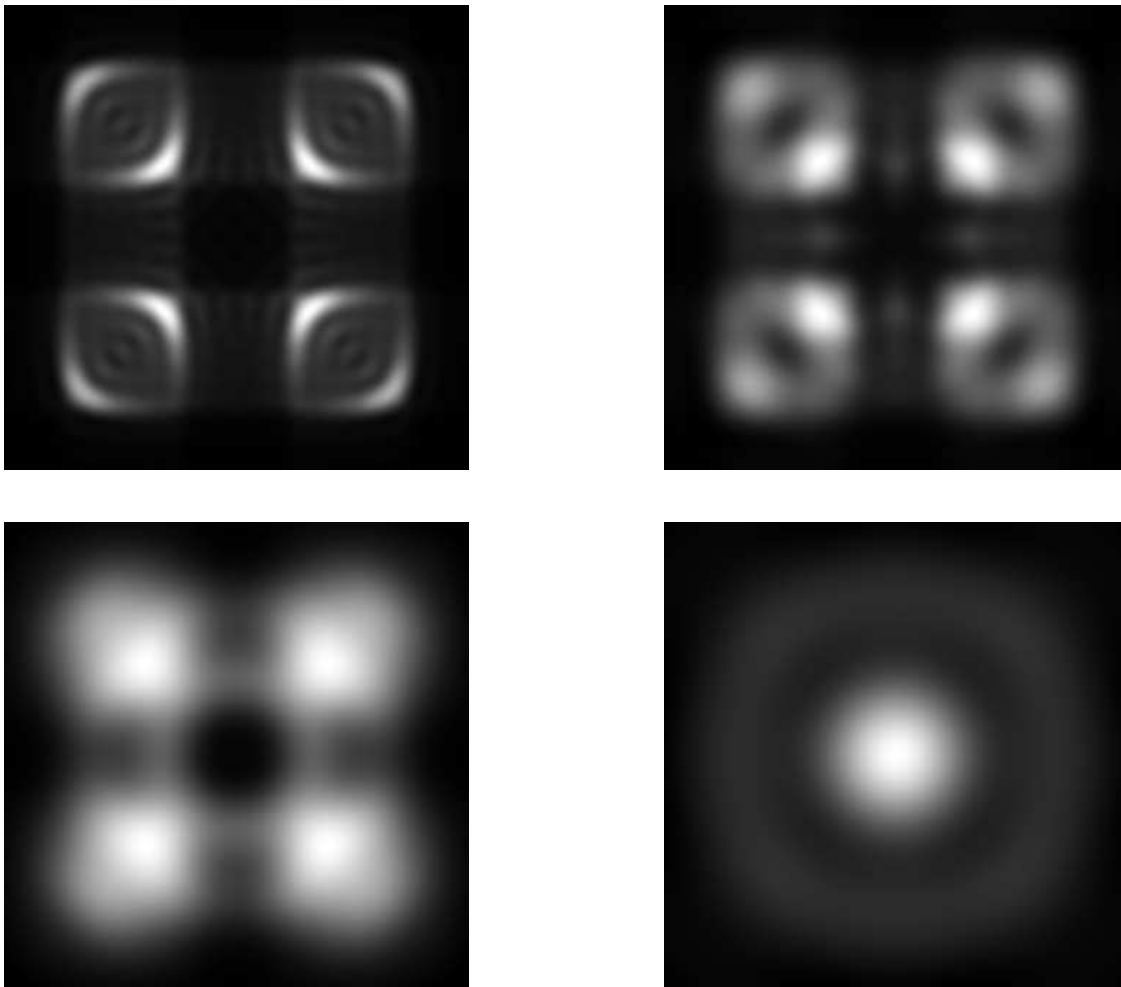


Figure 6.23: Simulated images of the four pupils on the CCD for field stops with different diameters. Starting from the upper left corner the images correspond to a stop radius of  $5\lambda/D$ ,  $2.5\lambda/D$ ,  $1\lambda/D$  and  $0.5\lambda/D$ .

therefore corrected (if the DM has enough degrees of freedom). This means that a field stop with less than 0.83 mm of diameter cuts out reachable information. It is not noticeable any loss in performance in the corrections done because the number of corrected modes is only 14. For sensing 14 modes 8 pixels are already oversampling.

For the PYRAMIR instrument (see Chapter 7 for design details) the same reasoning allows a field stop of 1.8-4.2 mm diameter (J-K band) due to the 18 pixels per pupil diameter. Since the DM has only 10 actuators per diameter, the correctable frequencies are lower than the sensed ones, what allows a smaller size of the field-stop. In the case of 8 pixels, like it was planned for the AO-MUX detector, the field-stop diameter would stay in the range of 0.8-1.9 mm. The pinholes available in PYRAMIR will be in the range of 2-10 mm.

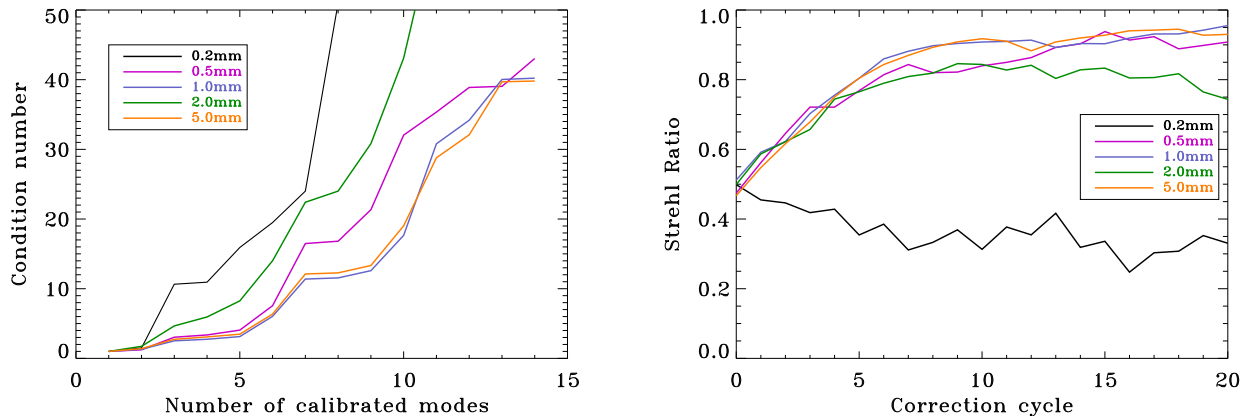


Figure 6.24: The results of the laboratory measurements using the PWS with a field stop of variable diameter in front of the pyramid. On the left the condition numbers obtained for different calibrations and on the right the evolution of the residual RMS during a static closed loop correction of random aberrations.

## 6.8 Three-sided pyramid

Using the simulation of the full PWS the amount of light lost in the refraction process through the pyramid was estimated. In the case of a nearly perfect edge and tip size there is no significant difference in relation to the four-sided case, as can be seen in Fig.6.25, although the light loss is slightly lower in the three-sided case. The proportion of light lost is reduced at a similar rate with increasing aberrations. Having a non-negligible tip and edge size the effect of having 3 instead of four edges can be considerable, as seen on the right side of the same figure. Not to forget also are the disadvantages of the presence of the roof, which creates an asymmetry in the pupil illumination, as shown in Section 6.5. Since for a three-sided pyramid there is no roof formation, this asymmetry can be avoided if the three sides of the pyramid have the same size.

A closed loop correction for a 3.5 m telescope at a wavelength of  $2.2 \mu\text{m}$  with a non-modulated PWS was simulated for a four-sided and a three-sided pyramid. The F-ratio of the beam focussed on the pyramid was 100. Screens of  $1024 \times 1024$  pixels were used and the pupil size on the detector was rebinned to 8 pixels per diameter. The atmospheric phase screens simulate very good seeing conditions with an  $r_0 = 0.5$  m. The correction gain is set to 1. The simulation for a *very bright* star is done with no photon statistics, a perfect detector and full transmission of the optics. For the stars of magnitude 6 and 8 the photon statistics is included, as well as a real detector (based on the planned AO-MUX characteristics) and a transmission factor for each of the optical components. The results are shown in Fig. 6.26, where the result for each correction cycle is shown. The integration time of the detector is 3 ms and the turbulent phase screens used are spaced 1 ms. This means that only after 3 screens, were the detector is integrating, the correction is applied, what explains the steps in the curves. In all cases the AO system closed the loop and increased the Strehl ratio, only for the less bright guide star with the three-sided pyramid it was not able to close the loop. This shows that although the threesided pyramid

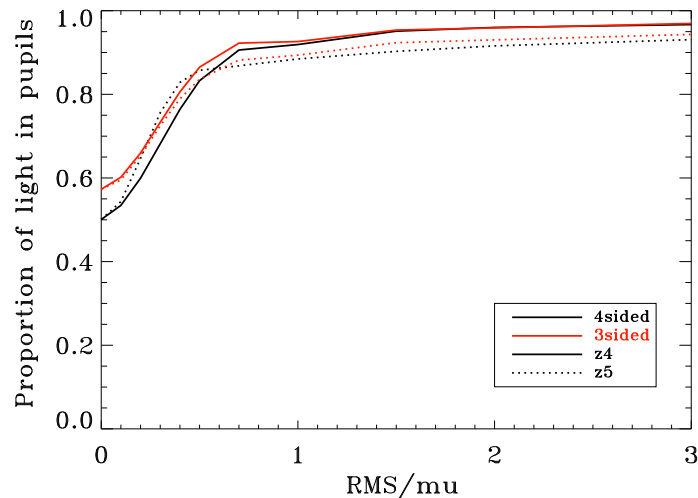


Figure 6.25: Simulation results for the proportion of light, which can be detected inside the four pupils on the detector, in relation to the amount of light present before refraction by the pyramid, as a function of the RMS of the wavefront (see also Fig. 6.6). The simulation parameters were a 3.5 m telescope, working with a  $2.2 \mu\text{m}$  wavelength and a F/100 beam. The edge size is almost perfect smaller than  $10 \mu\text{m}$ . The difference between a four and threesided pyramid in the amount of light lost is very small, having a slightly lower loss in the threesided case. This is because the area around the tip which is covered by edges is smaller, resulting in less light refracted to outside the pupils.

has some advantages from the production side, it may be more unstable especially in low-light conditions, due to a worse propagation of the measurement noise. In Section 3.4.7 it has been shown analytically that in the case of a low read-out noise detector and a weaker star, the four-sided pyramid performs better than a three-sided one.

Results from simulations of a modulated PWS made by Clare and Lane (2003), where the measured wavefront is compared to the incoming wavefront (distorted by atmospheric turbulence), show less error in the reconstructed wavefront for the four-sided pyramid than for the three-sided one. More sides translate into a smaller reconstruction error if no other effects are taken into account.

## 6.9 Future developments

There is the possibility of upgrading the laboratory setup with a set of rotating phase screens simulating the atmospheric turbulence in various conditions. These have been analyzed by Butler et al. (2003) and can be mounted in the setup. The rotation will be performed by a motor, which allows to perform a rotation with different velocities. This would allow to simulate different seeing conditions as well as adapt the rotation to the loop bandwidth achievable in the laboratory.

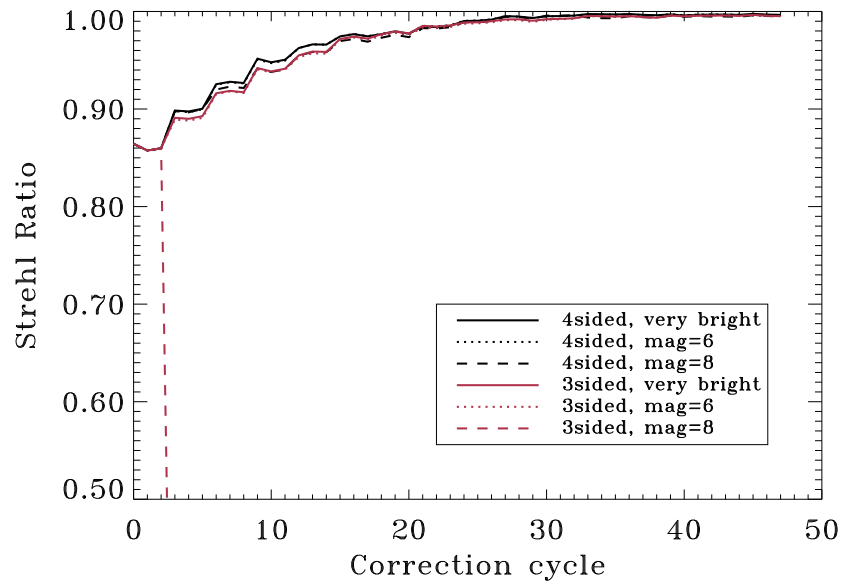


Figure 6.26: Simulation of a closed loop correction for a 3.5 m telescope at a wavelength of  $2.2 \mu\text{m}$  with a non-modulated PWS for a threesided and a foursided pyramid. The simulated seeing is very good ( $r_0=0.5 \text{ m}$ ). Guide stars with two different magnitudes were used and a simulation without photon statistics nor limitations from the detector or the optics (bright star).

The number of modes correctable without modulation can for sure be increased through a better control of the DM. The DM should be characterized and the quality of the modes should be increased. This would mean that they would be more independent from each other, the calibration would give lower condition numbers and the corrections could be more effective. With a better definition of the modes the dynamic range of the DM could be fully used.

A set of three-sided pyramids have already been characterized with the profilometer. Mounts for the assembly in the setup are also available and the software for the signal calculation has been written. It is for sure very interesting to compare the performance and to get an idea, what the advantage of a perfect tip would be. Even if the noise propagation may be worse, the fact that there is no roof could compensate or even be more advantageous.

The laboratory system has also been used for a comparative study between Shack-Hartmann and Pyramid Sensors<sup>3</sup>. Although there have not been published results yet, this is for sure a very interesting project.

---

<sup>3</sup>Together with the research group of Biomedical Optics at the University of Heidelberg, which studies wave-front sensing and adaptive optics in the human eye.

# Chapter 7

## The PYRAMIR instrument

The objective of the PYRAMIR project is to complement the Calar Alto Adaptive Optics System - ALFA - with a new pyramid wavefront sensor working in the near IR, replacing the previous tip-tilt tracker arm. The sensor will work at the wavelength range of J, H and K bands. Here the optical design is described and issues like the image quality and chromatic effects due to band sensing are discussed. To gain experience, a laboratory pyramid wavefront sensor was set up, with its optical design adapted to PYRAMIR. This setup allowed to establish aligning techniques and perform different tests.

Sensing the wavefront in the infrared poses particular requirements like a cooling system for the opto-mechanical components. Most of the PYRAMIR instrument parts are kept inside a liquid nitrogen cooled vacuum dewar to reduce thermic radiation. The mechanical design of the cold parts is described here. The infrared detector which is planned to be used is a PICNIC-array, the successor of NICMOS3 from Rockwell, as one option, together with the AO-Multiplexer (AO-MUX) due to its very low read-out noise. As preliminary option a Hawaii I detector will be integrated until the AO-MUX is available. It is described how the integration of the system into the optical, mechanical, electronics and control architecture of ALFA is expected. Updates on this project have been given in Costa et al. (2003a) and Costa et al. (2004b).

### 7.1 Optics

PYRAMIR was developed for integration in the existent adaptive optics system ALFA on the 3.5 m telescope on Calar Alto in Spain, as alternative to the existent Shack-Hartmann sensor (SHS), which is currently in use and operated with visible light (with a CCD detector). The Pyramid wavefront sensor is going to work in the near-infrared, in a wavelength range of  $1.0 \mu m - 2.35 \mu m$ .

**The ALFA optical design** In Fig. 7.1 a representation of the optical bench of the ALFA system is shown, with the SHS and the new PWS. The optical design of ALFA (Hippler et al. (1998)) consists of two off-axis paraboloids. The first images the telescope pupil onto the deformable mirror, the second re-images the telescope focus on the infrared science camera at the same position as the telescope's Cassegrain focus.

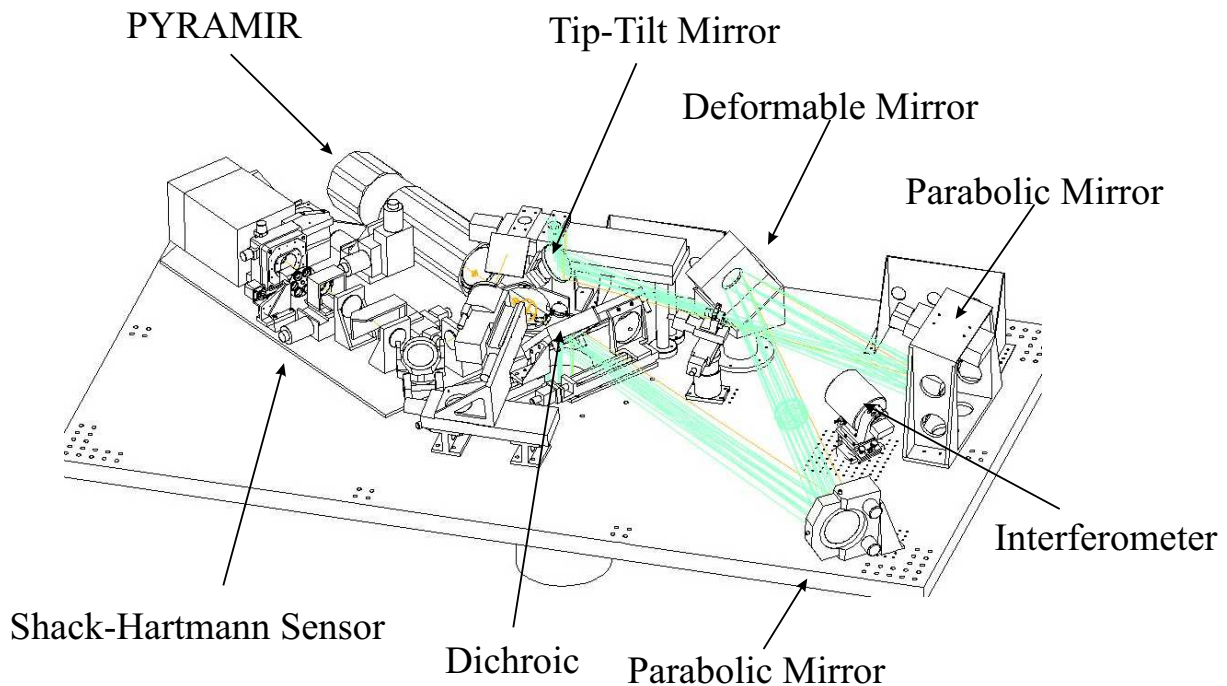


Figure 7.1: The CAD drawing of the ALFA board, with all its optical and mechanical components. In the upper left corner there is the cylindrical dewar where the optics of PYRAMIR is enclosed.

The DM was purchased from Xinetics Inc., USA. It has 97 PMN (lead magnesium niobate) ceramic piezo actuators with a  $2\ \mu\text{m}$  interactor stroke. There are 11 actuators per diameter of the telescope.

The telescope can still be used without ALFA just by sliding two mirrors out of the beam. The default focus of the telescope is  $F/10$ , which ALFA converts into an  $F/24$  focus. Before focussing on the science camera, part of the light is split. When using the visible wavefront sensor, the infrared light is reflected to the science camera and the visible light is transmitted to the wavefront sensor.

**The PYRAMIR optical design** A schematic representation of the PYRAMIR optical design is represented in Fig. 7.2. For PYRAMIR the visible/IR beamsplitter has been substituted. There will be installed two new dichroics: one JH/K, which transmits J and H bands to the science camera and K band to the wavefront sensor, the other K/JH, respectively splitting the light. A choice of wavelength-unsensitive beamsplitters, like 10/90% and 80/20%, will be used standardly, the first one to use the wavefront sensor for faint objects at the expense of longer integration times on the science camera. The dichroics have a diameter of 70 mm, approximately half of the previous ones in ALFA. The thickness of this dichroics was also reduced from 10 to 4 mm, to reduce the non-common path static aberrations. Since the dichroic is mounted in an angle of 45 degrees, the resulting aberrations and shifts obtained in transmission had to be compensated with a silica compensator plate.

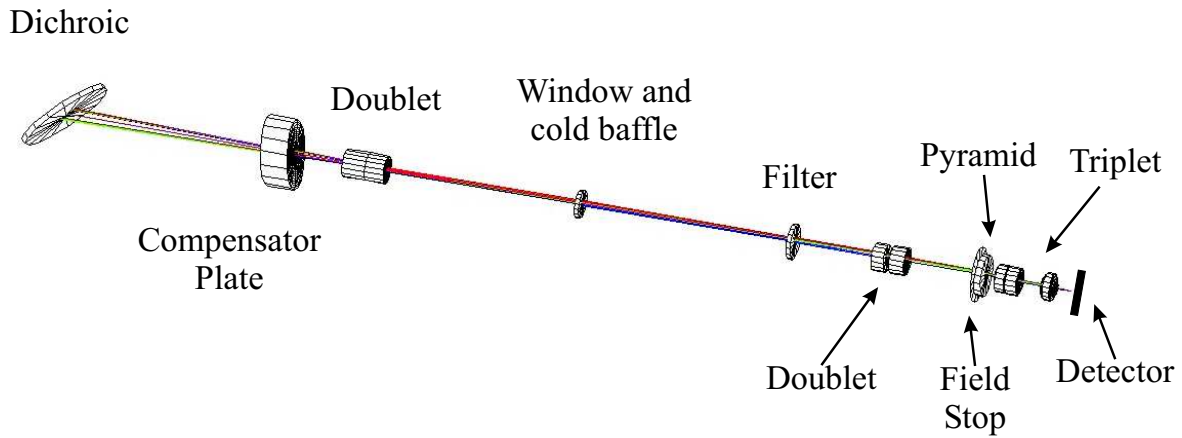


Figure 7.2: The PYRAMIR optical design, starting with the new dichroic, which splits the infrared light into the sensor after passing the first components of ALFA.

The wavefront sensor will work is J, H and K band. For this reason the optical design was optimized for the range of  $1.0 - 2.35 \mu\text{m}$ . The field of view has a diameter of  $4''$ . For dithering the infrared science field by moving the telescope, the PWS can be moved through a x-y-stage by  $\pm 5''$  to follow the reference star.

To correct the system for the static aberrations produced by the dichroic, which can affect the performance of the system, degrading the linearity of the sensor (Costa et al. (2004a)), a tilted silica plate is positioned after the dichroic. The static aberrations remaining in the systems optical design are mainly chromatic (for a quantitative analysis see Fig. 7.3 and the next paragraphs). The non-chromatic errors were reduced to  $0.05\lambda$ .

The layout of PYRAMIR consists basically of a combination of two doublets, which focus the beam on the tip of the glass pyramid. The F/24 beam of ALFA is transformed in a F/100 beam. The full correction for static aberrations and the telecentricity is only achieved in combination with the second doublet. The latter is required because a shift of the PWS in the field would otherwise slightly change the angle of incidence on the pyramid. PYRAMIR's optical components are partially outside the dewar. As can be seen in Fig. 7.2, the first doublet, a cemented CaF<sub>2</sub>/FusedSilica lens with 20 mm is at ambient temperature, the second, an spaced CaF<sub>2</sub>/FusedSilica combination with the same diameter, is already inside the dewar in the cold environment at 77 K. The dewar window out of fused silica has a thickness of 3 mm. The calculated bending through vacuum ( $5.9 \mu\text{m}$ ) and the therefore resulting radius of curvature (34000 mm) is negligible. Also in the cold environment, before the second lens group, a filter wheel allows to choose the wavelength range for the sensor. This is a necessary complement to the first dichroic due to the chromatically different refraction of the atmosphere, especially at larger zenith distances (Costa et al. (2003a)). The thickness of the filters is 3 mm, the diameter is 1 inch.

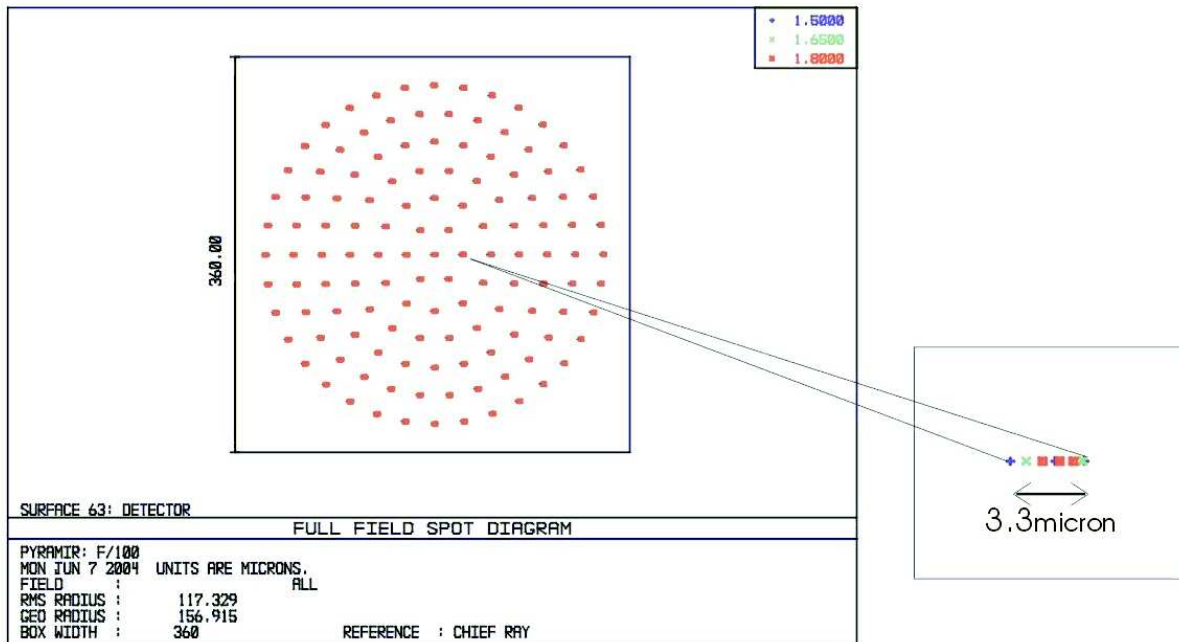


Figure 7.3: In this figure one of the four pupils on the detector is represented. The pupil diameter is  $320\ \mu\text{m}$ . The interior square with  $320\ \mu\text{m}$  side length corresponds to 20 pixels on the detector. The represented image is in H band, for the complete field of view. In the small square a zoomed extract of the pupil is shown. We see the quality of the image, which is  $3.3\ \mu\text{m}$  for this band, along the full field of view.

In the focal plane lies the tip of the pyramid, which separates the light in four beams. It consists of a four-sided fused silica prism, transmissible in the infrared. The angle of each of the sides with the horizontal is  $1.5^\circ$ . This angle, together with the specification for the tip quality of  $10\ \mu\text{m}$ , was very difficult to achieve. Despite the considerable difficulties found in the manufacturing process, we have now characterized very promising pyramids (see Section 6.1). The thickness of the pyramid is 5 mm. Together with the small angle this reduces the chromatic aberrations of the light traversing.

Immediately before the pyramid a field stop limits the FoV and therefore also the background from the sky. This field stop will be changeable, ranging from 2 – 10 mm diameter. The effects on this stop on the performance of the PWS has been tested through simulations and lab-experiments (see Section 6.7 and Feldt et al. (2004)).

The spaced triplet of CaF<sub>2</sub>/Fused Silica/LiF forms the four pupils on the detector. The separation was made as small as possible, to minimize readout time. In the actual design they have 40 pixel diagonal center to center distance. Each of them has a diameter of  $320\ \mu\text{m}$ . This diameter corresponds to 18 pixels on the detector, a Hawaii-1 with  $1024 \times 1024$  pixels ( $18.5\ \mu\text{m} \times 18.5\ \mu\text{m}$ )

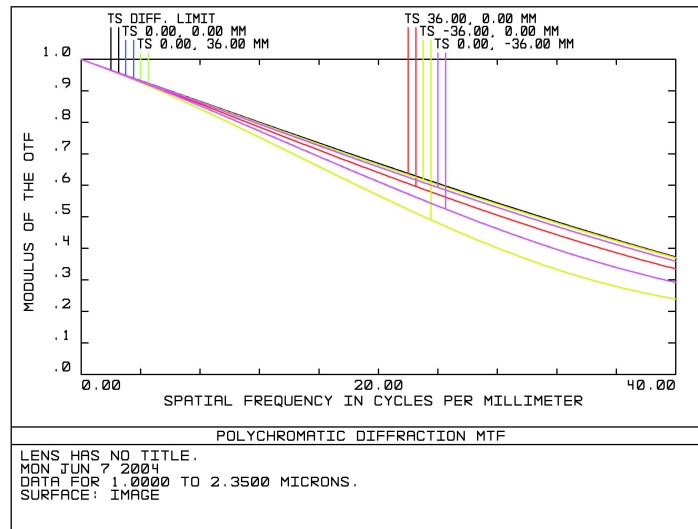


Figure 7.4: Modulation transfer function for the system imaging the DM on the detector. The diffraction limit is also represented in the plot. The frequencies are transferred almost diffraction limited at the center of the DM. For a more detailed discussion see the text.

from Rockwell. This detector has previously worked in Omega Prime at Calar Alto Observatory. It has been tested at MPIA (Ligori et al. (2004)) and it meets the requirements of PYRAMIR in terms of read-out noise and high frame rate. In future it is planned to upgrade PYRAMIR with the AO-Mux from Rockwell. This update is possible without changing the optics, only changing the detector, having instead 8 pixel per diameter pupils. One of the four pupils is plotted in Fig. 7.3. The quality of the image ranges from  $3.3 \mu\text{m}$  in H-band,  $5.5 \mu\text{m}$  in J-band to  $7.4 \mu\text{m}$  in K-band. This quality corresponds to a quality of 1/10 pixel to 1/5 pixel for the AO-Mux, for which the design was originally planned.

The analysis of the quality of the re-imaging of the deformable mirror on the detector can be done through the modulation transfer function (MTF) of the optical system, which starts with the DM in the ALFA adaptive optics system, has as limiting pupil the field stop in front of the pyramid and images the DM on the detector. The MTF for a field stop of 8 mm diameter is shown in Fig. 7.4. Having 10 mirror actuators per diameter, these will be imaged with  $32 \mu\text{m}$  per actuator on the detector. This corresponds to a frequency of 31 cycles/mm. The contrast of the transmission of this frequency ranges from almost diffraction limited at the DM center to 35% at the edge. The diffraction limit lies at 50%.

## 7.2 Laboratory setup

The laboratory setup was designed and built with the main objective of gaining experience on building a pyramid wavefront sensor system, in matters like optical adjustment techniques and optical quality tests (of the pyramids, for example), software routines for calibration and reconstruction and closed loop behavior in non-modulated regime. For this purpose the optical setup is similar to the one of PYRAMIR in some aspects. A detailed description of the setup is given in Chapter 5.

The optical adjustment of the components of PYRAMIR is not straightforward because the setup has to be mounted inside the dewar. This means that the detector can not be mounted at intermediate stages of the setup during the alignment process. As an example, the knowledge of the exact location of the focus is necessary so that the pyramid is positioned at the right place. If this is not the case, there will always be a small static defocus, which is not directly visible in the four pupils, but can be harmful for the system (see Section 6.6). Since the beam has a relatively high F ratio ( $F=100$ ) there is a certain range where it is not clear at naked eye where the focus is. Using a small pinhole, the focus can be found as being the point where the maximum amount of light falls on the detector. These and other techniques were developed during the optical alignment in the laboratory.

The software routines for finding the pupils on the detector and signal extraction, calibration and measurement have been developed and tested with the lab-setup. These techniques were adopted for the PYRAMIR software.

## 7.3 Mechanics

Most of the optical and mechanical parts of PYRAMIR are situated inside the vacuum dewar (see Fig.7.5). This dewar has two liquid nitrogen (LN2) tanks (volume 4.8 and 1.4 liters) which are designed in a way that nitrogen cannot drain off at any telescope orientation, if they are filled up only half. To guarantee a holding time of at least 27 hours three nested radiation shields are used. Two of them are thermally connected with one of the LNs-tanks each, the third shield is only passively cooled by the cold exhaust gas of the tanks. The cold plate is mounted directly on the inner LN2 tank and is so cooled to a temperature of 77 K. The dewar in principle is a diminished copy of the Omega2000 (Baumeister et al. (2002)) cryostat, which has proven to work very well. Three sets of spacers, made from glass fiber reinforced plastic separate the warm and cold structure and allow the cold parts to shrink and move in respect to the warm vacuum vessel during cooling-down. The cryostat is about 950 mm long and has a diameter of 216 mm, the total weight including nitrogen is about 30 Kg.

There are three motor driven elements inside the dewar. These are the filter wheel, the mask wheel and the detector z-stage, which allows the detector to be moved along the optical axis by  $\pm 1$  mm. Since all these elements work at a temperature of about 77 K, we use Phytron cryogenic stepper motors together with modified Harmonic Drive gears (reduction ratio 80:1) which are almost free of backlash (Rohloff et al. (2004)). Each filter wheel position can be checked by a

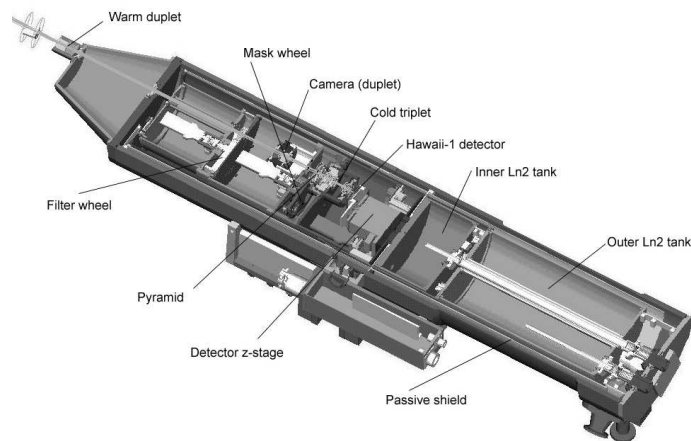


Figure 7.5: A section through PYRAMIR.

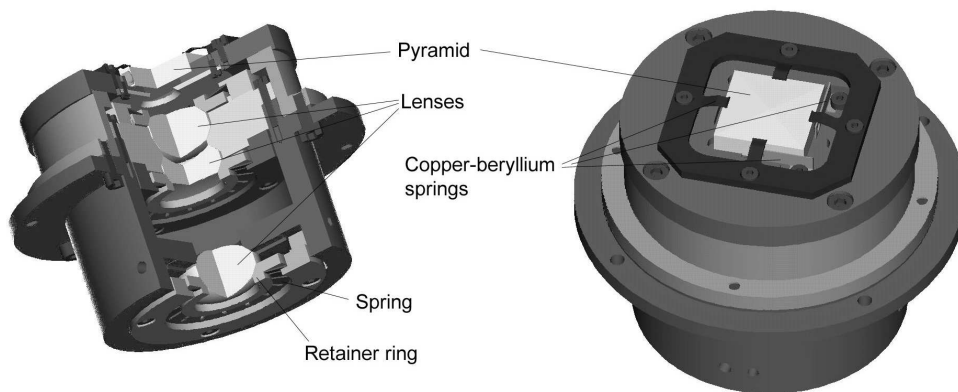


Figure 7.6: The cold triplet in PYRAMIR.

set of micro switches.

The wheels, both cold lens groups and the pyramid are mounted to thin-walled cylindrical supports that are piled up on each other. All these supports together also serve as the inner radiation shield.

The five cold lenses have a diameter of 20 mm and have 40° chamfers on both sides. They are mounted in aluminum mounts having the same kind of chamfers. This is necessary to compensate the mismatch of thermal expansion between the lens and the mount material during cool-down and warm-up of the optics. So the lenses can slide on the chamfers. This method is described in detail in Baumeister et al. (2002) for much bigger lenses; it works excellently in Omega2000.

Due to its rectangular shape, the pyramid is mounted by six copper-beryllium springs (see Fig. 7.6).

## 7.4 Detector

PYRAMIR will use in a first phase an  $1024 \times 1024$  Hawaii I detector from Rockwell Scientific, which has been developed for advanced astronomy and space telescope applications. The pixel size is  $18.5 \mu\text{m}$  and maximum pixel rate is 1 MHz. The quantum efficiency is higher than 0.6. The charge storage capacity is higher than 100000 electrons. It has 4 quadrants, which can be read-out in parallel through different channels. Since the four pupils are restricted to a small portion of one of the quadrants, a small window of  $64 \times 64$  pixels is addressed. This allows to achieve high frame rates of more than 150 Hz. This small window can be located somewhere on the detector, where the performance is best. In the best channel the read-out noise in correlated double sampling mode (reset of the frame followed immediately by one read-out and another read-out after the integration time) at 87 Hz is less than 10 electrons (Ligori et al. (2004)).

## 7.5 Thermic background estimation

The estimate of the thermic background noise was made for a 'worst case' situation, using the optical design. The amount of thermic photons that would reach the detector pixel was estimated for the case of all the light falling onto one pixel only (what of course is never the case), coming through the field stop before the pyramid. Further it was assumed that the PWS is located in an environment of 293 K temperature and the black body flux from such an environment that can optically enter the entrance window (baffle) of the infrared sensor was calculated. The result is nevertheless very low ( 150 photons/s in a spectral band from 2–2.3  $\mu\text{m}$ ), and the instrument will be limited by the detector or the sky background noise.

## 7.6 Limiting magnitude

The simulations of the PYRAMIR system were done using a model of the instrument programmed in IDL (see Section 5.2). The model contains all key-features of the system, which are:

**The telescope and optics** which in this model are represented only by a transmission factor of 0.45. No static aberrations were applied in the simulation described here.

**The DM** The deformable mirror, with its sampling of 10 actuators across the aperture, and its finite resolution and stroke.

**The pyramid** A pyramidal prism with a pin-hole of  $3''$  diameter in front. In this simulation no imperfections of the pyramid's shape were taken into account.

**The detector** with its flat-field accuracy, read-noise, dark-current, sensitivity, etc. In this case, it was assumed that the four aperture images match perfectly onto the pixel grid.

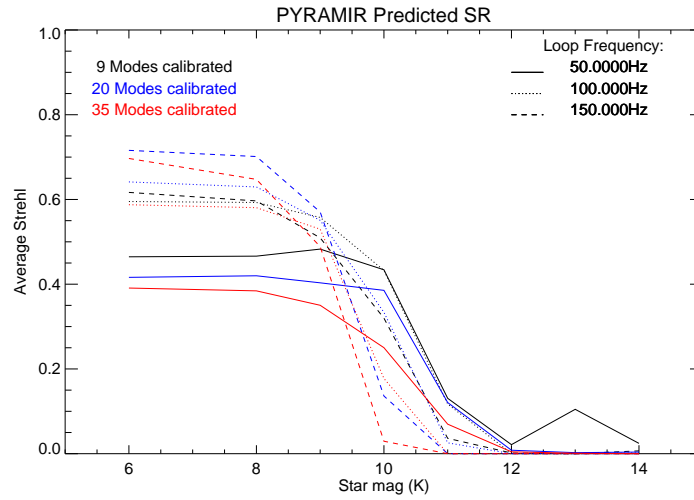


Figure 7.7: The results of the simulation: The resulting average Strehl ratio for closed loop corrections with different star magnitudes. This simulations were done for a system calibrated with 9, 20 and 35 modes and for three different loop frequencies.

A summary of the simulation parameters is given in Tab. 7.1 and the results are shown in Fig. 7.7. According to it the limiting magnitude can reach 12th magnitude in K-band in all cases simulated.

Telescope transmission (incl. ALFA)	0.45
Static Strehl ratio	1.0
No. of DM actuators	100
DM act. stroke	10 $\mu\text{m}$
Pin-hole diameter	3"
Aperture sampling on detector	17 pix
Detector quant. eff.	0.6
Detector flat err.	$1 \times 10^{-4}$
Detector read noise	15 $e^-$
Detector gain	5
Seeing ( $K$ )	0.5"
$\tau_0$ ( $K$ )	15 ms
No. of calibrated modes	9, 20, 35
AO loop frequency	50 Hz, 100 Hz, 150 Hz
Filter	$K$
Sky background	17 mag per square arcsec
Guide star mag	6, 8, 9, 10, 11, 12, 13, 14

Table 7.1: Simulation parameters.

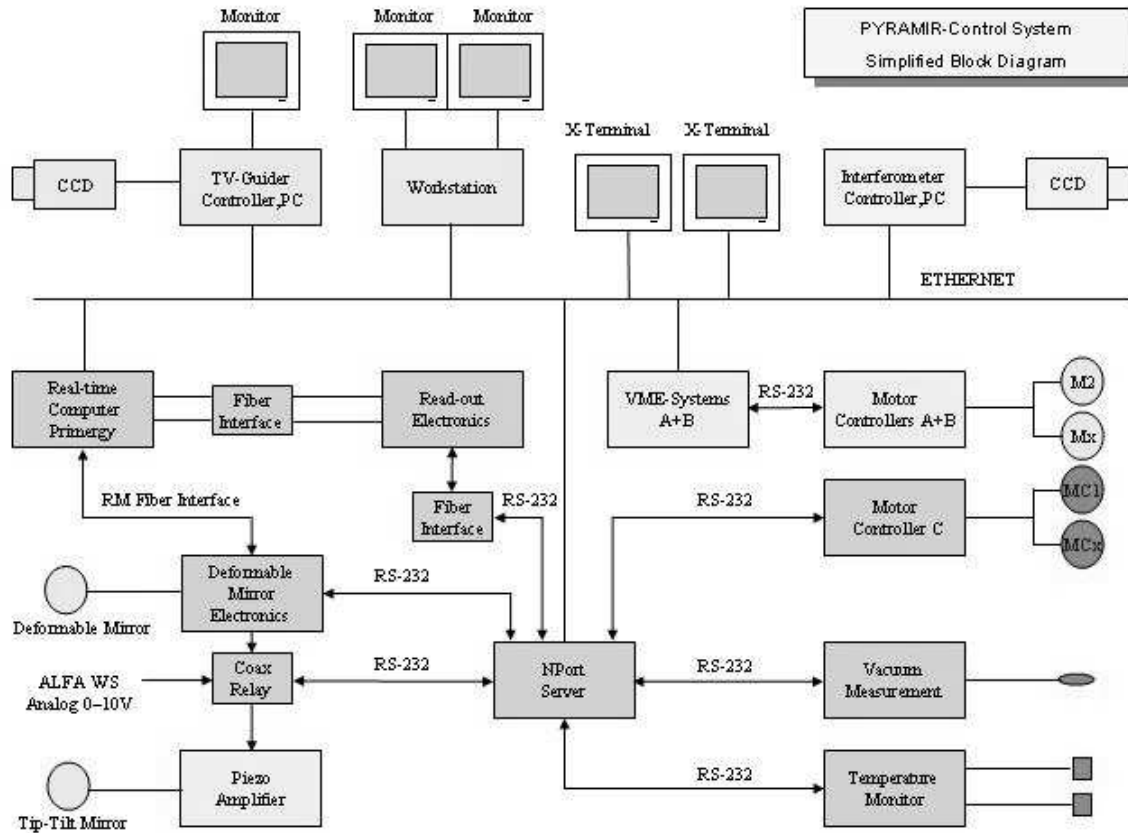


Figure 7.8: The PYRAMIR control system simplified block diagram. The components in dark gray are specifically developed for the new pyramid wavefront sensor. In medium gray we see the components from ALFA, which are still going to be used in the new WFS.

## 7.7 Electronics/Control

PYRAMIR will be a second high-order wavefront sensor integrated in the ALFA system. For this integration process to be as smooth as possible, a new real time computer (RTC) will be used, instead of the existing one (Hippler et al. (1998)). It is a Primergy R450 4-way rack server, which has two high-speed interfaces, one to receive data from the camera read-out electronics and another one to send data to the deformable mirror electronics, as can be seen in Fig. 7.8. The first will be a Gigabit fiber link, the latter will be a reflective memory system with PCI 64-bit 66 MHz transfers. The RTC is connected to the user workstation through ethernet. The workstation is connected to the deformable mirror electronics through a serial RS-232 interface. With the same type of serial interface it can be chosen from the workstation through a coaxial relay, which WFS to use.

The deformable mirror, a Xinetics Inc. with 97 PMN ceramic piezo actuators, has a controller from Cambridge Innovations, able to control up to 349 channels of this type of mirrors. The connections to the motor controller, vacuum and temperature measurement systems are also done through serial interfaces. The systems have been tested, the motors, compatible for use in vacuum and cryostats, are already in-house, and the motion controller, developed at MPIA, is ready to use. The connection through ethernet to all the different devices is done through a NPort Server.

The tip-tilt sensor from ALFA will be replaced by PYRAMIR, and tip and tilt will be sensed with the PWS. The previous tip-tilt-mirror electronics will also be controlled by the deformable mirror electronics.

## 7.8 Telescope implementation

It is planned to start with the assembly, integration and testing of PYRAMIR in the second half of 2004. The instrument has already been shipped to Calar Alto, where the integration is going to start soon. The optics integration will start very shortly after. The full instrument will be installed at the telescope in Calar Alto in December 2004. Technical first light is expected to be in the beginning of 2005.



# Chapter 8

## Conclusions and Future Prospects

In this work the use of a pyramid wavefront sensor (PWS) at near-infrared wavelengths for the measurement of the optical aberrations produced by atmospheric turbulence, while integrated in an adaptive optical system, has been studied. This is part of the framework of a project called PYRAMIR, that intends the installation of a new PWS at the 3.5 m telescope on the Calar Alto observatory in southern Spain. It complements the adaptive optics system ALFA, actually working with a Shack-Hartmann wavefront sensor at visible wavelengths.

The motivation for this work has been the potential increase of sky coverage that is obtained because of the higher number of bright infrared sources. Especially in the galactic region, where the new instrument is expected to give at least 27% of sky coverage, the increase is considerable when compared to the coverage of the existing visible wavefront sensor that is less than 1%. Also in regions of special interest, like star forming regions where the images generally suffer high extinction at visible wavelengths, infrared wavefront sensing can increase the coverage from almost 0 up to 20%.

From the technical point of view a PWS is better adapted for infrared wavefront sensing in ALFA. The temporal and spatial characteristics of the system and the fact that turbulence is less harmful to the images in the infrared allow the loop to be more easily closed at longer wavelengths. In closed-loop PWSs are expected to achieve higher sensitivity than Shack-Hartmann sensors.

The PWS has generally been used with a mechanical modulation of the beam around the pyramid tip, increasing the dynamic range of the sensor at the cost of lower sensitivity. A model for the effect of the atmospheric turbulence on the pyramid wavefront sensors' measurements was developed, which shows that it has a similar effect to the mechanical modulation usually employed in these systems. The model allows to estimate quantitatively the size of this effect which linearizes the signals on one side but reduces the sensitivity on the other side. The estimation done shows that the effect can be a non-negligible fraction of the one of mechanical modulations with amplitudes of  $1 \lambda/D$ . It has been verified at the telescope that the loop can be closed without mechanical modulation and the Strehl ratio achieved with only atmospheric modulation has shown to be slightly higher than with additional mechanical modulation. These

results are still preliminary and further tests should be made at the telescope to determine the optimum size of the modulation amplitude.

The techniques used for the analysis of adaptive optics systems working with pyramid wavefront sensors were essentially a full-system integrated modelling that simulates a full adaptive optics system working in open-loop and closed-loop. This model integrates the experience of a telescope including the real-time compensation of the atmospheric turbulence. A laboratory setup of an adaptive optics system was also used, with a pyramid wavefront sensor, a deformable mirror to compensate the aberrations and an interferometer working as independent wavefront sensor.

One of the objectives of the laboratory setup was to recognize problems with the optical setup. It has been adapted to the PYRAMIR instruments' setup so that the design of the latter could be optimized with the knowledge achieved.

The laboratory setup was characterized and the calibration techniques were elaborated. The experimental setup is able to perform open-loop and closed-loop corrections of 9 to 14 modes in the actual configuration without modulation and up to 35 modes with modulation. One of the main sources of error that have been found in the laboratory setup was the deformable mirror control and the poor quality of the generated modes. Further optimization of the deformable mirror modes will surely increase the number of controllable modes. Also the intrinsic deformation of the deformable mirror producing static aberration and the non-negligible roof size of the pyramids' tip were other relevant sources of error, that should be solved in future.

The optimum modulation amplitude in terms of reconstruction error propagation is estimated to be between 0.5 and 0.75  $\lambda/D$  (where  $\lambda/D$  is the PSF angular full width at half maximum) for a system working with 35 modes, no static aberrations and a calibration amplitude within the linear range of the sensor. Closed-loop simulations of atmospheric turbulence compensation show that by choosing an appropriate gain factor for the correction applied a non-modulated system may achieve the performance of a system modulated with the most appropriate amplitude.

Static aberrations, which are present in the non-common path of the wavefront sensor and the science channel, can be very harmful for the performance of a non-modulated PWS. Subtraction of the offset signal from the measured signals is essential in this case to maintain some sensitivity to the modes which are also present statically. Even so the range in which the sensor is able to measure correctly those modes is greatly reduced. To a certain degree this may be taken into account by the control system. For PYRAMIR the static aberrations due to the optical setup are expected to be  $0.05\lambda$ . This value stays within the linear range of the sensor and should not limit the dynamic range of measurements.

The effects of light loss through the edges and tip of the pyramid have been studied. Even through very small edges, in the scenario of a diffraction limited spot on the pyramid tip, the light loss is around 50%. This fraction decreases quite rapidly in case of a spot enlarged by

aberrations, reaching less than 20% with  $0.4\ \mu\text{m}$  root mean square aberration, for the case of PYRAMIR. In any case, the portion of light carrying the information about the distortion will always land further away of the pyramid tip and therefore, in case of a small tip, will land inside the four pupils, where it can be measured. Much more harmful is the effect of a pyramid roof, which creates an unsymmetrical illumination of the four pupils. It was estimated that the roof should not be bigger than  $20\ \mu\text{m}$  in the case of PYRAMIR.

Laboratory measurements give as upper limit for the diameter of a spatial filter in front of the pyramid  $2-5\ \lambda/D$ . One reason to use this spatial filter is to filter out higher order modes, which cause aliasing errors. For PYRAMIR it is mainly planned for reduction of the background. In the case the spatial filter is too small the loop does not close and the system does not reach a stable correction. For PYRAMIR this means that the spatial filter should not be smaller than 2 mm.

Different pyramids made of different glass types have been characterized and their suitability for the PYRAMIR instrument has been tested. A manufacturer able to meet the specifications has been found and fused silica glass pyramids have been delivered. This supplier already polished a pyramid for the laboratory having a roof size of  $46\ \mu\text{m}$  and the edge and surface quality needed to test the setup. The pyramid for PYRAMIR shows a smaller roof under the light microscope. Exact measurements with a profilometer are planned for the near future.

The possibility to use a three-sided pyramid has been analyzed. This alternative would greatly decrease the manufacturing problems due to the strict requirements for the roof size, since there is no roof formation in this case. In a first analysis there seems to be no reason to discard the possibility, even though systems with three-sided pyramids seem to be less stable than four-sided ones in closed loop simulations of atmospheric turbulence compensation, probably due to a slightly higher photon noise error propagation. Some three-sided pyramids have been manufactured and will be introduced in the laboratory setup very soon.

The PYRAMIR optical setup has been developed and optimized for the range of  $1.0-2.35\ \mu\text{m}$ , including J, H and K bands. Specifications for the pupil image quality, static aberrations and DM re-imaging quality have been worked out. With filters the sensing wavelength can be constricted to combinations of bands or single band. The limiting magnitude of PYRAMIR is estimated to be  $m_K=12$ . The instrument is being implemented in the ALFA system and technical first light is expected in the beginning of 2005.



# Appendix A

## Integration of the power spectrum

We describe here how to get expressions, which are easily integrable and only dependent on one parameter. First we will rewrite the power spectrum for each zernike mode  $Z_n$ :

$$w_{Z_j}(\nu) = 4(n+1)C_1 \int_{-\infty}^{+\infty} df_y \frac{|J_{n+1}(\pi D f)|^2}{\pi D f} \left[ \left( \frac{\nu}{V} \right)^2 + f_y^2 \right]^{-11/6} \begin{cases} 2 \cos^2(m\theta) & , m \neq 0 \\ 2 \sin^2(m\theta) & , m \neq 0 \\ 1 & , m = 0 \end{cases} \quad (\text{A-1})$$

with  $f = (f_x^2 + f_y^2)^{1/2}$   
and  $\begin{cases} f_x = f \cos \theta = \nu/V \\ f_y = f \sin \theta \end{cases}$

Performing a variable change  $\mu = V f_y$ , we obtain:

$$w_{Z_j}(\nu) = \underbrace{\frac{4(n+1)C_1 V^{14/3}}{\pi^2 D^2}}_{C_2} \int_{-\infty}^{+\infty} d\mu \frac{|J_{n+1} \left[ \frac{\pi D}{V} (\nu^2 + \mu^2)^{1/2} \right]|^2}{(\nu^2 + \mu^2)^{17/6}} \times \begin{cases} 2 \cos^2 \left[ m \arcsin \left( \frac{\mu}{(\nu^2 + \mu^2)^{1/2}} \right) \right] & , m \neq 0 \\ 2 \sin^2 \left[ m \arcsin \left( \frac{\mu}{(\nu^2 + \mu^2)^{1/2}} \right) \right] & , m \neq 0 \\ 1 & , m = 0 \end{cases} \quad (\text{A-2})$$

Now we will integrate the power spectrum for each mode n, changing to polar coordinates  $(r, \theta)$  with  $r^2 = \nu^2 + \mu^2$ :

$$\int_{-\infty}^{+\infty} d\nu w_{Z_j}(\nu) = C_2 \int_0^{2\pi} d\theta \int_0^{+\infty} dr \frac{|J_{n+1} \left( \frac{\pi D r}{V} \right)|^2}{r^{14/3}} \times \begin{cases} 2 \cos^2(m\theta) & , m \neq 0 \\ 2 \sin^2(m\theta) & , m \neq 0 \\ 1 & , m = 0 \end{cases} \quad (\text{A-3})$$

$$= 2\pi C_2 \int_0^{+\infty} dr \frac{|J_{n+1} \left( \frac{\pi D r}{V} \right)|^2}{r^{14/3}}. \quad (\text{A-4})$$

Changing variables again  $\rho = (\pi D r) / V$

$$\int_{-\infty}^{+\infty} d\nu w_{Z_j}(\nu) = 2\pi C_2 \left( \frac{V}{\pi D} \right)^{-11/3} \int_0^{+\infty} d\rho \frac{|J_{n+1}(\rho)|^2}{\rho^{14/3}}. \quad (\text{A-5})$$

At last we show how to integrate the power spectrum weighted with the error transfer function (in polar coordinates as before), defining  $a = V / (\pi D \nu_c)$ :

$$\begin{aligned} \int_{-\infty}^{+\infty} d\nu \left| T \left( \frac{\nu}{\nu_c} \right) \right|^2 w_{Z_j}(\nu) &= C_2 \left( \frac{\pi D}{V} \right)^{11/3} \int_0^{2\pi} d\theta \int_0^{+\infty} d\rho |T(a\rho \cos \theta)|^2 \frac{|J_{n+1}(\rho)|^2}{\rho^{14/3}} \\ &\times \begin{cases} 2 \cos^2(m\theta) & , m \neq 0 \\ 2 \sin^2(m\theta) & , m \neq 0 \\ 1 & , m = 0 \end{cases} \end{aligned} \quad (\text{A-6})$$

Substituting  $T$  from Eq. (4.13) the integration can be performed numerically and we see that the result, when normalized with Eq. (A-5), depends only on  $a$  (and on  $j$ ).

# Appendix B

## Dependencies of the modulation function

Here we rewrite Eq. (4.8), introducing the normalization with the telescope diameter  $D$ :

$$M(x', x, y) = \exp \left\{ - \sum_j \frac{2\sigma_j}{D^2} [P_j(x', y) - P_j(x, y)]^2 \right\}. \quad (\text{B-1})$$

Naming the outcome of Eq. (A-6) as  $f_j(a)$ , we have that

$$\sigma_j \propto f_j(a) j^{-\sqrt{3}/2} \left( \frac{D}{r_0} \right)^{5/3}. \quad (\text{B-2})$$

We can rewrite the exponential term of the modulation function:

$$M(x', x, y) \propto \left[ \exp \left( - \frac{1}{D^2} \right) \left( \frac{D}{r_0} \right)^{5/3} \right] \cdot \left[ \exp \left( - \sum_j f_j(a) j^{-\sqrt{3}/2} [P_j(x', y) - P_j(x, y)]^2 \right) \right]. \quad (\text{B-3})$$

From the first exponential we see that  $M(x', x, y)$  depends on  $Dr_0^5$ . The second exponential shows the dependence on  $a$ .



# Appendix C

## Singular value decomposition

The main definitions and results related to the singular value decomposition (SVD) used throughout this thesis are going to be resumed here. For a more detailed analysis refer to Golub and Van Loan (1983), f.ex., or for a more brief description relating the numerical computations see Press et al. (1992).

The wavefront reconstruction process can generally be described by a system of equations of the type:

$$\hat{s} = \mathbf{A}x + n \quad (\text{C-1})$$

where  $\hat{s}$  is a vector of estimated or measured gradient measurements,  $x$  is a vector describing the actual wavefront,  $\mathbf{A}$  is a matrix depending on the geometry of the problem and  $n$  is the noise associated with the measurement process, which is assumed as being random, uncorrelated and equal for all gradient measurements.

The objective is to find a solution in a least square sense, what means finding  $x$  such that  $(\mathbf{A}x - \hat{s})$  is minimum, where  $\mathbf{A}$  and  $\hat{s}$  are known.

One of the mostly used techniques to solve equation systems of the type

$$\mathbf{A}x = \hat{s}, \quad (\text{C-2})$$

where  $\mathbf{A}$  is not invertible, is to find the *pseudo-inverse* of  $\mathbf{A}$  through SVD.

The SVD is one of the most important decompositions in matrix computations. It is based on a theorem, whose proof can be accessed in the given literature:

**Theorem** Given a matrix  $\mathbf{A}_{m \times n}$ , there exist a column-orthogonal matrix  $\mathbf{U}_{m \times m}$ , a diagonal matrix  $\mathbf{W}_{n \times n}$  and an orthogonal matrix  $\mathbf{V}_{n \times n}$ , so that  $\mathbf{A}$  can be written as

$$\mathbf{A} = \mathbf{U}\mathbf{W}\mathbf{V}^T. \quad (\text{C-3})$$

The diagonal elements of  $\mathbf{W}$  are called the *singular values* and are greater or equal to zero. The pseudo-inverse  $\mathbf{A}^+$  can be calculated as:

$$\mathbf{A}^+ = \mathbf{V} [\text{diag}(1/w_j)] \mathbf{U}^T, \quad (\text{C-4})$$

where  $[\text{diag}(1/w_j)]$  is a diagonal matrix with the inverse values of  $\mathbf{W}$  in the diagonal.

The condition number of the matrix ( $\kappa(\mathbf{A})$ ) is defined as the ratio of the largest (in magnitude) of the  $w_j$ 's to the smallest of the  $w_j$ 's. In case of a very small  $w_j$  approaching the machine's floating-point precision it is *ill-conditioned*. If the smallest  $w_j$  is zero the condition number is infinite and the matrix is singular. In this case there is a subspace of  $x$  which is mapped to zero:  $\mathbf{A}x = 0$ , which is called the nullspace. The range of  $\mathbf{A}$  is the subspace of  $\hat{s}$  where some  $x$  is mapped on. The SVD constructs orthonormal bases for the range (the columns of  $\mathbf{U}$  which have correspondent singular values that are non-zero) and the nullspace of  $\mathbf{A}$  (the columns of  $\mathbf{V}$  which have correspondent singular values that are zero).

If  $\hat{s} = 0$  any column of  $\mathbf{V}$  that has a correspondent singular value that is zero is a solution. If  $\hat{s} \neq 0$  and it lies in the range of  $\mathbf{A}$  there is a solution for the system of equations<sup>1</sup>. It can be shown that the solution with the smallest length  $|x|^2$  of Eq. C-2 is:

$$x = \mathbf{A}^+ \hat{s}, \quad (\text{C-5})$$

where the  $(1/w_j)$  are replaced by zero if  $w_j = 0$ .

If  $\hat{s} \neq 0$  and it does not lie in the range of  $\mathbf{A}$  the SVD will not allow to find an exact solution, but the best solution in a least-square sense, which will minimize the residual  $r = (\mathbf{A}x - \hat{s})$ .

In the case of an over-determined system with more equations than unknowns, which is the case in this work, generally no  $w_j$ 's are zero. Even though it may be an advantage to set some very small ones to zero, because the corresponding columns are linear combinations of  $x$  which are very insensitive to the data and can destabilize the system pulling the solution vector in a wrong direction and increasing the residual.

The condition number of the system is also a measure for the sensitivity of the linear system to slight perturbations in  $\mathbf{A}$  or  $\hat{s}$  (Golub and Van Loan (1983)):

$$\frac{\Delta x}{x} \leq \kappa(\mathbf{A}) \left( \frac{\Delta \mathbf{A}}{\mathbf{A}} + \frac{\Delta \hat{s}}{\hat{s}} \right), \quad (\text{C-6})$$

meaning that the relative error in the solution  $x$  has as upper value the condition number times the sum of the relative errors of  $\mathbf{A}$  and  $\hat{s}$ .

---

<sup>1</sup>Since any of the nullspace vectors can be added to the solution it has even more than one solution.

# Appendix D

## Zernike polynomes

The description of optical aberrations is very often done in two-dimensional Zernike polynomes, which allow to decompose complex wavefront shapes into a set of basis functions. They were introduced by Zernike (1934) and their low order terms correspond to the classical aberrations like tilt, defocus and astigmatism. They are a set of orthogonal polynomes defined on a unit circle and every two-dimensional function can be described by a linear combination of them. In Noll (1976) the use of zernike polynomes for a description of the turbulent atmosphere is discussed. His notation, given in polar coordinates  $\rho$  and  $\theta$ , is reproduced here:

$$\begin{aligned} Z_{j_{\text{even}}} &= \sqrt{n+1} R_n^m(\rho) \sqrt{2} \cos(m\theta) & \text{for } m \neq 0 \\ Z_{j_{\text{odd}}} &= \sqrt{n+1} R_n^m(\rho) \sqrt{2} \sin(m\theta) & \text{for } m \neq 0 \\ Z_j &= \sqrt{n+1} R_n^0(\rho) & \text{for } m = 0 \end{aligned} \quad (\text{D-1})$$

where

$$R_n^m(\rho) = \sum_{k=0}^{\frac{n-m}{2}} \frac{(-1)^k (n-k)!}{k! (\frac{n+m}{2} - k)! (\frac{n-m}{2} - k)!} \rho^{n-2k}. \quad (\text{D-2})$$

The indices  $n$  and  $m$  represent the radial order and the azimuthal frequency respectively. They satisfy  $n \geq m$  and  $n - m$  is even. The index  $j$  can be obtained from  $n$  and  $m$  and is an ordering of the modes. Even values of  $j$  correspond to symmetric modes in  $\cos m\theta$  and odd values of  $j$  correspond to antisymmetric modes in  $\sin m\theta$ . The normalization is such that each polynomial has a root-mean-square value of 1 over the unit disk. They are represented in Tab. D.1 till  $j = 11$  and in Fig. D.1 till  $j = 70$ .

Noll (1976) and later Wang and Markey (1978) have represented the Kolmogorov turbulence spectrum by Zernike polynomes. They evaluated the covariance matrix of the expansion coefficients, which is not purely diagonal because polynomial terms having the same azimuthal frequency  $m$  do not have 0 covariance. This implies a certain redundancy in the decomposition which can only be eliminated by using a basis set like Karhùnen-Loeve functions (Wang and Markey (1978)). These are defined in a way that their covariance matrix is diagonal but they vary according to the stochastic process that they are describing. Despite the differences, the first order Karhùnen-Loeve functions are very similar to the first order Zernike polynomes.

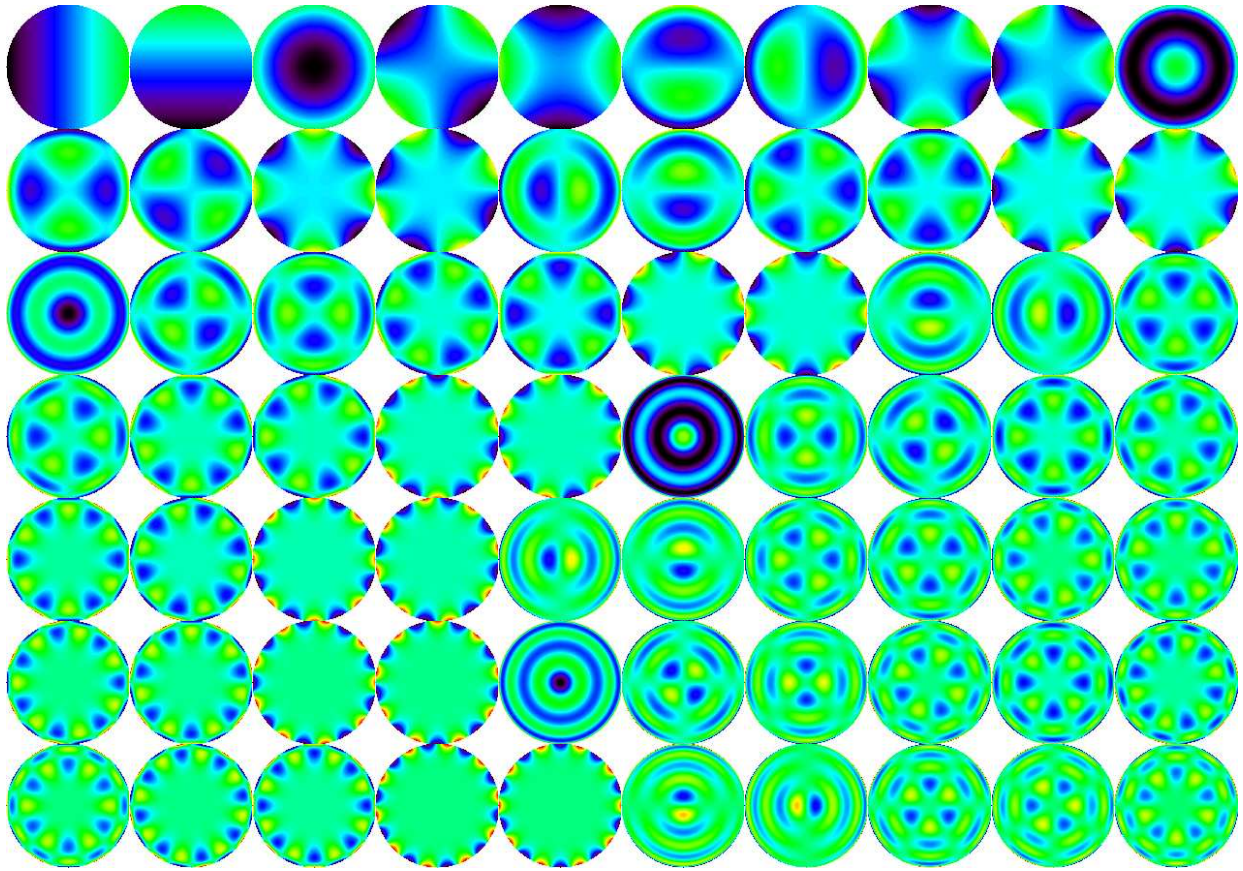


Figure D.1: The first 70 zernike polynomials excluding the piston mode.

n	m=0	m=1	m=2	m=3
0	$Z_1 = 1$ (piston)			
1		$Z_2 = 2\rho \cos \theta$ $Z_3 = 2\rho \sin \theta$ (tip/tilt)		
2	$Z_4 = \sqrt{3}(2\rho^2 - 1)$ (defocus)		$Z_5 = \sqrt{6}\rho^2 \sin 2\theta$ $Z_6 = \sqrt{6}\rho^2 \cos 2\theta$ astigmatism	
3		$Z_7 = \sqrt{8}(3\rho^3 - 2\rho)\sin\theta$ $Z_8 = \sqrt{8}(3\rho^3 - 2\rho)\cos\theta$ (coma)		$Z_9 = \sqrt{8}\rho^3 \sin 3\theta$ $Z_{10} = \sqrt{8}\rho^3 \cos 3\theta$ (trifoil)
4	$Z_{11} = \sqrt{5}(6\rho^4 - 6\rho^2 + 1)$ (spherical aberration)			

Table D.1: The first 11 zernike polynomes according to Nolls' notation.

# Bibliography

- Anderson, B. D. O. and Moore, J. B. (1990). *Optimal Control: Linear Quadratic Methods*. Prentice Hall.
- Babcock, H. W. (1953). The Possibility of Compensating Astronomical Seeing. *Pub. Astr. Soc. Pac.*, 65(386):229–236.
- Bally, J., Yu, K. C., Rayner, J., and Zinnecker, H. (1998). Hubble Space Telescope Wide Field Planetary Camera 2 Observations of the Young Bipolar H II Region S106. *Astron. Journal*, 116:1868–1881.
- Baumeister, H., Bizenberger, P., Bailer-Jones, C., Kovacs, Z., Röser, H.-J., and Rohloff, R.-R. (2002). Cryogenic engineering for OMEGA2000: design and performance. In M.Iye and Moorwood, A., editors, *Instrument Design and Performance for Optical/Infrared Ground-based Telescopes*, volume 4841 of *Proc. SPIE*, pages 343–354.
- Berkefeld, T., Weiss, R., and Glindemann, A. (2002). Simulations of Kolmogorov Phase Screens - Algorithms and Applications. *submitted to Appl. Opt.*
- Born, M. and Wolf, E. (1999). *Principles of optics*. Cambridge University Press, 7th edition.
- Butler, D. J., Marchetti, E., Bähr, J., Xu, W., Hippler, S., Kasper, M. E., and Conan, R. (2003). Phase screens for astronomical multi-conjugate adaptive optics: application to MAPS. In Wizinowich, P. L. and Bonaccini, D., editors, *Adaptive Optical System Technologies II*, volume 4839 of *Proc. SPIE*, pages 623–634.
- Carbillet, M., Vérinaud, C., Esposito, S., Riccardi, A., Puglisi, A., Femenia, B., and Fini, L. (2003). Performance of the first-light AO system of LBT by means of CAOS simulations. In Wizinowich, P. L. and Bonaccini, D., editors, *Adaptive Optical System Technologies II*, volume 4839 of *Proc. SPIE*, pages 131–139.
- Chan, S., Henning, T., and Schreyer, K. (1996). A catalogue of massive young stellar objects. *A&AS*, 115:285–+.
- Clare, R. M. and Lane, R. G. (2003). Wavefront sensing from spatial filtering at the focal plane. In Tyson, R. K. and Lloyd-Hart, M., editors, *Astronomical Adaptive Optics Systems and Applications*, volume 5169 of *Proc. SPIE*, pages 43–54.

- Claudi, R. U., Costa, J., Feldt, M., Gratton, R., Amorim, A., Henning, T., Hippler, S., Neuhäuser, R., Pernechele, C., Turatto, M., Schmid, H. M., Walters, R., and Zinnecker, H. (2004). CHEOPS: a second generation VLT instrument for the direct detection of exoplanets. In *Second Eddington Workshop: Stellar structure and habitable planet finding, 9 - 11 April 2003, Palermo, Italy. Edited by F. Favata, S. Aigrain and A. Wilson. ESA SP-538, Noordwijk: ESA Publications Division, ISBN 92-9092-848-4, 2004, p. 301 - 304*, pages 301–+.
- Conan, J. M., Rousset, G., and Madec, P.-Y. (1995). Wave-front temporal spectra in high-resolution imaging through turbulence. *J. Opt. Soc. Am A*, 12:1559–1570.
- Costa, J. B. (2004). The modulation effect of the atmosphere in the pyramid wavefront sensor. *Appl. Opt. (accepted)*.
- Costa, J. B., Feldt, M., and Stumpf, M. (2004a). Testing a Non-Modulated Wavefront Sensor. In *Advancements in Adaptive Optics*, volume 5490 of *Proc. SPIE*.
- Costa, J. B., Feldt, M., Wagner, K., Bizenberger, P., Hippler, S., Stumpf, M., and Henning, T. (2004b). Status Report of Pyramir - A Near-Infrared Pyramid Wavefront Sensor for ALFA. In *Advancements in Adaptive Optics*, volume 5490 of *Proc. SPIE*.
- Costa, J. B., Hippler, S., Feldt, M., Esposito, S., Ragazzoni, R., Bizenberger, P., Puga, E., and Henning, T. (2003a). PYRAMIR: A Near-Infrared Pyramid Wavefront Sensor for the Calar Alto Adaptive Optics System. In Wizinowich, P. L. and Bonaccini, D., editors, *Adaptive Optical System Technologies II*, volume 4839 of *Proc. SPIE*, pages 280–287.
- Costa, J. B., Ragazzoni, R., Ghedina, A., Carbillet, M., Verinaud, C., Feldt, M., Esposito, S., Puga, E., and Farinato, J. (2003b). Is there Need of any Modulation in the Pyramid Wavefront Sensor? In Wizinowich, P. L. and Bonaccini, D., editors, *Adaptive Optical System Technologies II*, volume 4839 of *Proc. SPIE*, pages 288–298.
- Esposito, S., Feeney, O., and Riccardi, A. (2000a). Laboratory test of a pyramid wavefront sensor. In Wizinowich, P. L., editor, *Adaptive Optical Systems Technology*, volume 4007 of *Proc. SPIE*, pages 416–422.
- Esposito, S. and Riccardi, A. (2001). Pyramid Wavefront Sensor behavior in partial correction Adaptive Optic Systems. *A&A*, 369(L9).
- Esposito, S., Riccardi, A., and Feeney, O. (2000b). Closed-loop performance of pyramid wavefront sensor. In Steiner, T. D. and Merritt, P. H., editors, *Laser Weapons Technology*, volume 4034 of *Proc. SPIE*, pages 184–189.
- Feeney, O. A. (2001). *Theory and Laboratory Characterisation of Novel Wavefront Sensor for Adaptive Optics Systems*. PhD thesis, National University of Ireland, Galway.
- Feldt, M., Costa, J., Stumpf, M., Schmid, H. M., Berton, A., and Lima, J. (2004). Wavefront Sensing through Spatial Filters: The Case for Coronagraphic, High Contrast AO Systems. In *Advancements in Adaptive Optics*, volume 5490 of *Proc. SPIE*.

- Feldt, M., Henning, T. F. E., Hippler, S., Weiß, R., Turatto, M., Neuhäuser, R., Hatzes, A. P., Schmid, H. M., Waters, R., Puga, E., and Costa, J. (2003a). Can we really go for direct exo-planet detection from the ground? In Schultz, A. B., editor, *High-Contrast Imaging for Exo-Planet Detection*, volume 4860 of *Proc. SPIE*, pages 149–160.
- Feldt, M., Hippler, S., Henning, T., Gratton, R., Turatto, M., Waters, R., and Quirrenbach, A. (2003b). The Planet Finder: Proposal for a 2nd Generation VLT Instrument. In *ASP Conf. Ser. 294: Scientific Frontiers in Research on Extrasolar Planets*, pages 569–572.
- Feldt, M., Turatto, M., Schmid, H. M., Waters, R., Neuhäuser, R., and Amorim, A. (2003c). A "Planet Finder" instrument for the ESO VLT. In *ESA SP-539: Earths: DARWIN/TPF and the Search for Extrasolar Terrestrial Planets*, pages 99–+.
- Fernández, E. J. and Artal, P. (2003). Membrane deformable mirror for adaptive optics: performance limits in visual optics. *Opt. Express*, 11(9):1056–1069.
- Foucault, L. M. (1859). Mémoire sur la construction des télescopes en verre argenté. *Ann. Obs. Imp. Paris*, 5(197).
- Fried, D. L. (1965). Statistics of a Geometric Representation of Wavefront Distortion. *J. Opt. Soc. Am.* **A**, 55(11):1427–1435.
- Ghedina, A., Cecconi, M., Ragazzoni, R., Farinato, J., Baruffolo, A., Crimi, G., Diolaiti, E., Esposito, S., Fini, L., Ghigo, M., Marchetti, E., Niero, T., and Puglisi, A. (2003). On Sky Test of the Pyramid Wavefront Sensor. In Wizinowich, P. L. and Bonaccini, D., editors, *Adaptive Optical System Technologies II*, volume 4839 of *Proc. SPIE*, pages 869–877.
- Glindemann, A. (1997). Beating the Seeing Limit-Adaptive Optics on Large Telescopes. Habilitation, University of Heidelberg, Germany.
- Golub, G. H. and Van Loan, C. F. (1983). *Matrix computations*. The Johns Hopkins University Press.
- Goodman, J. W. (1996). *Introduction to Fourier Optics*. Mc Graw Hill, 2nd edition.
- Hardy, J. W. (1998). *Adaptive Optics for Astronomical Telescopes*. Oxford University Press.
- Hartmann, J. (1900). Remarks on the Construction and Adjustment of Spectrographs. *Ap. J.*, 11:400–413.
- Hecht, E. (2002). *Optics*. Addison Wesley, 4th edition.
- Hippler, S., Glindemann, A., Kasper, M., Kalas, P., Rohloff, R., Wagner, K., Looze, D., and Hackenberg, W. (1998). Alfa: The mpia/mpe adaptive optics with a laser for astronomy project. In Bonaccini, D. and Tyson, R., editors, *Adaptive Optical System Technologies*, volume 3353 of *Proc. SPIE*, pages 44–55.
- Kasper, M. (2000). *Optimization of an adaptive optics system and its application to high-resolution imaging spectroscopy of T Tauri*. PhD thesis, University of Heidelberg, Germany.

- Kasper, M., Looze, D., Hippler, S., Herbst, T., Glindemann, A., Ott, T., and Wirth, A. (2000). ALFA: Adaptive optics for the Calar Alto observatory - optics, control system, and performance. *Experimental Astronomy*, 10:49–73.
- Kurtz, S., Churchwell, E., and Wood, D. (1990). A High Resolution Radio Survey of FIR Color Selected UC HII Regions. *BAAS*, 22:1269–+.
- Ligori, S., Grimm, B., and Hippler, S. (2004). Performance of PYRAMIR detector System. In *Advancements in Adaptive Optics*, volume 5490 of *Proc. SPIE*.
- Linfoot, E. H. (1948). On the theory of the Zonal Foucault Test. *Monthly Notices Roy. Astron. Soc.*, 108:428–445.
- Noll, R. J. (1976). Zernike polynomials and atmospheric turbulence. *J. Opt. Soc. Am A*, 66(3):207–211.
- Poyneer, L. A. and Macintosh, B. (2004). Spatially filtered wave-front sensor for high order adaptive optics. *J. Opt. Soc. Am. A*, 21(5):810–819.
- Press, W. H., Flannery, B. P., Teukolsky, S. A., and Vetterling, W. T. (1992). *Numerical Recipes in C: The Art of Scientific Computing*. Cambridge University Press, 2nd edition.
- Prieto, P. M., Vargas-Martín, F., Goelz, S., and Artal, P. (2000). Analysis of the performance of the Hartmann-Shack sensor in the human eye. *J. Opt. Soc. Am A*, 17:1388–1398.
- Ragazzoni, R. (1996). Pupil plane wavefront sensing with an oscillating prism. *J. Modern Opt.*, 43(2):289–293.
- Ragazzoni, R., Diolaiti, E., and Viard, E. (2002). A pyramid wavefront sensor with no dynamic modulation. *Opt. Comm.*, 208(51).
- Ragazzoni, R. and Farinato, J. (1999). Sensitivity of a pyramidal Wave Front sensor in closed loop Adaptive Optics. *A&A*, 305(L23-L26).
- Ragazzoni, R., Ghedina, A., Baruffolo, A., Marchetti, E., Farinato, J., Niero, T., Crimi, G., and Ghigo, M. (2000). Testing the pyramid wavefront sensor on the sky. In Wizinowich, P. L., editor, *Adaptive Optical Systems Technology*, volume 4007 of *Proc. SPIE*, pages 423–430.
- Ragazzoni, R., Herbst, T. M., and et al., W. G. (2003). A visible MCAO channel for NIR-VANA at the LBT. In Wizinowich, P. L. and Bonaccini, D., editors, *Adaptive Optical System Technologies II*, volume 4839 of *Proc. SPIE*, pages 536–543.
- Riccardi, A., Bindi, N., Ragazzoni, R., Esposito, S., and Stefanini, P. (1998). Laboratory characterization of a Foucault-like wavefront sensor for Adaptive Optics. In Bonaccini, D. and Tyson, R. K., editors, *Adaptive Optical System Technologies*, volume 3353 of *Proc. SPIE*, pages 941–951.
- Rohloff, R.-R., Baumeister, H., Ebert, M., Münch, N., and Naranjo, V. (2004). Cryogenic actuators in ground-based astronomical instrumentation. In *Astronomical Structures and Mechanisms Technology*, volume 5495 of *Proc. SPIE*.

- Stumpf, M. (2004). Laboratory Setup for an infrared pyramid wavefront sensor. Diplomarbeit, University of Heidelberg, Germany.
- Vdovin, G. V. (1996). *Adaptive mirror micromachined in silicon*. PhD thesis, Technische Universität Delft.
- Vérinaud, C. (2004). On the nature of the measurements provided by a pyramid wavefront sensor. *Opt. Commun.*, 233:27–38.
- Wang, J. Y. and Markey, J. K. (1978). Modal compensation of atmospheric turbulence phase distortion. *J. Opt. Soc. Am.*, 68:78–87.
- Weiss, R. (2000). TurbuLenz. <http://www.mpia-hd.mpg.de/AO/ATMOSPHERE/Turbulenz/tlz.html>.
- Wilson, R. G. (1975). Wavefront-error evaluation by mathematical analysis of experimental Foucault-test data. *Appl. Opt.*, 14(9):2286–2297.
- Zernike, F. (1934). Beugungstheorie des Schneidverfahrens und seiner verbesserten Form, der Phasenkontrastmethode. *Physica*, 94:689–704.



# Acknowledgements

This work would not have been possible without the help and support of many, many people. I want to thank especially to ...

Professor Dr. Reinhard Mundt for the supervision of this thesis and for many good advice on the way.

Professor Dr. Josef Bille for being co-advisor, for always believing in me and my work and for his enthusiasm and interest.

Dr. Markus Feldt for the direct engagement in the elaboration of this thesis, many fruitful discussions and his support and interest in many situations.

Dr. Stefan Hippler for giving me the chance of working on this interesting project and for opening me the doors to collaborations with many interesting people.

Prof. Dr. Thomas Henning for his interest and support during this work.

Peter Bizenberger, from whom I learned so much, for his great knowledge in optics and optical design, for unnumbered discussions and shared thoughts about PYRAMIR and especially for his friendship and support through all the way.

Professor Dr. Roberto Ragazzoni for many precious moments, where I found someone who listened and made me think more deeply.

Dr. Simone Esposito for teaching me so many things about pyramid wavefront sensors during my stay in Florence at the beginning of this work. I also thank him and all people in Florence for making my stay so joyful.

Adriano Ghedina for the time he spent making the telescope measurements at TNG.

Dr. Elena Puga, Dr. Sadegh Khochfar, Dr. Robert Weiss, Richard D'Souza and Boris Rockenfeller for the unique combination of friendship, work and a lot of fun in the office.

Wolfgang Gaessler for helping so much with advice and good ideas, for questioning and thinking.

Dr. Elena Masciadri for her accurate questions and good advice.

Dr. Tom Herbst for polishing pyramids for us in his free time.

All the people from the mechanics and electronics departments for helping out with often very creative and unconventional ideas.

Elena Puga for always spreading good mood around her, for her contagious laugh, for all the scientific and non-scientific support, but especially for being the best friend I have ever had and for sharing the best times I spent in my life!

Dr. Andrea Borch for a great collaboration as women-representative and all the deep thoughts about women we shared.

Carmelo Arcidiacono for helping out with his programs.

Micaela Stumpf for the good collaboration in the laboratory and her cheerfulness.

Sebastian Egner and Stephan Kellner for all the support given in the laboratory, for serious and non-serious conversations and for a good laugh now and then.

Elena, Sebastiano, Laura, Nadine, Boris, Richard, Jakob, Olivier, Jens, Boris, Elena, Martin, Claudia, Dimitrios, Johny, Stephan and all the people from the "unofficial" science-coffee for unforgettable moments of laughter. I had a great time with you! And of course thanks to the italian side for teaching us that coffee has to be italian!

Dr. Markus Feldt, Wolfgang Gaessler and Richard D'Souza for proof-reading this thesis.

The people from the Physics and Optometry and Vision Science Department from the University of Braga for giving me the freedom to finish my thesis in the last weeks.

My parents for always believing in me and supporting me in all my projects. But especially for teaching me to be strong and to have a strong will.

My mother, my father, my sister Sonia and my brother Ricardo for always helping with all their means especially in the last months of this work, keeping me alive.

Marta for being such a wonderful person and for almost not crying in the night.

Filipe for being a part of me for all these years.